Dynamic Response of an Orthotropic Bridge Deck Subjected to EOVs

A Case Study of the Haringvlietbrug

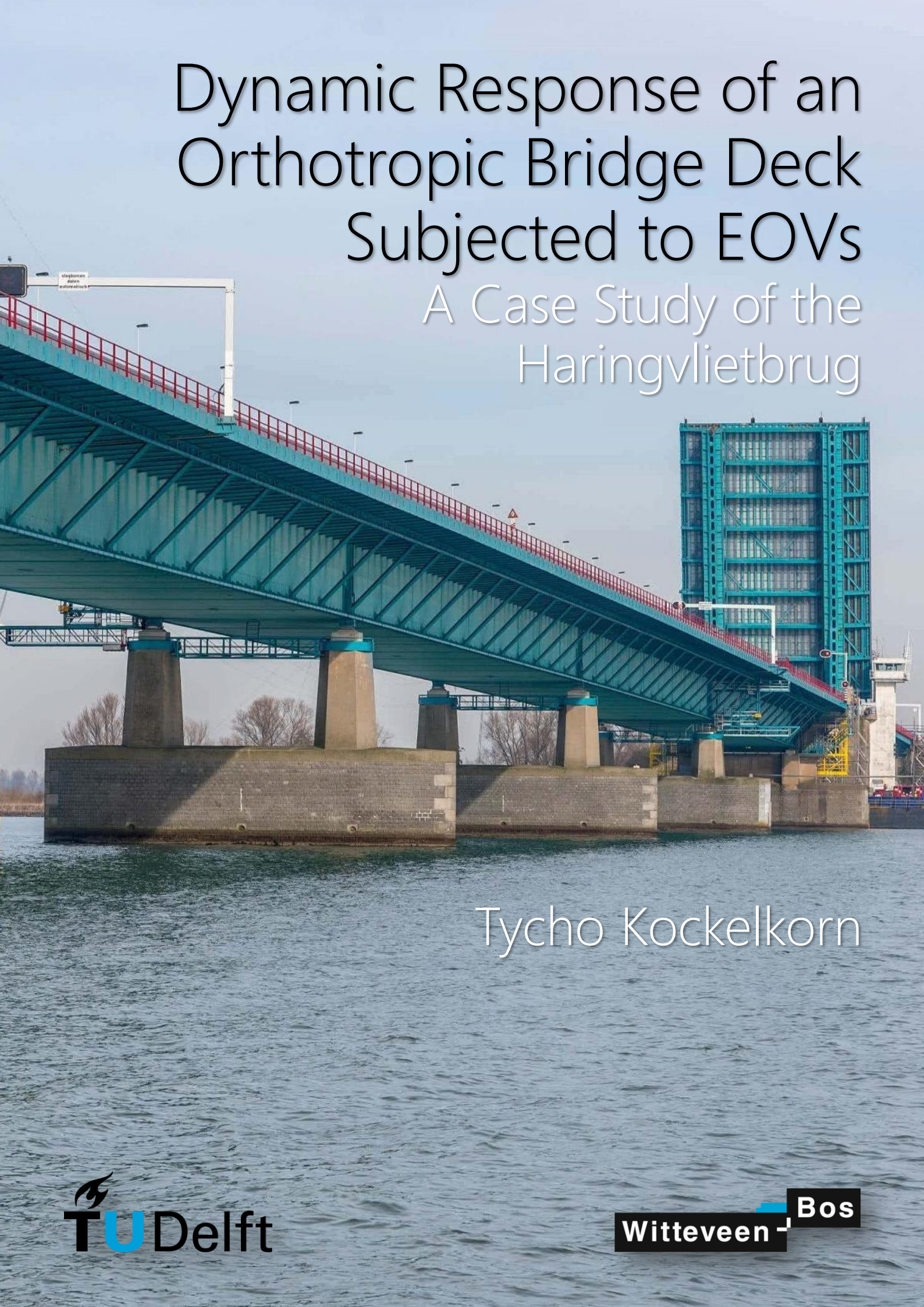

Tycho Kockelkorn

TU Delft

Witteveen+Bos

Dynamic Response of an Orthotropic Bridge Deck Subjected to EOVs

A Case Study of the Haringvlietbrug

by

P.T. Kockelkorn

in partial fulfilment of the requirements for the degree of

Master of Science
in Civil Engineering

at the Delft University of Technology,
to be defended publicly on Monday June 27, 2022 at 15:00 PM.

Student number:	4477499	
Project duration:	September, 2021 – June, 2022	
Thesis committee:	Prof. dr. A.V. Metrikine	TU Delft, chair
	Dr. ir. E. Lourens	TU Delft
	Dr. ir. K.N. van Dalen	TU Delft
	Ir. F. Besseling	Witteveen+Bos
	Ir. J. de Bruijn	Witteveen+Bos

An electronic version of this report will be available at
`http://repository.tudelft.nl/` from January 1, 2023.

Cover picture by Rijkswaterstaat.

TU Delft Delft University of Technology

Witteveen+Bos

Preface

Here it is. In front of you is my master thesis on SHM and the dynamic response of the bridge deck of the Haringvlietbrug. With its submission, I have met all the requirements for the degree of Master of Science in Civil Engineering, specialised in Structural Engineering and Dynamics of Structures, at the Delft University of Technology. Writing the thesis has asked a lot of me. The subject has changed several times: the initial thought was to apply machine learning algorithms, but I ended up creating a theoretical model of bridge vibrations. Moreover, the Covid-19 lockdowns decided for me if I went to the office in Deventer or stayed at home. Fortunately, the university was always open to study and drink coffee with my fellow graduate students.

But now it is done. I almost cannot believe this year of writing my thesis and, most of all, seven beautiful years of studying in Delft have come to an end. I will never forget my time in Delft with a lot of great memories of amongst others Huize de Zeester, JC Eclipse, the COWcie and my MDP. But now, the time for the next steps of my life has come.

I could not have written this thesis all by myself. Without the time and feedback given by the members of the thesis committee, the thesis would have looked completely different. First of all, I would like to thank ir. Floris Besseling. Exactly one year ago, we had contact for the first time and he enthused me about this subject and for working together with him. He was always willing to make time to answer my questions or for discussions. The same was true for dr. ir. Eliz-Mari Lourens and ir. Janno de Bruijn who were always present at the update meetings every other week and provided a lot of tips, suggestions and enthusiasm. Then, I want to thank the chair of the committee, prof. dr. Andrei Metrikine who extensively helped me with setting up the semi-analytical model and whose lectures during my bachelor's and master's were among the best in my opinion. I am also grateful to my colleagues for their advice and Witteveen+Bos for facilitating my thesis. Finally, I want to thank my friends, family and fellow graduate students for listening to all my thesis worries.

Overall, I am satisfied with the results of this research and, above all, with my time in Delft. I hope there will be follow-up research capable of validating the results and making vibration-based SHM work in this context. For now, I hope you enjoy the read!

P.T. Kockelkorn
Delft, June 2022

Summary

The Haringvlietbrug, which was delivered in 1964 and connects the island of Goeree-Overflakkee to the Dutch mainland, approaches the end of its lifetime. Rijkswaterstaat and Witteveen+Bos investigate the potential use of vibration-based structural health monitoring (SHM) to track deterioration. In vibration-based SHM, a change in the structure's eigenfrequencies indicates probable damage but most current approaches focus on fundamental modes of the structure which are not or hardly affected by small structural impairments. In this study, vibration-based SHM was employed on local modes of vibration of the Haringvlietbrug, with the hope of detecting small-scale damage. New obstacles arose as a result of this: the influence of environmental and operational variabilities (EOV) on the eigenfrequencies of the structure was often larger than the influence of small damage. As a result, the EOVs should be filtered out of the recorded acceleration data before damage-sensitive features can be extracted.

To investigate this, 32 accelerometers and 16 temperature sensors were installed in two segments of the Haringvlietbrug. The sensors yield a large data set which was analysed extensively. This made it clear, among other things, that the dynamic response of the bridge deck showed large variability when comparing different vehicle passages.

The first research objective was to investigate the applicability of similarity filtering (SF) to filter out operational variabilities from the Haringvlietbrug acceleration signals to extract damage-sensitive features. SF amplified similarities and damped differences between samples of vehicle passages. This way, only consequently excited modes should remain in the signals which were subsequently used as damage-sensitive features for SHM.

This study found that using SF to filter the operational variabilities from the Haringvlietbrug data set was ineffective. Three reasons were identified for this. First, the method was not robust as a single deviating sample or a poorly chosen filter coefficient significantly influenced the results. Secondly, missing closely-spaced modes might have caused inconsistency of the results. Lastly, SF was not able to converge to consistent behaviour as the variability of response of the bridge deck might be too great for different passages. The latter reason was investigated further in the remaining of the research.

The second research objective was to improve the understanding of the effect of vehicles on local bridge vibrations of the Haringvlietbrug for the application of vibration-based SHM. First, the eigensystem realisation algorithm (ERA) was used to identify and compare consistent mode shapes in order to better understand bridge deck vibrations and find patterns in the eigenfrequencies. ERA is an operational modal analysis (OMA) and output-only system identification technique.

ERA was able to identify two consistent modes in the data but they had a large variance in both shape and eigenfrequency. The uncertainties of the results were too large to draw firm conclusions based on ERA because two of ERA's key assumptions were not perfectly met and the input samples were not optimal.

Next, a semi-analytical model of a segment of the Haringvlietbrug was built to simulate the important sources of the variability as found in the acceleration recordings of the Haringvlietbrug. The goal of the model was to investigate the sensitivity of the response of the beam to variations of input parameters. The model was both used for time-history analyses and eigenfrequency analyses. Parametric studies showed that the response of the beam was highly sensitive to the time delay between moving masses (dependent on the axle configuration and vehicle velocity), the unevenness (describing any source of vibration of the interaction between vehicle and bridge deck) and the vehicle velocity. These parameters influenced both the amplitude and the shape of the acceleration response of the Haringvlietbrug bridge deck in the time and frequency domain.

The effect of the three dominant parameters was further investigated by simulating four characteristic cases from the Haringvlietbrug data set. Hypotheses on the source of the measurement variability were formed by qualitatively comparing the results of the model to the measured response of the bridge. The model parameters were able to describe a large part of the variability but it was concluded that it is likely that some factors that were not included in the model also play a role in the variability of the measurements.

The above findings led to the following recommendations for further research. Firstly, it is recommended to only select similar vehicle passages for SF because this would improve the ability to converge to consistent modal behaviour. Secondly, should someone want to further explore ERA, it is recommended to equip a section of the bridge with a high spatial density of accelerometers to improve the reliability of the results.

Next, some recommendations related to the model were made. The first step of follow-up research would be to verify the influence of the model parameters on the dynamic response of the Haringvlietbrug by experimenting with different test vehicles. Subsequently, depending on the importance of the parameters, possible extensions of the measurement set-up for a new campaign were proposed. Secondly, the current model could be improved by introducing more parameters, like acceleration of the moving mass or by implementing a more realistic vehicle model, to be better able to explain the dynamic variability. Thirdly, more parameters could be investigated by building a 3D finite element model. This would make it possible to investigate the influence of the presence of multiple vehicles on the bridge and 3D wave propagation.

Upcoming research into data-driven approaches of vibration-based SHM of bridge decks is recommended to focus on similar passages as not all samples contain the same information on the dynamic behaviour of the structure. Decreasing the variability of the input samples might improve the performance of the algorithms.

Contents

Acronyms

ANN artificial neural network.

ARX Auto-Regression with eXogenous variables.

CMI consistent-mode indicator.

CSD cross-spectral density.

DAF dynamic amplification factor.

EMA experimental modal analysis.

EOV environmental and operational variabilities.

ERA eigensystem realisation algorithm.

FDD frequency domain decomposition.

FT Fourier transform.

KNMI Royal Dutch Meteorological Institute.

LTI linear time-invariant.

MAC modal assurance criterion.

ML machine learning.

OMA operational modal analysis.

OSP optimisation of sensor placement.

SDD structural damage detection.

SDOF single degree-of-freedom.

SF similarity filtering.

SHM structural health monitoring.

SVD singular value decomposition.

SVM support vector machine.

VBI vehicle-bridge interaction.

WT wavelet transform.

1

Introduction

The Netherlands is full of 'baby boomer bridges', bridges built in the fifties and the sixties of the last century, a time when the dutch highway network was expanding rapidly. Today, these bridges are about 60 years old, approaching their end of life. In fact, this is the case for 568 bridges and viaducts in the Netherlands. Some of them even have already exceeded their original lifespan according to Rijkswaterstaat[1], the practical executor of the public works and water management in the Netherlands. One of these bridges is the Haringvlietbrug in the province of South Holland. The bridge was delivered in 1964 and is an important connection between South Holland, Zeeland and North Brabant. The condition of the bridge is, however, bad. So bad that measures were taken by Rijkswaterstaat to preserve the bridge until its renovation in 2023 as visible in Figure 1.1: the lanes were narrowed and the speed limit was lowered from 100 km/h to 50 km/h leading to delays for road users.

Figure 1.1: A picture of the Haringvlietbrug with the measures taken because of its bad condition (source: Rijkswaterstaat).

Damage to and degradation of structures is inevitable as structures are continuously prone to environmental and operational factors like rain and traffic. It is therefore necessary that the health of structures is monitored. Monitoring of structures used to be done with visual inspections, but now a large variety of techniques exists to monitor structures even on a continuous basis. One of these methods is vibration-based structural health monitoring (SHM). With SHM, Rijkswaterstaat aims to improve its knowledge about the current state

[1] https://nos.nl/artikel/2394865-babyboomerbruggen-toe-aan-groot-onderhoud-files-en-kosten-verwacht

of bridges and viaducts. Monitoring structures in danger might enable Rijkswaterstaat to spot damages before regular inspections would and to extend the life of some of them. In vibration-based SHM, the bridges are continuously monitored with sensors. Many different types of sensors can be used, but accelerometers and strain gauges are the most common. Rytter (1993) categorised SHM into four levels:

1. Detection of damage
2. Localisation of damage
3. Severity of damage
4. Prognosis of damage

In short, an SHM technique that covers all levels is not only able to analyse existing damage but also capable of making a prediction of the remaining lifespan of a structure. A large advantage of these vibration-based structural damage detection (SDD) techniques compared to other methods like non-destructive testing is the fact that internal, hidden damages can be detected (Hou & Xia, 2021). To do this, vibrations in the monitored structure are measured. Multiple approaches exist within vibration-based SHM. Some of them use the eigenfrequencies of the structure which can be obtained from the sensor data. This approach takes advantage of the fact that the dynamic characteristics of the structure are influenced by damage: eigenfrequencies change due to a changing structural stiffness. This is confirmed by the well-known equation for calculating the eigenfrequency (ω) of a single degree-of-freedom (SDOF) system:

$$\omega = \sqrt{\frac{k}{m}} \tag{1.1}$$

where k is the stiffness and m is the mass of the structure. According to this equation, a decreasing stiffness (for example caused by a crack) decreases the eigenfrequency of the structure. So, observing a shift of the eigenfrequencies of the monitored structure indicates the structure is damaged (level 1 in Rytter, 1993).

So far, the success of vibration-based SHM in practical applications is, however, limited. Bao & Li (2021) identified four reasons for this: 1) lack of spatial density of sensors on a structure, 2) the influence of environmental and operational variabilities (EOVs), 3) uncertainties such as measurement noise and structural models and 4) the fact that damage is often a local phenomenon and may not influence the fundamental modes of the structure. Generally, these fundamental, low-frequency, modes are monitored in existing SHM methods.

This research distinguished itself from most SHM related research by focusing on local, high-frequency modes. The expectation is that small faults in the structure should be noticeable when analysing the higher-order modes but the influence of EOVs on the data is even larger in the high-frequency domain than with fundamental modes. So handling EOVs is a large challenge in this research. To identify the eigenmodes of the structure, one is only interested in the stationary dynamic behaviour, the modal vibrations of a structure. EOVs add non-stationary behaviour to the signals caused by for example traffic loads and temperature differences. These effects need to be taken into account to make the sensor data useful for selecting damage-sensitive features because the influence of EOVs on the signal is often larger than the influence of damage itself (Malekloo *et al.*, 2021).

1.1. Related Research

This thesis is the fifth in line about vibration-based SHM of the Dynamics of Structures section of the Delft University of Technology in cooperation with engineering firm Witteveen+Bos. The goal of this series of research is to develop a methodology for detecting damage in bridges on a relatively small scale. Where most literature about vibration-based SHM is on a global scale (fundamental modes), this series has focused on vibration-based SHM of higher-order modes, on the scale of bridge components or structural elements (bridge decks).

The first two theses in the series were about SHM of the Zwartewaterbrug in Hasselt, Overijssel. Milosevic (2018) looked for a 'damaged' bridge component (added mass to the bridge deck) with a model-driven approach and De Bruijn (2019) applied a data-driven approach. To handle EOVs, Milovesic introduced the concept of similarity filtering (SF), which was later adapted by De Bruijn. SF should be able to remove non-stationary vibrations caused by EOVs (mainly traffic) from the acceleration data. By applying SF, the stationary behaviour of the bridge (modal vibrations) is amplified, while non-stationary behaviour is damped. After

applying SF, De Bruijn found a strong correlation between the features and the air temperature. His dataset, however, was too limited to draw a firm conclusion about this correlation.

The theses after were about the Haringvlietbrug. The goal of Greijmans (2020) was to identify damage on an even smaller scale (structural elements) using a purely data-driven approach in a high-frequency domain (>200 Hz). SF appeared not to work in this frequency domain. So, SF was only applied successfully at the Zwartewaterbrug project. The research of Kortendijk (2020) deviated from his predecessors as he focused on the influence of temperature on the dynamic properties of the bridge. He found that the temperature distribution in the bridge is nonuniform; material characteristics, shading and the position relative to the sun influence the temperature distribution and therefore strains and stresses. The first eigenfrequency of the subsystem of interest, consisting of the asphalt, the deck plate and a bulb, can deviate around 6% within a day cycle according to Kortendijk.

1.2. Research Goal

This thesis focused on handling operation variabilities for the sake of vibration-based SHM. In the measurement campaign, all sensors were placed in healthy bridge segments. Hence, this research was not about detecting damage but focused on data normalisation and the effect of a passing vehicle on the bridge's vibrations. It was expected that similar patterns were present in the signals after applying similarity filtering as the patterns found by De Bruijn (2019). These relations were investigated further. Furthermore, it was clear from the measurements that different the variability of the dynamic response of the bridge was large when comparing different vehicle passages. In this research, the influence of vehicles on the vibrations of the bridge deck was looked into in more detail to find explanations for the differences in response. The goal of this research was defined as:

To investigate the applicability of similarity filtering on steel bridge deck structures under the influence of EOVs and to improve the understanding of the effect of vehicles on local bridge vibrations for the application of vibration-based SHM using local modes.

This research goal was achieved with the help of the following research questions:

1. To what extent is similarity filtering an effective method to remove operational variabilities from the signals at the Haringvlietbrug?
2. How is the local dynamic response of the bridge deck of the Haringvlietbrug influenced by operational variabilities?
3. What are the causes of the differences in dynamic response of the Haringvlietbrug to different vehicle passages?
4. How can the newly obtained insights be used for the sake of vibration-based structural health monitoring?

In Section 1.3, these questions are further elaborated on.

1.3. Methodology

The proposed research questions in the previous section acted as guidance for obtaining the research goal. An overview of the research process is given in the flowchart of Figure 1.2. This section goes into the methodology for answering each research question. Before being able to answer the research questions, three tasks needed to be completed: data acquisition, importing and cleaning of the data and performing a preliminary data analysis.

The data was acquired by 32 accelerometers and 12 temperature sensors. These sensors were installed by a team of Witteveen+Bos and recorded for 33 full days. Subsequently, the measurement data was imported and cleaned using existing Python scripts. The environmental circumstances (temperature measurements and weather data) of all separate measurements were added to the measurement database enabling the creation of batches of measurements with highly similar environmental conditions. A preliminary frequency analysis, time-frequency analysis and modal analysis were performed on the acceleration data to get a better understanding of it. Also the temperature data was analysed. This research was fully based on the output data

of the sensor; any input parameters of the bridge or vehicle characteristics were not available. The last pre-processing step was sample selection of vehicle passages as this was necessary for the application of multiple methods in this research.

After the preparation steps, research question 1 could be looked into. Question 1 was about data normalisation with respect to the traffic effect by applying SF. SF required the tweaking of some parameters: the length of the segments to be convolved with each other and the number of times each segment is convolved. The exact value of these parameters was obtained by trial and error by inspecting and comparing the output of SF. With applying SF, the question was also raised if sensors located in different bridge segments can be combined. Despite the fact that the segments are structurally equal, it is a possibility that the influence of EOVs is different. The goal was to assess the applicability and the boundaries of SF.

Research question 2 was about describing the variability observed in the dynamic response of the Haringvlietbrug. With data analysis, the behaviour of the bridge and its response to, for example, a semi-trailer truck was looked into. The following tools were used for the data analysis of separate vehicle passages: time-history analysis, frequency analysis and the time-frequency analysis. In addition, the signals of different sensors responding to the same passage were compared and analysed.

Research question 3 aimed to find an explanation for the large differences in the bridge response found during the previous research question. The frequency spectra of passage samples showed large variability when compared to each other. So, it appears that each vehicle excites the measured bridge segments differently. With an extensive operational modal analysis (OMA) technique, the eigensystem realisation algorithm (ERA), consistent mode shapes and the belonging eigenfrequencies were tried to obtain for separate vehicle passages. By comparing consistent modes, it was aimed to find a relation between the eigenfrequency shift and the characteristics of the passage. In addition, a semi-analytical model of the bridge deck was made to investigate the sensitivity of the dynamic response of the bridge deck to different parameters. This way, explanations for the differences in dynamic bridge response were looked for which was further explored by comparing the results of the model to characteristic load cases of the Haringvlietbrug.

In research question 4, a connection between the insight gained in the previous research questions and vibration-based SHM was created. A relation was tried to be found between the identified modes and the measurement data. The ultimate goal was to find a way to extract suitable features for damage detection from the measurement data which are not sensible to EOVs. Additionally, recommendations were made on how the results of the model can be used in order to be able to extract suitable features.

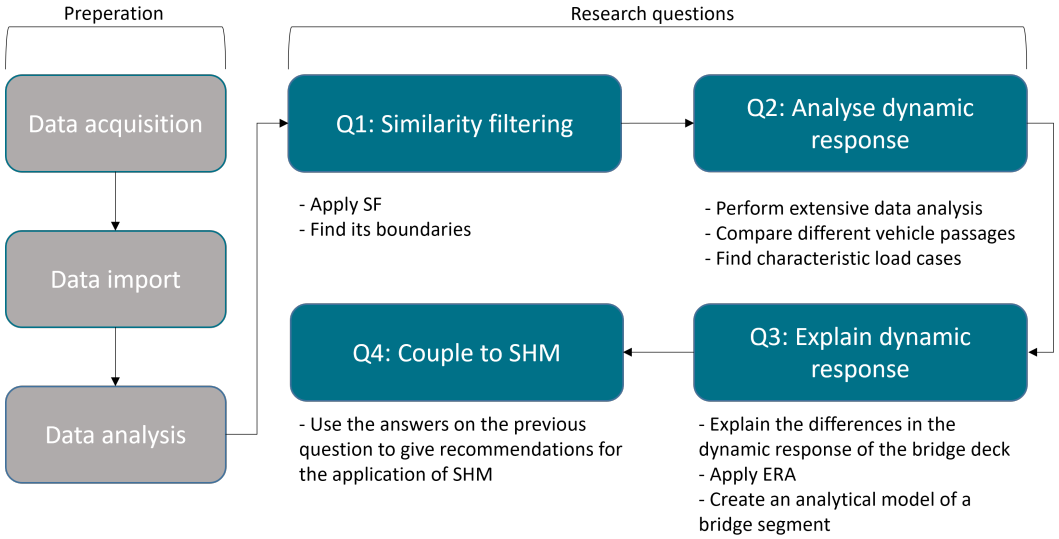

Figure 1.2: The workflow of this thesis.

1.4. Structure of This Thesis

Besides the introduction, this thesis consists of eight more chapters. Chapter 2 contains a literature review on vibration-based SHM and, in special, EOVs. In Chapter 3, general information about the Haringvlietbrug and the measurement campaign is discussed. The collected acceleration and temperature data is analysed

in Chapter 4 with multiple analysis techniques. This chapter also explains the sample selection algorithm and analyses. Chapter 5 aims to answer the first research question about similarity filtering (SF) containing both the theoretical background of the method and the application. Next, the eigensystem realisation algorithm (ERA) is introduced and applied to the data set in Chapter 6. Then, Chapter 7 presents a semi-analytical model of a segment of the bridge deck. This chapter investigates the most important parameters influencing the dynamic response of the bridge deck. Subsequently, the sensitivity of the model to its parameters is investigated based on four characteristic load cases obtained from the Haringvlietbrug measurement data in Chapter 8 in order to find the potential sources of the variability. In Chapter 9, points of discussion, conclusions and recommendation are provided.

2

Literature Review

Literature was reviewed to get a good understanding of the subject and to find out the current state of the research area. Section 2.1 gives general information about vibration-based structural health monitoring (SHM) and Section 2.2 goes into the EOVs temperature and, most extensively, traffic.

2.1. Vibration-Based Structural Health Monitoring

Vibration-based SHM is a non-destructive health monitoring technique that involves several steps. The steps and options within these steps are explained below based on Malekloo *et al.* (2021).

Excitation A large number of SHM techniques use modal characteristics of a structure. Within these techniques, one can choose to apply experimental modal analysis (EMA) or operational modal analysis (OMA). With EMA, the structure is excited artificially, for example with mass shakers or test vehicles. OMA is an output-only analysis in which the structure is merely excited by ambient loads such as wind, temperature and traffic (Farrar *et al.*, 1999). Traffic, however, cannot be seen as purely ambient load because all vehicles have a similar velocity and thus repeated frequencies (Brewick & Smyth, 2014). It is assumed that the dynamic excitation of a structure only excited by ambient loads can be modelled by a white-noise process (Brincker & Ventura, 2015). An example of an OMA technique is the eigensystem realisation algorithm (ERA). OMA techniques are easier and cheaper applicable on large structures and the necessary choice for continuous monitoring and in-service infrastructure. Only output data was available for this thesis. Alamdari (2015) emphasizes the challenge of extracting damage-sensitive features from higher-order modes of vibration because of the difficulty to consequently excite them.

Data acquisition The SHM data is collected with sensors. Many different types of sensors, active as well as passive, can be chosen. Passive sensors inflict no input energy on the structure. Examples of often used passive sensors are accelerometers, strain gauges and acoustic sensors. An example of an active sensor is a piezoelectric ultrasonic sensor. In addition, wired sensors are generally still preferred over wireless sensors because of their durability and reliability although being more expensive and more complicated to install according to Noel *et al.* (2017).

Besides the type of sensor, there are two more essential elements of data acquisition: the number of sensors and their location (Malekloo *et al.*, 2021). These are optimised in the research area optimisation of sensor placement (OSP). In many vibration-based SHM techniques, a key requirement of the sensor layout is the ability to identify damage-sensitive modes. Ostachowicz *et al.* (2019) shows that many different OSP techniques exist, increasingly more often based on the machine learning (ML) paradigm.

Data normalisation The collected sensor data needs to be normalised before it can be properly used to extract features for damage detection. Especially the effect of environmental and operational variabilities (EOV) needs to be handled. The reader is referred to Section 2.2 for more information.

Feature extraction The eventual goal of the previous steps is to be able to extract damage-sensitive features. Here, a clear distinction in the methodology of vibration-based damage detection can be made between model-driven and data-driven approaches. In addition, a combination of both systems into hybrid approaches is also possible (Figueiredo *et al.*, 2019; Gardner & Barthorpe, 2019). An example of a model-driven approach is an inverse technique where an FE model of the structure is used whose parameters are updated based on measurements. Changes in the updated parameters are subsequently used as features. Features in data-driven approaches are for example extracted eigenfrequencies or peaks in a Fourier spectrum (Gardner & Barthorpe, 2019).

Damage detection The last step of SHM is the detection of damage using the extracted features. In model-driven approaches, a changing feature indicates the potential presence of damage. Data-driven approaches often rely on ML algorithms to learn the relation between features to detect deviations.

2.2. Environmental and Operational Variabilities

One of the main challenges in SHM is handling environmental and operational variabilities (EOV) like traffic and temperature because the influence of EOVs on the signals is often of the same magnitude as the influence of small damage (Rainieri & Magalhaes, 2017). There are multiple ways of taking EOVs into account. One could choose to filter out or normalise the effects (separately) in the pre-processing phase. Another option comprises a range of data-driven approaches using pattern recognition (e.g. using ANNs in Kostić & Gül, 2017) or clustering techniques (e.g. using KPCA in Santos *et al.*, 2016). However, Malekloo *et al.* (2021) has written that the performance of the latter methods is not always sufficient, making the algorithm often only useful for the detection of severe damage. Lastly, one can choose to extract damage-sensitive features which are not sensitive to EOVs. An example of a temperature-insensitive feature is available in Deraemaeker *et al.* (2008). This paper showed mode shapes are barely affected by temperature changes. However, being more sensitive to noise makes it again less useful for detecting small damage. Since this thesis is about SHM techniques for detecting local damages, the goal was to handle EOVs in the pre-processing phase.

Four categories of EOVs for in-service structures were defined (Sohn, 2006): temperature effects, boundary condition effects, traffic (mass loading) effects and wind-induced variation effects. Boundary condition effects include for example freezing of the supports (Alampalli, 1998). For bridge decks, the most important effects were found to be temperature and traffic (De Bruijn, 2019). Hence, these two effects were investigated most thoroughly in this thesis and are discussed in more detail below.

2.2.1. Temperature Effects

Wahab & De Roeck (1997) showed that temperature has a large influence on the dynamical characteristics of a bridge. This causes the system to be time-variant. A decrease in temperature from 15 to 0 °C increased the eigenfrequencies of all inspected modes by 4 to 5%. Also Xia *et al.* (2006) and Zhou & Yi (2014) found a negative correlation between temperature and eigenfrequencies for the fundamental modes of the structure of respectively a concrete slab bridge and a steel bridge. Kortendijk (2020) found a similar negative correlation but also for subsystems of the bridge. Remarkably, De Bruijn (2019) found positive correlations between the temperature and eigenfrequencies investigating only local higher-order modes, but was unable to find an explanation for this. Peeters *et al.* (2001) showed that the correlation is dependent on the mode. He investigated the Z24 bridge which showed a negative correlation for the first mode and a positive correlation for the second mode for temperatures above the freezing point.

The equations below also suggests a negative correlation between the temperature and eigenfrequencies of a structure. The eigenfrequencies shift by a changing temperature because it affects material properties and causes thermal expansion. Rishin *et al.* (1973) showed that the Young's modulus E decreases linearly with an increasing temperature. This effect leads to lower eigenfrequencies according to the equation for the natural frequencies of a simply supported beam:

$$\omega_n = \frac{n^2\pi^2}{L^2}\sqrt{\frac{EI}{\rho A}} \tag{2.1}$$

where L is the length of the beam, EI is the bending stiffness and ρA is the mass per unit length. The other important temperature-induced effect is thermal expansion. Materials expand under increasing temperatures. Thermal expansion induce an internal axial force in a beam:

$$N = -EA\alpha_T \Delta T \tag{2.2}$$

where EA is the axial stiffness, α_T is the thermal expansion coefficient of a material and ΔT is the temperature change. This equation shows that an increasing temperature leads to an increasing negative normal force, a compression. The effect of such compression on the eigenfrequencies of a simply supported beam is given by:

$$\omega_n = \omega_n \sqrt{1 + \frac{N}{n^2 N_{cr}}} \tag{2.3}$$

where N is the axial force and N_{cr} is the critical buckling load. So, an increasing temperature leads to a negative axial force and therefore the eigenfrequencies decrease. Hence, both thermal-induced effects result in a negative correlation between temperature and eigenfrequencies.

When the temperature drops below zero, the correlation is always negative. This creates a bilinear relation between the temperature and eigenfrequencies with the inflection point at the freezing point, confirmed by multiple papers (Peeters *et al.*, 2001; Zhou & Yi, 2014). This bilinear behaviour is mainly caused by the asphalt which is highly sensitive to temperature changes (Peeters & De Roeck, 2000). According to Kortendijk (2020), the influence of the asphalt is also significant for a temperature shift above the freezing point. He showed that subsystems which included the asphalt layer were more sensitive to temperature changes than other subsystems.

It can be concluded that the data needs to be normalised with respect to temperature before it can be properly used to detect damage. Various methods have been developed to normalise the data to the bridge temperature. Just like vibration-based damage detection, these methods can be divided into model-driven and data-driven approaches. Explanations about and examples of these approaches are discussed below.

Model-driven In the model-driven approach, one can investigate the physical behaviour of all structural elements of the bridge influencing the dynamical characteristics. For example, a relation between temperature, Young's modulus and the eigenfrequencies can be looked for. Kortendijk (2020) applied a model-driven approach in which he looked for a temperature-stress/strain-eigenfrequency relation using a finite element model. Complicating factors are the non-uniform temperature distribution and the orthotropic design of the structure.

Data-driven Most literature prefers a data-driven approach to handle the temperature effect. In this approach, an algorithm establishes connections between temperature data and the identified eigenfrequencies. Many methods are suggested in literature, but the two most popular methods are linear regression analysis and support vector machine (SVM) techniques. With linear regression analysis, "a linear relation between the frequency at a certain time instant and (some of) the temperatures at the same time instant is estimated by least squares" (Peeters *et al.*, 2001). Thermal dynamics of the bridge are taken into account in this method by implementing a temperature phase shift. The model is called an ARX model: Auto-Regression with eXogenous variables. It consists of an auto-regressive output and an exogenous input part for example proposed by Ljung (1999):

$$y_k = a_1 y_{k-1} + \cdots + a_{n_a} y_{k-n_a} = b_1 u_{k-n_k} + b_2 u_{k-n_k-1} + \cdots + b_{n_b} u_{k-n_k-n_b+1} + e_k \tag{2.4}$$

where y_k is the output at time k, u_k is the input and e_k is an error term. In the case of temperature normalisation, the output is an eigenfrequency and the input is the temperature. Ni *et al.* (2005) presented a method to normalise the signals taking into account the mean value of numerous temperature sensors using an SVM technique.

2.2.2. Traffic Effects

The influence of the traffic effects seems to be limited for fundamental modes but increases for higher-order modes according to Sheibani & Ghorbani-Tanha (2021). The traffic effect brings two problems along: disturbance in the signals (affecting the white-noise assumption) and the mass loading effect. Normalising the latter is a challenge because the effect is dependent on the mass of the vehicle relative to the magnitude of the bridge (Sohn, 2006). Hence the dynamic response of the bridge differs for each passing vehicle. Each vehicle

is an addition of mass to the bridge (this explains the term 'mass loading effect'). Therefore, the resonance frequencies correspond to a coupled interacting system between bridge and vehicle, but not to the bridge itself (those frequencies are called instantaneous eigenfrequencies). This was observed by Furtmüller *et al.* (2020) who found a relative change in eigenfrequency of 0.5% for the fundamental modes of the Lueg Bridge due to the mass loading effect. So, the influence of the mass loading effect is smaller than the temperature effect for middle- and long-span bridges but it can still be of importance when detecting small structural damages. For short-span bridges, the effect can be of more significance: Kim *et al.* (1999) reported a relative shift in eigenfrequency of 5.4%.

The other problem is the disturbance in the signals. A heavy truck causes severe vibrations in the bridge. In fact, the traffic effect is the most important short-term time-variant load on the structure. Therefore by removing the effect of the traffic from the signals, the signals should be close to a white-noise process.

Removing the influence of vehicles from the signal is complicated due to its large variance. If the input is known, this can be used to normalise the data; Cross *et al.* (2013) found a linear relation between the traffic load and the fundamental eigenfrequency of a suspension bridge. This can, however, not be applied in this research since the traffic loads were unknown. Many tend to investigate the traffic effect on structures by creating an analytical or numerical model of the vehicle-bridge interaction. Examples are Huang (2012) and Zhu *et al.* (2018) for road bridges and Song *et al.* (2018) for railway bridges. These papers have in common that they focus on fundamental modes. In addition, some of the models need vehicle characteristics as input parameters which were not available for the Haringvlietbrug project. Zhang *et al.* (2018) focused on local mode shapes of a concrete box-girder railway bridge. He compared a detailed FE model to experimentally obtained data and found that the measurement data was limited useful to detect local modes because of a too low spatial density of the sensors (a total of nine sensors were available) and the dense spacing of the local vibration modes which made them difficult to distinguish.

Also output-only system identification models can be used to get a better understanding of the traffic effect. Brewick & Smyth (2013) used multiple OMA techniques to investigate the effect of traffic-induced local vibrations on damping estimates and compared the results to a FE model. They found that OMA methods on real-world data are limited reliable for obtaining damping estimates if no a priori knowledge of the traffic is available. This is caused by the non-ambient quasi-periodic character of the traffic input whereas OMA methods traditionally require ambient, broad-banded excitation. Traffic load is however often not broad-banded since the energy of the load of vehicles is concentrated at different frequencies.

An often used tool in modal analyses is the modal assurance criterion (MAC). The MAC is a statistical indicator of the extent similarity between two mode shapes. The MAC value of two mode shapes is calculated according the following equations:

$$MAC(\phi_k, \phi_l) \triangleq \frac{|\phi_k^H \phi_l|^2}{||\phi_k||_2^2 ||\phi_l||_2^2} \tag{2.5}$$

where ϕ is a modal vector and H indicates the Hermetian transpose. The MAC value is bounded between 0 and 1; a value of 0 indicates completely non-consistent mode shapes and a value of 1 indicates fully consistent mode shapes (Pastor *et al.*, 2012).

Milosevic (2018) and De Bruijn (2019) proposed the concept of similarity filtering (SF). In this purely data-driven method, they aimed to filter out the traffic effect by amplifying similarities in the data while damping out any differences. The background of this concept is further discussed in Chapter 5.

2.2.3. Influence of Tyre and Pavement Characteristics on Bridge Vibrations

Not only the traffic effect but also the interaction between characteristics of the tyres of the vehicles and characteristics of the pavement of the bridge deck influences the vibrations of the bridge. Experiments show that the vertical accelerations in the deck increase with the amplitude of irregularities of the pavement (Camara *et al.*, 2017). They also wrote that the frequency content of the pavement irregularities significantly influence the bridge vibrations; if the frequency content is close to an eigenfrequency of the bridge, the magnitude of the vertical acceleration response of the bridge increases.

Also the vehicles' tyres influence the dynamic response of the bridge. A large variety exists within tyre parameters; ranging from standard tyre characteristics (Karakus *et al.*, 2017; Subbian *et al.*, 2019) to non-uniformities in a worn tyre (Smith & Garcia, 2013). The study of Karakus *et al.* (2017) focused on finding a relation between some tyre characteristics and the eigenfrequencies of the tyre. They found that the air

pressure in the tyre has a positive linear relation with the eigenfrequencies while the coefficient of friction between the tyre and pavement and the vertical force showed a low correlation with the eigenfrequencies of the tyre. According to that research, the first six eigenfrequencies of a standard car tyre range from 60 to 250 Hz. Subbian *et al.* (2019) showed that the profile of the tyres produce vibrations above 500 Hz if the vehicle has a velocity of 80 km/h so this effect can be neglected for the current research as the frequency range of interest is between 50 and 250 Hz. There exist tyre non-uniformities which have peak frequencies within the frequency range of interest (Smith & Garcia, 2013). Especially 3rd and 4th order tyre radial run-out can cause additional vibrations above 50 Hz.

2.2.4. Influence of Vehicle Velocity and Acceleration on Bridge Vibrations

Many works have been carried out to study the effect of different vehicle velocities on the dynamic response of bridges. Multiple authors concluded that the response of a simply supported beam increases with an increasing vehicle velocity. Yu *et al.* (2018) came to this conclusion with a numerical model and Shafiei (2021) with an analytical model. However, the extent of the shift of the response of the bridge is very different (20% and 300% respectively) for a similar velocity change. Both papers compared three discrete velocities. Yu *et al.* (2018) observed more or less the same behaviour when changing the vehicle acceleration, but the effect was smaller than with a changing velocity.

Authors taking a more continuous velocity range into account observed another phenomenon: the relation between vehicle speed and acceleration response is not always positive correlated. They found that critical velocities exist where the vibrations of the bridge can become excessive (Pisal & Jangid, 2016). Most research to critical velocities is performed on railway bridges where they occur when the loading frequency by the spacing of vehicle axes is close to an eigenfrequency of the bridge. Wang *et al.* (2003) found the following relation to obtain the critical velocity v_{cr}:

$$v_{cr} = \frac{\omega x_v}{2l\pi} \tag{2.6}$$

where $l = 1$ for the dominant first-order effect, ω is an eigenfrequency of the beam and x_v is the axle spacing. The same phenomenon can occur on road bridges (Brady *et al.*, 2006). They found that the dynamic amplification factor (DAF) increases significantly at certain velocities of two- and three-axle vehicles. The same happens when considering a single point load although less significant. In the latter case, the combination between velocity and road roughness can influence load frequency. These results were also obtained by Sawant *et al.* (2011), who performed a research to the deflection of the pavement underneath the main landing gear of an airplane. At high vehicle velocities the DAF decreases because the load needs less time to pass the beam than it takes for the fundamental modes of the beam to vibrate once according to Brady *et al.* (2006).

3

The Haringvlietbrug Project

This chapter provides some general information about and the design of the Haringvlietbrug in Section 3.1. Next, Section 3.2 goes into the measurement campaign held at this bridge explaining how all measurement data was acquired and, in Section 3.3, all measurements and weather data is summarised in the measurement matrix.

3.1. General Information and Design

National highway A29 goes over the Haringvlietbrug, creating a direct connection between the islands Hoeksche Waard and Goeree-Overflakkee (both in South Holland) and North Brabant. Figure 3.1 provides a map of the surroundings of the Haringvlietbrug and shows that the bridge is an important exit road southwards from Rotterdam and its port. The bridge was delivered in July 1964, replacing a ferry by providing the first road connection between Goeree-Overflakkee and the mainland.

Figure 3.1: A map of the surroundings of the Haringvlietbrug (source: Port of Rotterdam).

The span of the Haringvlietbrug, a box girder bridge, is 1220 m divided over ten identical segments spanning 106 m each and a bascule bridge as visible in Figure 3.2. All bridge segments exist of twelve compartments, separated by diagonal structural elements and with four frames each (2167 mm centre-to-centre). Figure 3.3 shows the cross-section of the bridge. The main girder is a duct profile of 11.5 m x 5.33 m. There is a cantilever of 7 m on both sides of the duct, regularly supported by the external and internal diagonals. The steel bridge has a 2x2 lane layout with a design maximum speed of 100 km/h. In addition, a service road meant for pedestrians, bicycles and agricultural vehicles is located on the eastern side of the bridge.

The bridge deck consists of multiple layers. It is supported by beams in the transverse direction at each frame (so 2167 mm centre-to-centre). On top of those beams is a steel deck plate with a thickness of 10 mm, stiffened by longitudinal bulb profile ribs with a spacing of 300 mm. There are some more layers on top of the

deck plate, from bottom to top: Mistral C (4 mm), asphalt (30 mm), Parafor Ponts (4 mm) and on top pervious concrete ('zoab', 30 mm). Mistral C and Parafor Ponts together form a waterproof layer.

Figure 3.2: Exterior view of the Haringvlietbrug (source: Rijkswaterstaat).

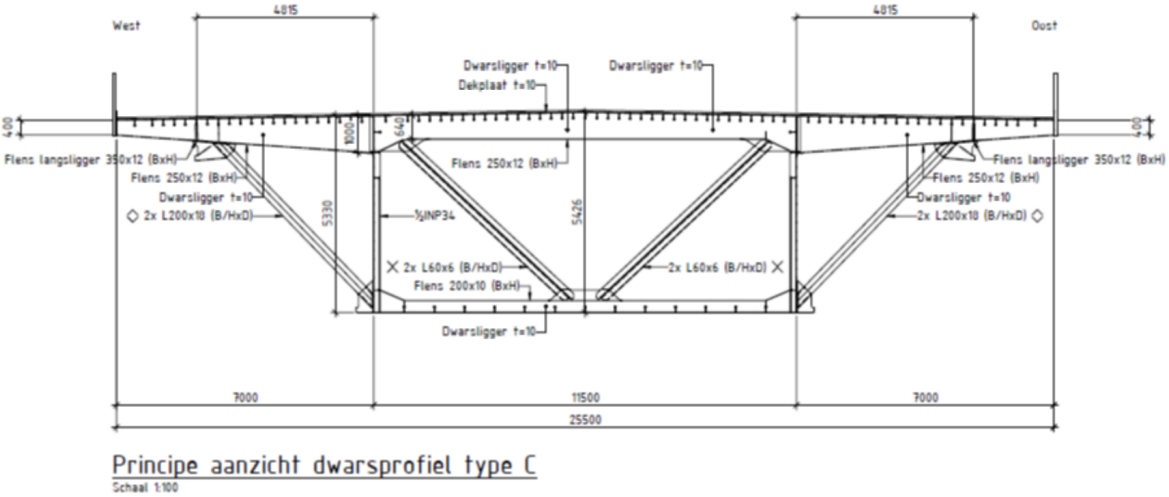

Figure 3.3: Cross profile of the Haringvlietbrug.

Safety measures Rijkswaterstaat was forced to take action in order to extend the service life of the Haringvlietbrug till renovations take place in 2023. This was necessary because clamps holding aluminium plates were shaking loose by the passing traffic and opening of the bascule bridge. To minimise this effect, Rijkswaterstaat took multiple measures (as visible in Figure 1.1): decreasing the maximum speed to 50 km/h, narrowing the driving lanes and limiting the number of times the bascule bridge opens. These measures lead to significant nuisance for the road users.

3.2. Data Acquisition

For the measurement campaign, 32 accelerometers and 12 temperature sensors were relocated from their former locations at the Haringvlietbrug. They were moved to their new locations on October 7, 2021. The measurement campaign was ended on November 10, 2021, yielding a total measurement time of 33 full days.

In addition, the 4 temperature sensors which were already placed at the cantilever on the east side of the bridge were not relocated and continued to record. Figure 3.4 shows the approximate longitudinal location of the sensors, which were all passive.

Figure 3.4: Aerial picture of the Haringvlietbrug. The approximate location of the sensors is indicated in cyan (source original picture: Rijkswaterstaat).

3.2.1. Accelerometers

The KAE-005-5-1 accelerometers have a sampling frequency of 1 kHz and recorded 15 minutes of each hour for four week and their data was stored as TDMS files. The location of all accelerometers is shown in Figure 3.6. A more zoomed-out view of the sensors can be seen in Appendix Figure A.1. The latter figure shows the location of the sensors relative to the traces of the traffic. The first step of the accelerometer placement was to glue mounting rings to the structure at the desired locations at the transverse beams or at $\frac{1}{4}$, $\frac{1}{3}$ or $\frac{1}{2}$ of the span of the bulbs and secure them with duct tape. All sensors were magnetically fixed to the mounting rings. A picture of a mounted accelerometer is shown in Figure 3.5a. The location of the sensors was chosen that way that they were able to detect the fundamental modes of the bulbs. The sensors were located in two different bridge segments which were structurally identical and believed to be undamaged. Also the layout of the sensors in both compartments was largely identical. Below is a short description of the placement of the accelerometers.

Accelerometers 1-3 were in the z-direction and attached to a bulb below a closed road segment. Accelerometers 4-19 and 22-29 were also attached to bulbs and in the z-direction, but this part of the road was in use. Sensors 20 and 21 were not attached to a bulb but attached to the bridge deck in between two bulbs. Sensor 30 was placed at the wall of the duct. Accelerometers 31 and 32 were both located at the middle of a bulb and were the only sensors in the y-direction.

When removing the accelerometers from the bridge, the connections of three sensors were noted as rogue. The mounting rings of sensors 1 and 8 had come loose from the structure and the mounting ring of sensor 5 was crooked. Therefore, the data of these sensors were disregarded.

3.2.2. Temperature Sensors

A total of 16 ATAL TEP-102 Pt1000 temperature sensors recorded the inside and outside temperature of the monitored bridge section continuously with a sampling frequency of 1 measurement per 5 minutes. They were attached to the bridge with duct tape as shown in Figure 3.5b. The sensors have a resolution of 0.3 °C and an accuracy of 1.0 °C. The location of the temperature sensors is shown in Figure 3.7.

Sensors 1, 5, 7 and 11 were attached to the bottom of the deck plate and sensors 6 and 8 to the bottom of the bulbs. Sensor 2 measured the temperature of the transverse beam and sensor 12 of the outside strut. Sensors 4 and 13-16 measured the duct's wall and floor temperature. Next, sensor 3 measured the air temperature inside the duct. Sensor 9 measured the temperature of the top layer of the asphalt while sensor 10 measured the temperature of the bottom layer of the road surface.

(a) Accelerometers

(b) Temperature sensors

Figure 3.5: Mounting of the sensors at the Haringvlietbrug for the current measurement campaign.

3.2.3. Weather Data

Weather data from October 7 till November 11, 2021 was retrieved from the Royal Dutch Meteorological Institute (KNMI). The Haringvlietbrug is located approximately in the middle of three weather stations: Rotterdam, Wilhelminadorp and Woensdrecht. To obtain the weather data at the Haringvlietbrug, the data of the adjacent stations was interpolated. This research used the following weather measurements: temperature, precipitation, sun availability, humidity and wind speed. The hourly data was coupled to the acceleration data and the bridge's temperature resulting in an extensive database. Three assumptions were made: 1) an hour was marked as wet if precipitation was measured in two or three weather stations and a minimal amount of 0.5 mm, 2) an hour was marked as sunny if the sun was shining at two or three weather stations with a minimum duration of 30 minutes and 3) the weather data was scaled to a 15-minute length, equal to the duration of the hourly acceleration measurements.

3.3. Measurement Database

All acquired data was added to a database. This database showed, besides the date, time and measurement ID, the weather characteristics and the bridge's temperatures as explained in the previous section. Since all acceleration measurements have a duration of 15 minutes, the mean temperature of the temperature sensors over the same 15 minutes were included in the database.

The database served two goals: firstly, it gave a general overview of all available measurements making samples with specific characteristics easy to find when necessary. Secondly, the database enables the clustering of measurements taken during highly similar environmental circumstances. These clusters of measurements serve as an important validation method for the techniques performed in this research as one would expect that measurements taken during highly similar weather conditions provide similar results as well.

The clusters were generated as follows. The measurement database was normalised in order to make all the entries the same order of magnitude and all wet measurements were removed because of their large uncertainty. The effect of rain on the dynamic properties of the structure was beyond the scope of this research. As the temperature of asphalt is of large influence on the eigenfrequencies of the bride deck, these sensors were prioritised (the entries were multiplied by 2). Next, the Euclidean distance between all measurements was obtained and clusters of measurements were formed if the Euclidean distance between each other was lower than 0.1.

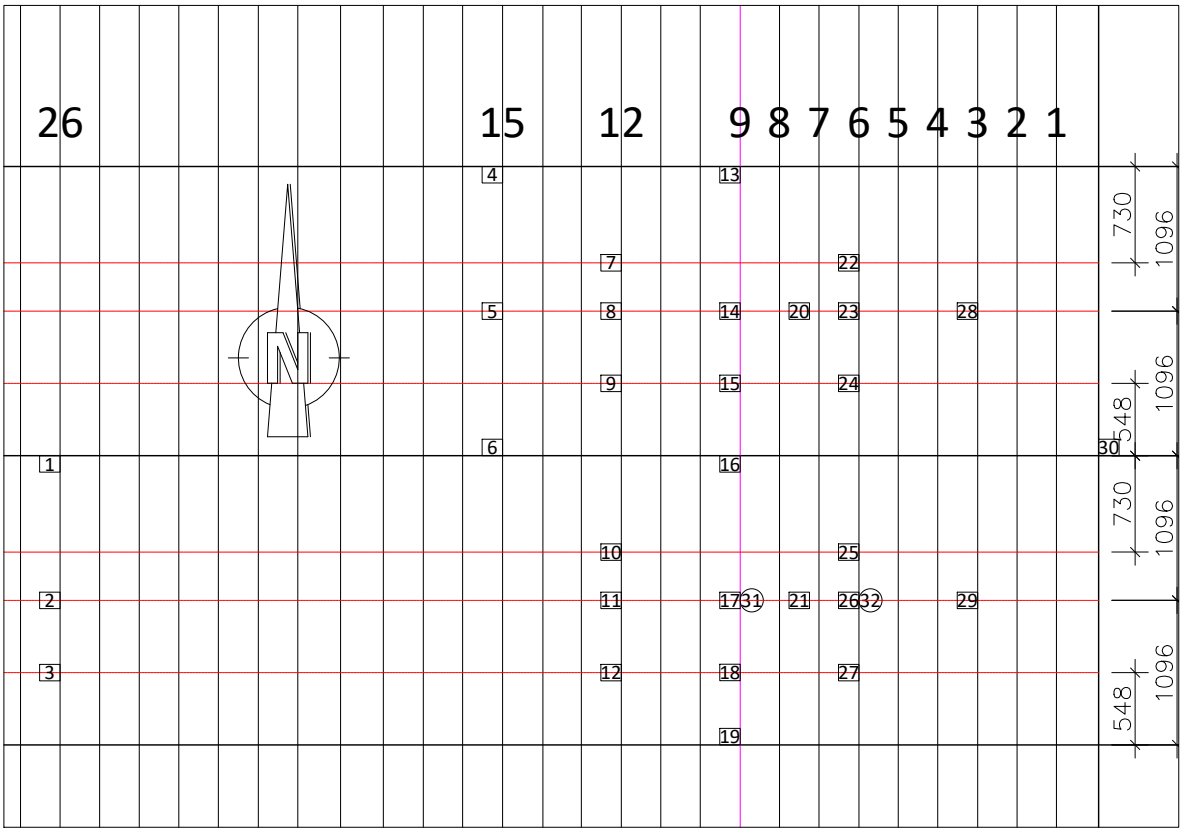

Figure 3.6: Top view of the accelerometer layout. All squared numbers are sensors in the z-direction and the circular numbers in the y-direction. The vertical lines and the other numbers are the bulbs, the horizontal black lines are the transverse beams and the red lines are guiding lines. The pink line is the alignment of the left wheels of heavy trucks.

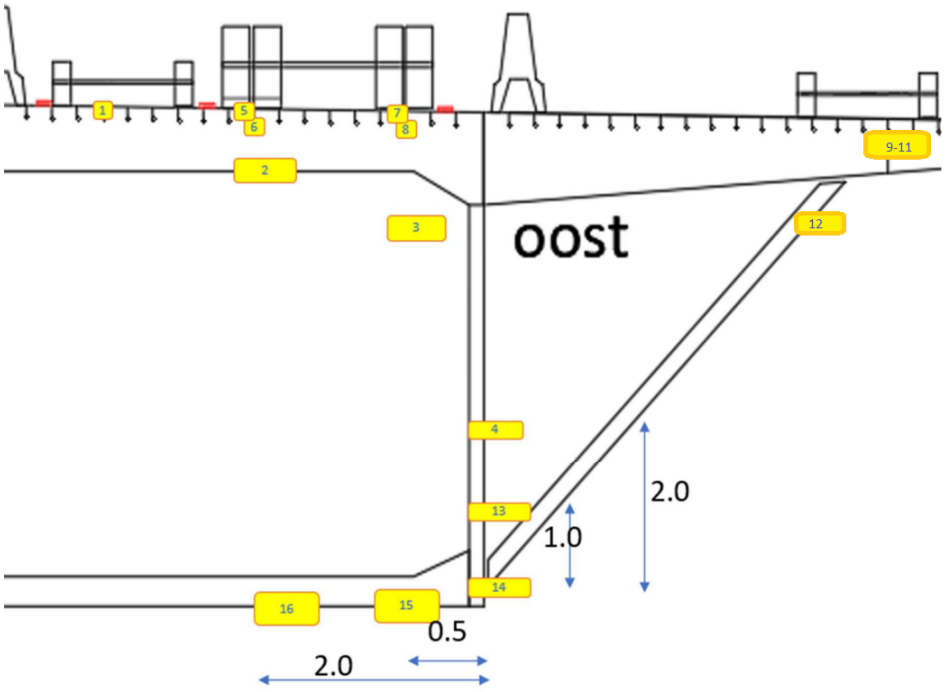

Figure 3.7: The temperature sensor layout.

4

Data Analysis and Pre-Processing

This chapter provides a first analysis of the collected data. First the acceleration data is analysed with a frequency analysis, a time-frequency analysis and a modal analysis in Section 4.1. Section 4.2 gives a first analysis on the temperature data. In Section 4.3, the important pre-processing step sample selection is explained and the samples are analysed.

4.1. Acceleration Data

The acceleration data was imported in Python with an already available script made by De Bruijn (2019) and stored as pickle after subtracting the mean of each signal. Figure 4.1 shows the graph of acceleration data of four sensors in the time domain of a 15-minute measurement. For the acceleration response of all sensors, the reader is referred to Appendix Figure A.2. The shown accelerometers recorded all in the z-direction and were attached to a bulb. In the plots, the peaks represent the passage of vehicles. Each separate passage is visible in the recordings of all sensors, though varying in magnitude.The largest measured acceleration response was approximately 0.5 m/s^2 and as expected, the sensors placed directly below the driving lanes measured a larger response than sensors located further away. Multiple data analysis techniques were applied to the signals, all discussed below.

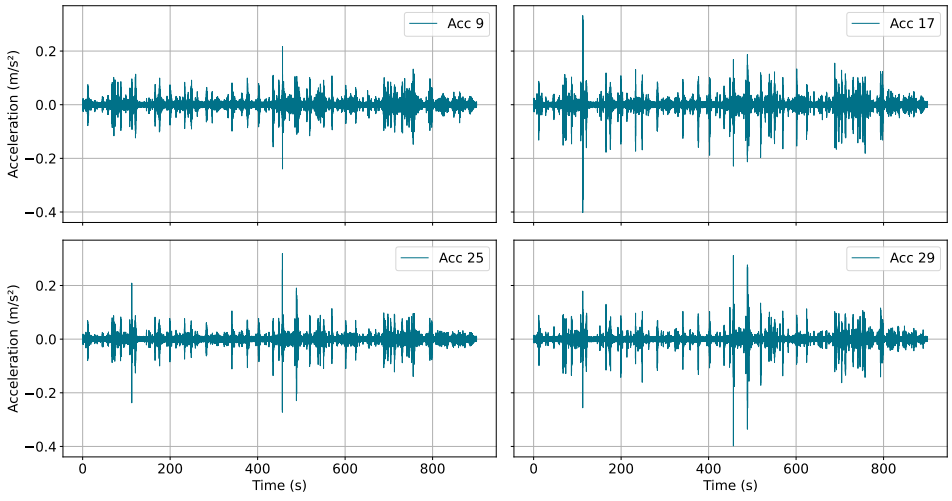

Figure 4.1: Raw acceleration data of sensors 9, 17, 25 and 29 recorded on the 11th of October at 5 AM.

4.1.1. Frequency Analysis

The first analysis was inspecting the frequency spectrum of multiple signals of all sensors using the Fourier transform (FT). The Fourier spectra of sensors 9, 17, 25, 29 are shown in Figure 4.2 and the spectra of all sensors in Appendix Figure A.3. The plots display a maximum frequency of 300 Hz since higher frequencies

are beyond the scope of the thesis. The four spectra show large similarities; the largest frequency response is below 50 Hz. Only sensor 29 has a relatively smaller response in this area. The domain above 50 Hz of the spectra is characterised by some smaller peaks but are rather constant in magnitude.

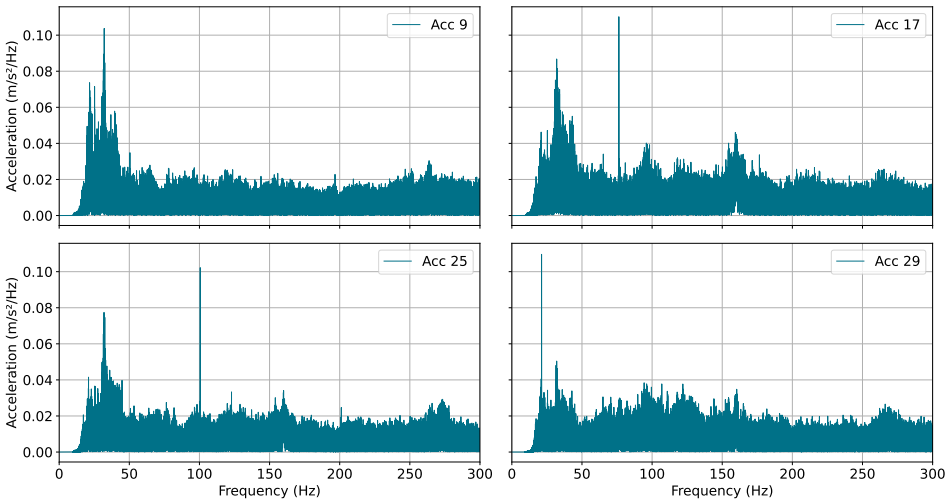

Figure 4.2: Fourier transform of sensors 17 and 31 recorded on the 11th of October at 5 AM with a high-pass filter of 20 Hz and over a frequency domain from 0 to 300 Hz.

In all spectra, narrow spikes with a relatively large magnitude are visible. Such spikes are not expected in a frequency spectrum of a bridge structure but were also detected by Greijmans (2020) who was using the same accelerometers. The following is observed concerning these spikes:

- The spikes are present in all sensors, but sometimes equal in magnitude with the rest of the signal making them less noticeable.
- The spikes are narrow: they have a bandwidth of approximately 2 Hz.
- Below 300 Hz, two spikes were observed; the first and largest one between 0 and 100 Hz and the second on at exactly twice the frequency of the first spike. More spikes were observed above 300 Hz.
- The spikes are time-variant: Greijmans (2020) found a correlation between the frequency and the air temperature. The spikes shift over a maximal frequency range of approximately 10 Hz when comparing measurements from different moments in time. Also the magnitude of the spikes is time-variant.
- For all sensors, the spikes are located at the same frequency in the new measurement campaign as in the old measurement campaign at the Haringvlietbrug despite all sensors being relocated. Moreover, this research detected the same spikes in the dataset of the Zwartewaterbrug although smaller in magnitude. Also in that measurement campaign the same accelerometers were used.

From the above points, it is clear the spikes in the frequency spectrum of the signals were not caused by the structure of the bridge itself. This has two reasons: one would expect that the peak of a structural response is wider because a narrow peak indicates damping-free vibrations while damping is always present in a structure. Secondly, the spikes are located at approximately the same frequency in three different measurement campaigns at two different bridges. Lok, owner of the accelerometers and supporting staff member at the University of Twente, found that the sensors have an eigenfrequency of around 2000 Hz. The spikes in the frequency range of interest result from aliasing (Z.A.J. Lok, personal communication, November 2021). The spikes do not influence the results of most analysis techniques but it always need to be checked according to Lok.

4.1.2. Time-Frequency Analysis

A time-frequency analysis of the acceleration data was performed using a continuous wavelet transform (WT). The FT assumes signals are periodic or infinite and loses therefore all information about the time domain. The advantage of WT is that it is able to perform a frequency analysis while maintaining the timestamps

because wavelets are finite and non-periodic. Figure 4.3 shows the WT using analytic Morlet wavelets of the acceleration data of sensor 17 as shown in Figure 4.1. As visible in the figure, stationary vibrations were observed around 15 Hz and 30 Hz. In the high-frequency domain (Figure 4.3b), only vertical lines are visible indicating no stationary vibrations were present. The large-magnitude vertical lines are located at large acceleration responses (e.g. at $t = 8$ min). The acceleration peak was caused by a passing vehicle; a high force during a short moment in time. The figure suggests that a passing vehicle can be modelled as an impulse force, the theoretical situation where all frequencies of a structure are excited, which is checked in more detail later this chapter.

Since this research focused on high-frequency excitation, the results of the WT are not as hoped for as no high-frequency stationary behaviour was found. This might be caused by a characteristic of the WT: high frequencies have better time resolution but a worse frequency resolution than low frequencies (Mathworks, n.d.). So being interested in stationary high-frequency events, continuous WT might not be a suitable data analysis technique to find stationary behaviour in an entire measurement.

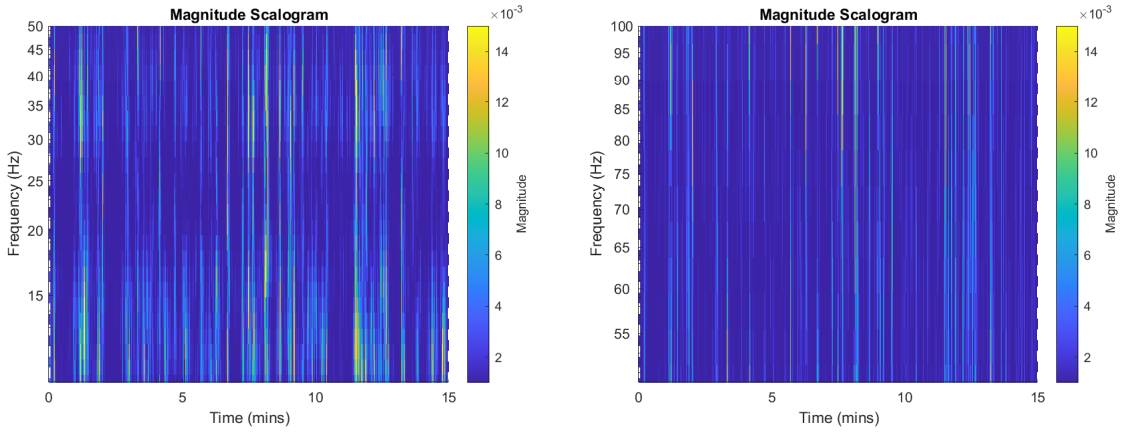

(a) 10-50 Hz (b) 50-100 Hz

Figure 4.3: Scalogram of the wavelet transform of sensor 17 recorded on the 11th of October at 5 AM.

4.1.3. Modal Analysis

A frequency domain decomposition (FDD) of the acceleration data was performed in order to identify modes of the structures. FDD is an operational modal analysis (OMA) technique. The peaks in the resulting singular value spectrum correspond to the mode shapes of the structure. The acceleration data of six sensors (14, 15, 20, 22, 23 and 24) were fused. These were all sensors in the z-direction, closely grouped and attached to a bulb. The data was split up into segments that served as input for the FDD. An algorithm written by De Bruijn (2019) selected consistent modes in each singular value spectrum. Figure 4.4 shows an example of such a spectrum. Only the first two singular values are shown since the magnitude of the others were insignificant compared to these. A peak was labelled as consistent if the MAC value within the whole peak (within a frequency range of 0.5 Hz) was larger than 0.90. If not, a peak in the singular value spectrum covered multiple modes which indicates it is not a physical mode.

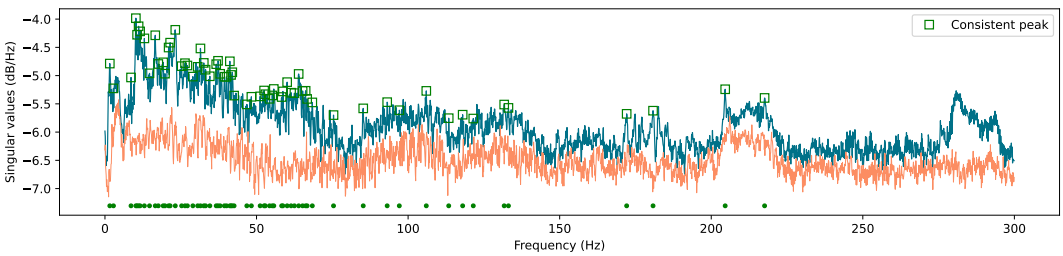

Figure 4.4: Singular value spectrum of sensors 14, 15, 20, 22, 23 and 24 recorded on the 11th of October at 5 AM.

All the consistent modes of each segment were summed which resulted in the histogram shown in Figure 4.5a. A high concentration of consistent modes was observed below 50 Hz, around 60 Hz and around 95 Hz. Since this research focused on higher-order modes, the consistent peaks below 50 Hz were ignored. It is expected the peaks found around 60 and 95 Hz belong to local modes of the bulbs. This is empowered by the consistent peaks of the transverse beams (Figure 4.5b) as far less activity is present around 60 and 95 Hz.

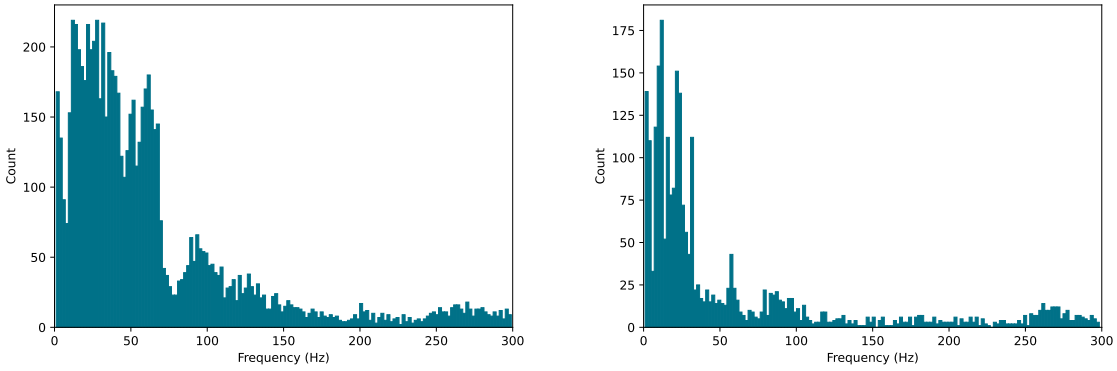

(a) Bulbs: sensors 14, 15, 20, 22, 23 and 24

(b) Transverse beams: sensors 4, 6, 13, 16 and 19

Figure 4.5: Histogram of consistent modes.

4.2. Temperature Data

The temperature data was obtained using 16 temperature sensors. The mean temperature of these sensors during the entire measurement campaign is shown in Figure 4.6. For the exact location of the sensors, the reader is referred to Figure 3.7. The temperature fluctuates in a clear day and night cycle. Besides, the sensors measured on average lower temperatures during November than October. During the measurement campaign, no single sensor recorded a temperature below the freezing point.

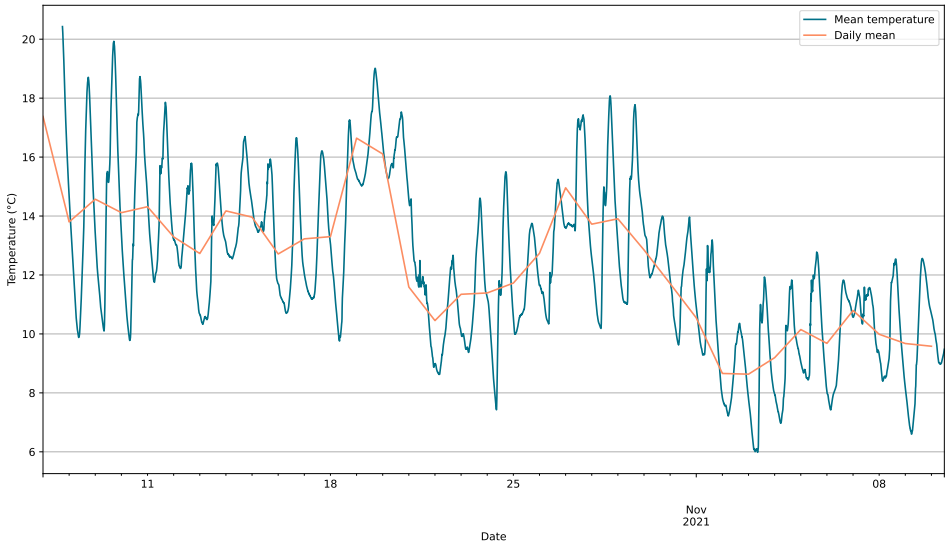

Figure 4.6: Mean temperature of all temperature sensors and the daily mean temperature recorded from the 8th to the 12th of October.

Figure 4.7 zooms into the measured temperature of all sensors on four days. The temperature was most scattered during the warmest moments of the day and was most uniform just before dawn. Three sensors sometimes showed outliers: the temperature of the eastern wall of the box girder (top, middle and to a lesser extent bottom sensors) increased excessively on mornings when the sensors were in direct sunlight. In the afternoon, however, these sensors showed relatively low temperatures.

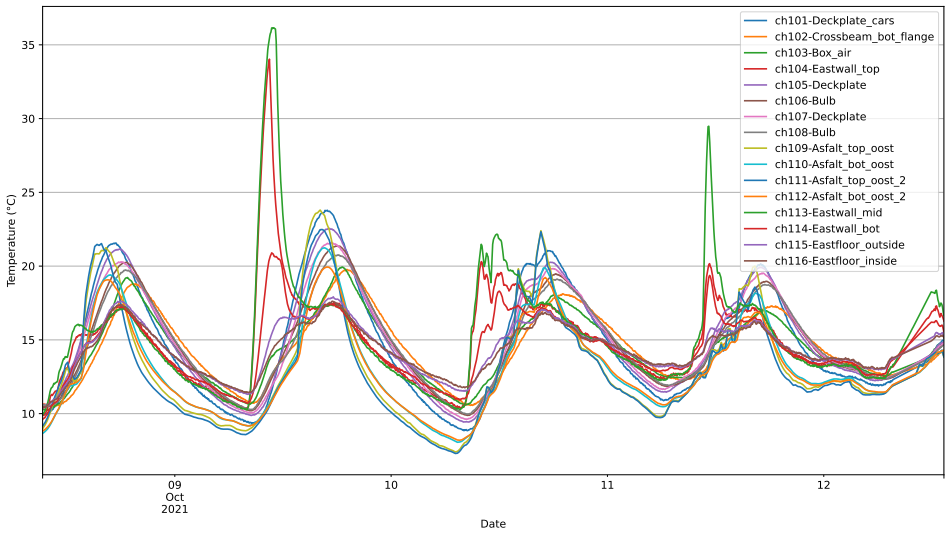

Figure 4.7: Temperature data of all temperature sensors recorded from the 7th of October to the 10th of November.

4.3. Samples of Vehicle Passages

This section focuses on separate vehicle passages. Firstly, an algorithm for passage recognition and sample selection is explained. Then, different combinations of passages and sensors are analysed after which the conclusions are given.

4.3.1. Sample Selection

In the following of this thesis, it is important to recognise vehicle passages in the data automatically and to select suitable samples. This was necessary for similarity filtering (SF), eigensystem realisation algorithm (ERA) and the comparison of load cases in Chapter 8. Two different kind of samples were selected: the samples needed for SF and ERA began right after the vehicle left the bridge segment and the samples needed to compare with the results of the semi-analytical model also started when the vehicle entered the bridge segment. The sample selection procedure is explained below based on the former type of sample.

The samples for SF and ERA were selected based on two criteria: the sample starts right after the passage of a vehicle and no other passage is allowed during the course of the sample. The latter criterion is necessary because of the mass loading effect (as introduced in Subsection 2.2.2). The mass loading effect causes a temporary change of eigenfrequencies of the structure because the structure forms a system with the added mass (a passing vehicle in this instance) which is time-variant. On the other hand, the presence of these passing vehicles is necessary to excite the bridge, otherwise only ambient forces would be present. In that case, it would be possible not all modes are excited. The sample should stop after the vibration has damped out. The time between the start and end point was determined to be minimal 2 seconds for most passages. Figure 4.8 shows an example of two selected samples. Sample selection involved the following steps:

1. All passages with a peak acceleration of more than 0.1 m/s^2 were identified with a peak finding algorithm for sensors 22 and 27. With this data, also the velocity of all vehicles was estimated.
2. The start time of the sample was set at the moment the vehicle has left the bridge segment using the estimated velocity. The end time was set at the start time plus the chosen sample length.
3. A sample was deleted if also another peak was selected during the length of the sample or if the standard deviation of the sample increased or was constant during the length of the sample or if the estimated vehicle velocity was not between 10 and 100 km/h.
4. All remaining samples were saved and the process was repeated for another 15-minute measurement.

4.3.2. Analyse Different Passages

In this section, multiple vehicle passages recorded by the same sensor are compared to each other. A total of 12 passages were selected to analyse from two 15-minute measurement on the 11th of October at 5 and 6 AM.

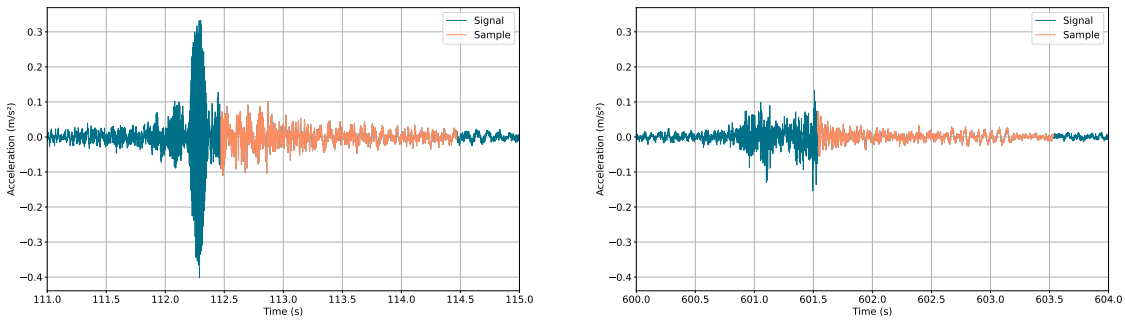

(a) High peak acceleration

(b) Low peak acceleration

Figure 4.8: The acceleration signal and the selected sample of sensor 17 of two passages recorded on the 11th of October at 5 AM.

Four of them are shown in Figure 4.9. In addition, passage 1 and 2 were further analysed with a continuous WT (Figure 4.10). The influence of environmental variabilities were neglected since the passages were extracted from two adjacent measurements both before dawn. The characteristics that stand out are explained below:

- The acceleration response was different for different passages; a large variety existed in peak acceleration (0.1 to 0.4 m/s^2), the shape of the peak and the amount of peaks.
- The spectrum of most passages showed a peak around 11 Hz. This peak was also visible if no vehicle was close to the sensor (only ambient forces were present). The peak is expected to be a dominant fundamental eigenfrequency of the Haringvlietbrug.
- Except from this peak at 11 Hz, the spectra of the passages are significantly different. However, most spectra are characterised by two energy fields: the first one lies between 0 and 50 Hz and the second one lies between 75 and 250 Hz. Especially considering higher frequencies the dominant frequency varies. Some passages even have either no clear or a wide energy field in the latter frequency domain while other passages have multiple high-energy frequency bands.
- Analysing these 12 passages, a positive correlation might exist between the magnitude of the peak acceleration and the magnitude and distinctiveness of the peak in the frequency domain from 75 to 250 Hz.
- The wavelet transform of passage 1 and 2 also shows a dominant frequency component around 150 to 200 Hz. With an increasing peak acceleration, the difference between the magnitude of the dominant frequency component and the other frequency components also increases. Furthermore, this dominant frequency component is also visible in the data a couple of seconds before and and couple of seconds after the actual passage.

Car Experiment Greijmans (2020) conducted a car experiment on the Haringvlietbrug to investigate the responses to different vehicle passages more in depth. Two different cars passed the bridge and sensor set-up twice. The experiment was conducted before the safety measures were taken at the Haringvlietbrug. Car A had the first run a velocity of 110 km/h and the second run 130 km/h. Car B had a velocity of 110 km/h during both runs. It should be noted that only four samples were available in the research so no hard conclusion could be drawn and that the accelerometers were located in the y-direction while, in this research, they were located in the z-direction.

The acceleration response of the car experiment looked similar for each passage. Only the 130 km/h passage was different: an approximately twice as large acceleration amplitude was measured. Figure 4.11 shows the frequency response of each passage. The responses show large variation in both dominant frequency and amplitude. There are, however, also similarities; all spectra show a peak (or a cluster of peaks) around 250 Hz and both passages of car A produced a peak around 340 Hz.

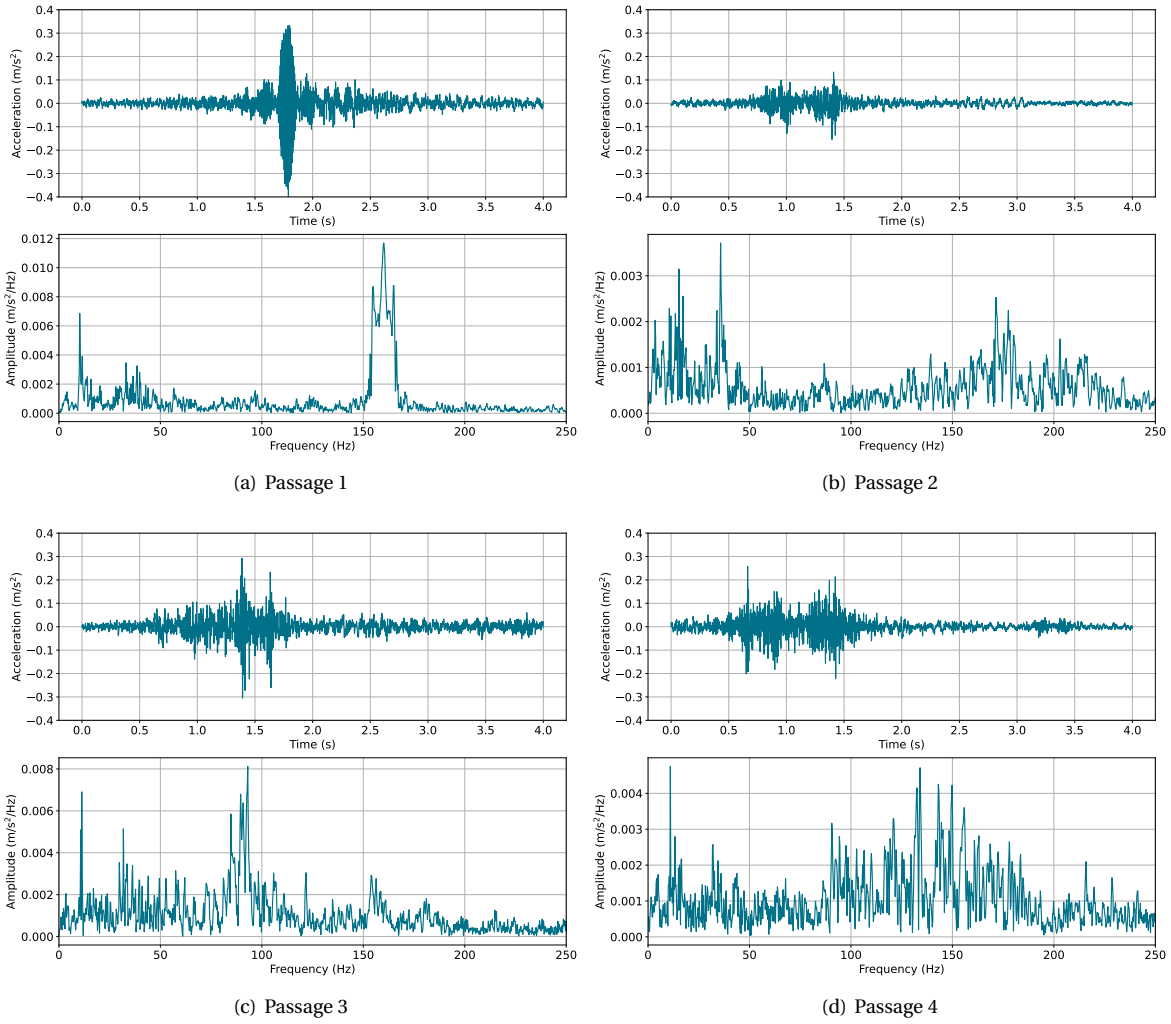

(a) Passage 1

(b) Passage 2

(c) Passage 3

(d) Passage 4

Figure 4.9: The acceleration and frequency response of four passages of sensor 17 recorded on the 11th of October at 5 and 6 AM.

4.3.3. Analyse Different Sensors

In the next analysis, the responses to one passage recorded with different sensors are analysed. An example of multiple recording of the same passage is shown in Figure 4.12 (passage 3 as defined in Figure 4.9). The difference and similarities between the responses in both the longitudinal and the transverse direction were considered.

Longitudinal direction Sensors 14, 15, 17 and 18 were included in this analysis (Figure 4.12a-d). All these sensors were attached to the same bulb but in two different plate fields. Sensors 14 and 17 were located at midspan of the bulb and sensors 15 and 18 at a quarter of the length. Comparing the responses lead to the following observations.

Firstly, the shape of the the acceleration response in the time domain of the sensors is similar but the sensors at midspan have a higher peak acceleration. Secondly, the frequency spectra show large similarities as well but two differences were noticed: the peak around 90 Hz slightly moves when comparing the sensors at midspan to the sensors at a quarter length and the spectra of sensors 14 and 15 show more peaks than the spectra of sensors 17 and 18 which were located on a different plate field. The same behaviour was observed when considering other passages.

Transverse direction Three sensors were included in this analysis: sensors 17, 21 and 29 (Figure 4.12c, e and f). These sensors were used to analyse the response of sensors located next to each other in transverse

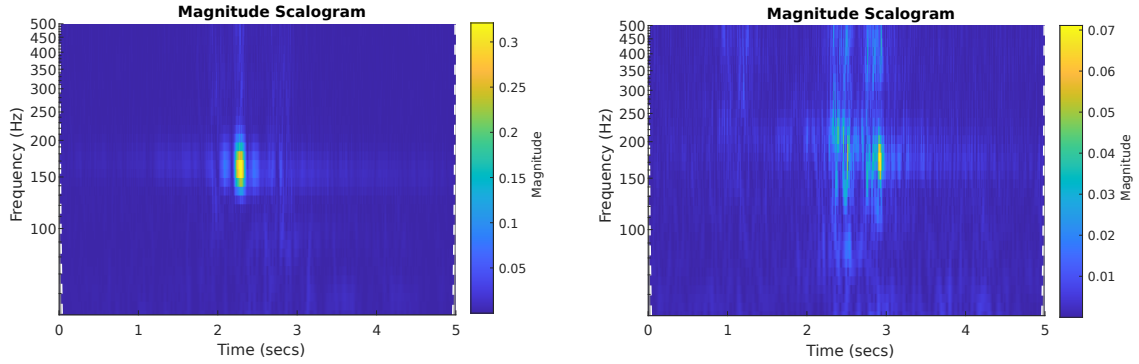

(a) Passage 1 (b) Passage 2

Figure 4.10: Scalogram of the wavelet transform of sensor 17 of two passages recorded on the 11th of October at 5 AM.

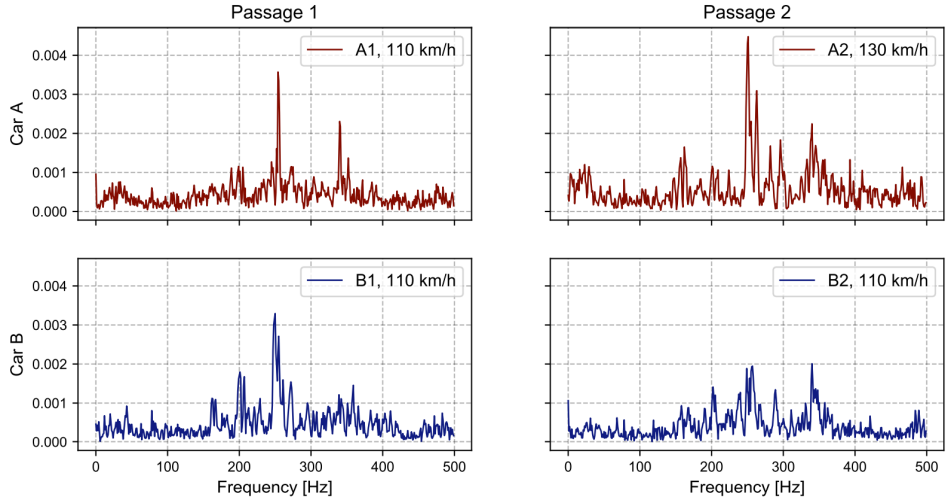

Figure 4.11: The frequency response spectra of the car experiment as conducted and plotted by Greijmans (2020).

direction. This way, the influence of the eccentricity of the load relative to the sensors was investigated which is important since the exact location and path of the vehicles during the measurements were unknown.

Figure 4.12 shows that the responses of the three sensors to the same vehicle passage are similar in shape. However, the amplitude of both the acceleration and frequency response does vary. It is expected that the closer the wheel is located above the sensor, the larger its response amplitudes are. In addition, the spectrum of sensor 29 has no significant peaks around 10 and 30 Hz in contrary to the other sensors. This could be caused by the location of the sensor close to the wall of the box girder.

4.3.4. Conclusion

The most import conclusion of the sample analyses is that different vehicle passages generate different responses in both the acceleration and frequency domain (Figure 4.9). The high-frequency components are most sensitive to changes. The car experiment in Figure 4.11 showed that the spectrum even changed with passages by the same vehicle. On the other hand, the responses measured by sensors aligned longitudinally as well as transversely were very similar when considering the same passage (Figure 4.12). From the latter figure, it became clear that the changes in response are not caused by the position of the vehicle relative to the sensor; this only influenced the amplitude of the response.

The question was raised what caused the large differences in response between passages. Answers to this question are looked for in Chapter 6, Chapter 7 and Chapter 8. In the former chapter, the system of the Haringvlietbrug is investigated with the eigensystem realisation algorithm (ERA), while the latter chapters introduce a semi-analytical model of a simplified bridge structure to investigate its sensitivity to the parameters of the structure and the vehicles.

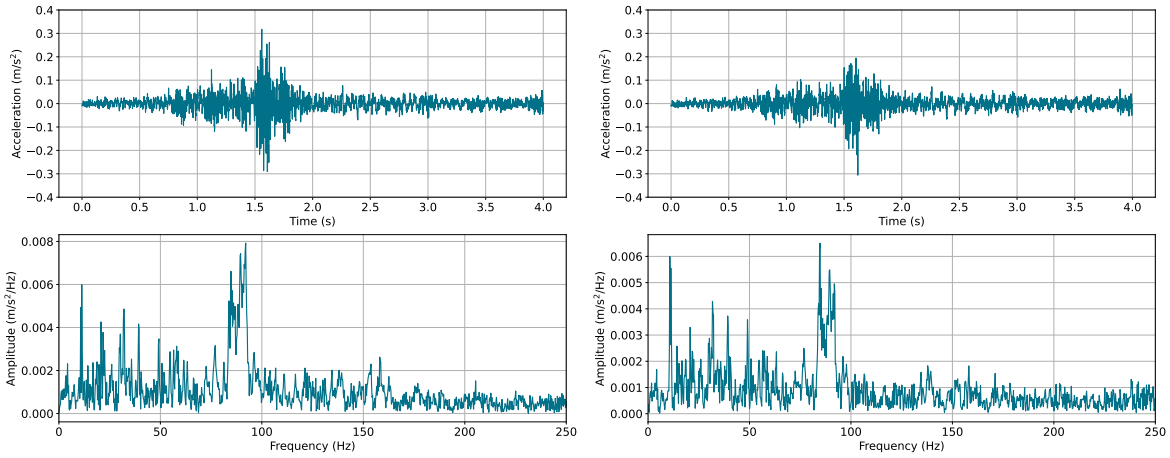

(a) Sensor 14

(b) Sensor 15

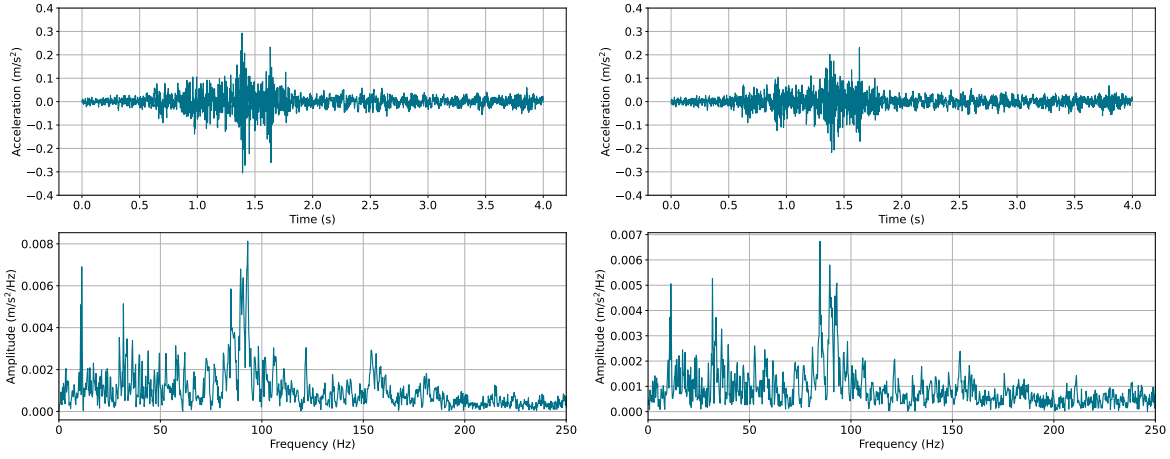

(c) Sensor 17

(d) Sensor 18

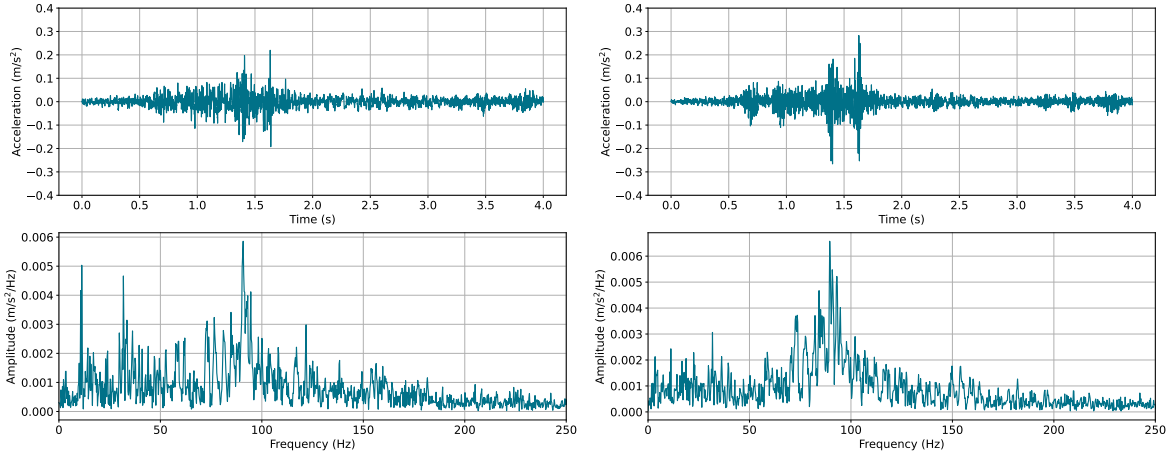

(e) Sensor 21

(f) Sensor 29

Figure 4.12: The acceleration and frequency response of passage 3 (see Figure 4.9) recorded on the 11th of October at 5 AM.

5

Similarity Filtering: Theory and Application

This chapter is about similarity filtering (SF), the first research question. In Section 5.1, the theoretical background of SF is explained, while Section 5.2 is about the application of SF on the acceleration data of the Haringvlietbrug and all the necessary steps. Then, the performance of SF is judged and discussed based on three assessment criteria in Section 5.3 and, lastly, the conclusion is given in Section 5.4.

5.1. Theory of Similarity Filtering

As already introduced in Chapter 1, this thesis investigated the effectiveness of similarity filtering (SF) in normalising the data with respect to traffic effects. SF also damps other short-term non-stationary effects (e.g. wind-induced variation effects). SF was firstly introduced by Milosevic (2018) and later adapted by De Bruijn (2019). The main idea of SF is that by convolution similarities between different samples of the same sensor are amplified and differences are damped. This way, only the stationary behaviour of the structure - vibrations in the eigenmodes - remains in the signal. This can only be the case if the system is time-invariant, a key assumption of SF.

SF is based on the convolution theorem. Convolution is a mathematical operation to obtain the response $x(t)$ of a system $h(t)$ subjected to a force $f(t)$. Convolution between two functions is denoted with an asterisk:

$$x(t) = h(t) * f(t) = \int_{-\infty}^{\infty} h(\tau) f(t-\tau) d\tau \tag{5.1}$$

According to the convolution theorem, convolution in the time domain is equal to multiplication in the frequency domain:

$$X(\omega) = H(\omega) F(\omega) \tag{5.2}$$

This property of convolution illustrates the idea behind SF. When applying SF on two signals, all frequencies are multiplied with each other which amplifies frequencies existing in both samples.

The system is assumed to be linear time-invariant (LTI) when all samples used for the similarity filter are measured during similar environmental conditions. This way, only operational variabilities are included in the samples, not environmental variabilities.

Before applying SF, all signals are split up into small samples which are subsequently convolved with each other. There are two filter coefficients: the length of the samples and the order of the similarity filter (the number of convolutions subjected to each signal). The optimal values of these coefficients depend on the case under study. The influence of both coefficients is discussed below.

When determining the length of the samples three aspects, are considered: the computational costs of the operation, the time scale on which SF operates and the expected natural frequencies of the system (De Bruijn, 2019). Longer samples require more data than short samples, thereby increasing the computational costs of applying SF. The time scale is important because the system cannot be considered time-invariant if the samples are too long. Lastly, the expected natural frequencies play a role when determining the sample size. All time samples must be able to capture the full dynamical behaviour of the structure. A sufficient number of cycles of the lowest frequency of interest must be included in each sample.

Determining the order of SF is done in combination with choosing the sample length. A higher order is computationally more expensive and requires the availability of a more extensive data set since data is lost by convolving. After applying SF, a too low order would result in a still unusable data set and a too high order would result in loss of data, possibly causing modes to be unidentified.

The eventual goal of SF is to be able to extract damage-sensitive features from the signals. The input acceleration signals contain practically all frequencies and are therefore wide-band processes. After SF, the signals are expected to be narrow-band processes. In the frequency domain, this yields peaks that would serve as features to detect damage. These features are still influenced by environmental variabilities; these can be removed at a later stage.

5.2. Application of Similarity Filtering

Similarity filtering (SF) was applied on the data set of the Haringvlietbrug to investigate its effectiveness in removing operational variabilities from the signals. All the steps taken and the choices made are shown below. First some pre-processing steps were needed. Then, the SF coefficients as introduced in the previous section (the sample length and the order of SF) are determined. Lastly, the extraction of features is discussed.

Only the 19 accelerometers positioned in the z-direction on the bulbs were included in this analysis. As a concentration of consistent modes were found at 95 Hz in the preliminary modal analysis in Section 4.1, a band-pass filter was applied to only take a frequency range of 75 to 110 Hz into account. By narrowing the frequency range, it was expected that the similarity filter resulted in a frequency spectrum with a single peak.

5.2.1. Pre-Processing Steps

Before SF can successfully be applied to the data set, two pre-processing steps need to be taken. Firstly, the spikes found in the frequency domain of the acceleration data (Section 4.1) were filtered out. After this, the acceleration data was split up into small samples by the method which was explained in Section 4.3. The optimal length of these samples is determined in the next section.

The spikes in the signals needed to be removed since SF converged to the spikes instead of to physical time-variant frequency components because the spikes have a relatively large magnitude and a constant frequency. The spikes were eliminated with the following steps and for each sensor separately:

1. The frequency domain of the spike within a range of 20 Hz was determined.
2. The data was filtered with a high-pass Butterworth filter of 20 Hz to remove the high-power low frequencies. Then, a Fourier transform (FT) was performed on the signals.
3. In the frequency spectrum, the highest peak in the found frequency domain of the spike was selected by a peak-finding algorithm. The spikes above 300 Hz were ignored as this frequency was outside the domain of interest.
4. The frequency of the found peak and twice this frequency (see Section 4.1 for an explanation) were used as input parameters to design a notch filter with a quality factor of 100. Subsequently, the raw signal was filtered with the designed notch filter.
5. Steps 1 to 4 were repeated for all sensors.

Figure 5.1 shows the frequency spectrum of the same signals as in Figure 4.2 but after removing the spikes. This method has a drawback: by removing the spikes from the signals, valuable data could be lost because the notch filter not only removes the spike itself but also other frequency components close to the spike. To limit the influence of this effect on the results of similarity filtering, it was chosen to only include the sensors without spikes in the frequency domain between 75 and 110 Hz (sensor 9, 11, 12, 14, 15, 17, 22, 23, 24, 25, 27 and 29).

5.2.2. Similarity Filter Coefficients

After obtaining the pre-processed samples, the filter coefficients of the SF were selected. The right coefficients were determined in view of the smoothness of the spectrum and the computational costs. There are two filter coefficients: the order of SF and the length of the samples. Both coefficients were determined by visual inspection of the frequency spectra after applying SF. One should note that the choice of filter coefficients seems arbitrary in this data set; other combinations of coefficients did not necessarily yield worse results.

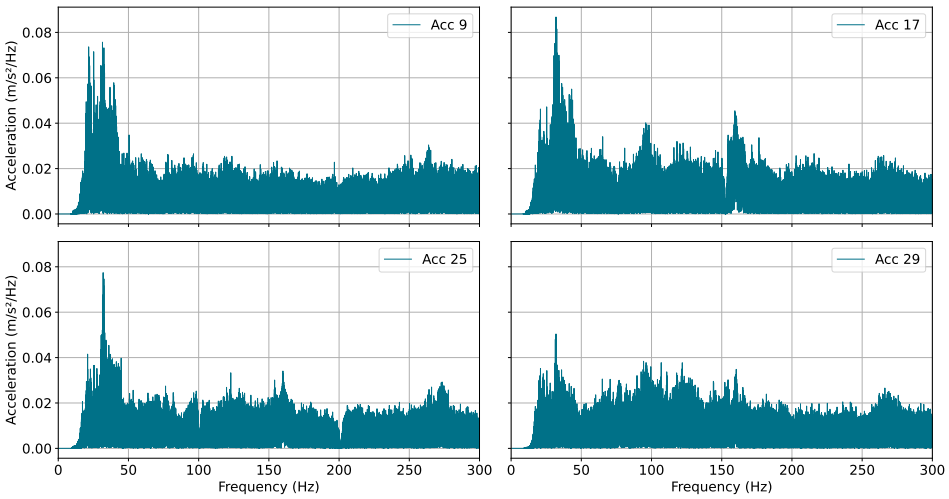

Figure 5.1: Fourier transform of sensors 9, 17, 25, 29 recorded on the 11th of October at 5 AM after removal of the spikes with a high-pass filter of 20 Hz.

Order of the similarity filter The most suitable order of similarity filtering was obtained by inspecting waterfall plots. In these plots, the same signal with different orders of SF was compared. Figure 5.2a shows an example of such a plot. Comparing multiple different signals made clear that an order higher than 30 does not smoothen the output spectrum significantly more while increasing the computational costs. On the other hand, the spectrum is still rough after SF with an order below 10.

Another consideration was the availability of a sufficient amount of samples while taking the LTI assumption and sample selection criteria into account. Since the system must be time-invariant, SF can only be applied on samples within one 15-minute measurement. However, the sample selection criteria caused only limited availability of samples. It was found that a SF order higher than 30 would cause a large part of the 15-minute measurements had to be neglected because too few suitable samples were available. In short, the most suitable order of the similarity filter was between 10 and 30.

Sample length Figure 5.2b shows the waterfall plot of the spectrum of a signal after SF is performed with different sample lengths. From the figure it becomes clear that the sample length does not influence the smoothness of the spectrum in a consistent manner: a sample length of 2 and 6 seconds resulted in a smoother spectrum than a sample length of 5 seconds. Inspecting also other signals indicated a random process.

Three other criteria also played a role concerning the sample length. Firstly, the sample length highly affects the computational costs of the similarity filter. Samples longer than 5 seconds were not desired because of this. In addition, the availability of suitable samples decreases with increasing sample lengths because of the sample selection criteria. Secondly, a sample must not be too long because in that case the vibrations caused by the vehicle are already damped out leaving only ambient vibrations. The bridge deck vibrated approximately 3 seconds after most passages according to the acceleration data. Lastly, samples shorter than 1 second were not desired because then the resolution of the frequency spectrum of the samples is low which leads to increased uncertainties. In short, the most suitable sample length was between 1 and 3 seconds.

5.2.3. Feature Extraction

The last step of similarity filtering (SF) is the extraction of the features for damage detection. Based on the results of De Bruijn (2019), it was expected that SF would converge the signals into narrow-band processes leaving one single frequency to be extracted. However, the resulting spectra mostly contained multiple distinctive frequencies and noise (as already visible in Figure 5.2). This increased the uncertainty of the extracted features. For damage detection, it is important to select peaks corresponding to the same modes. This yielded the question of which peak had to be selected as a feature. Three possibilities were implemented: select the highest peak, select all peaks above a certain threshold and select the most likely peak.

The latter implementation needs more explanation. For each signal, all peaks above a certain threshold value were selected. If only one peak was selected, this peak was extracted as a feature. If two or more peaks

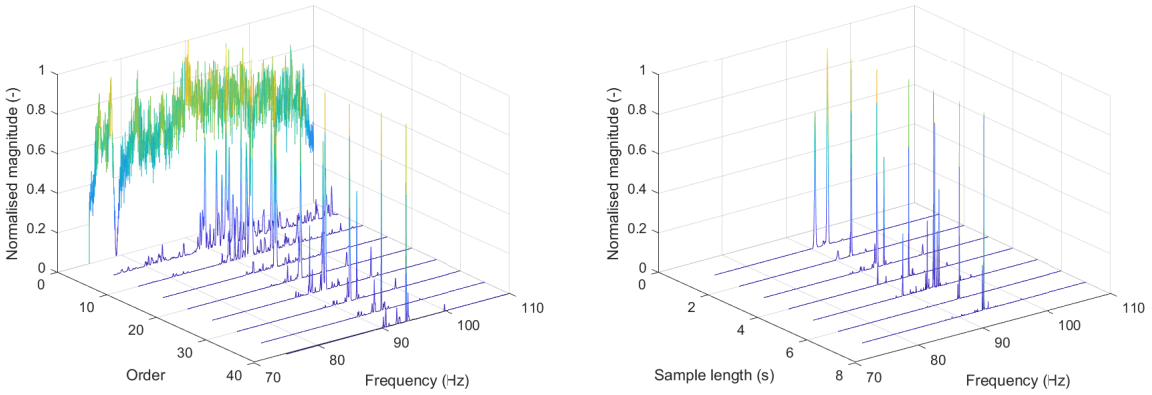

(a) Varying orders (segment length = 3 s)

(b) Varying sample lengths (order = 30)

Figure 5.2: Waterfall plots of the frequency spectrum of the output of SF with varying filter coefficients of sensor 17 recorded on the 8th of October at 3 PM.

were selected, the peak closest to the median of the peaks of the adjacent measurements was extracted as a feature. This peak was seen as the most likely peak because the system is assumed to be time-invariant; the adjacent measurements were recorded during highly similar conditions as a result of which the same modes need to have approximately the same frequency.

5.3. Results and Discussion

In this section, the results of similarity filtering (SF) are shown and discussed. The previous section showed a variety of choices of coefficients and implementations. For the sake of clarity, only one combination of factors is discussed in this section. The displayed combination yielded the best results. The results below were obtained with an order of SF of 30 and a sample length of 3 seconds and the most likely peaks were extracted as features. Furthermore, all signals with an insufficient amount of samples to comply with all criteria were disregarded. Lastly, only the results of four sensors and a frequency range from 75 to 110 Hz are shown in the following. The similarity filter is, however, applied on all suitable sensors and also on a frequency range of 45 to 75 Hz. The results were similar in all cases.

The performance of SF was judged based on three assessment criteria: the smoothness and consistency of the spectra after SF, the consistency of the features within batches of measurements and the correlation between the features and the temperature. Below, the results of SF are presented and discussed based on these criteria.

Smoothness and consistency of the spectra The aim of the similarity filter was to obtain a smooth spectrum converged to a single peak which would be subsequently extracted as a feature. This was not the case. Figure 5.2 shows an example of the frequency spectrum of a signal after the application of SF at the Haringvlietbrug. Three characteristics of the plots stand out. Firstly, many of the observed spectra still contain multiple peaks and noise after the application of SF. Secondly, the frequency of the peaks is not always consistent within one signal; they are sensitive to changing filter coefficients. As visible in Figure 5.2, the peaks of the same signal can shift about 1 Hz with varying filter coefficients. Thirdly, the magnitude of the extracted peaks show large variations: it ranges from 10^{10} to 10^{-27}.

The resulting spectra after SF did not match the expectations The spectra often contained multiple peaks and noise which increased the uncertainty of extracted features. This uncertainty was further increased by the fact that extracted features depended on the filter coefficients. The filter coefficient should not influence the physical properties of the structure. Apparently, the features do not only represent physical properties. Also the large variation of magnitudes of the peaks illustrates the uncertainties in the methodology.

Consistency of the features within batches One would expect that the features of measurements taken during highly similar environmental conditions are much alike. Figure 5.3 displays the extracted features

of four sensors of a nightly batch of seven 15-minute measurements. All measurements in this batch were taken during highly similar environmental conditions as explained in Section 3.3. From the figure, it is clear the consistency of the features is different for each sensor. The extracted features from sensors 17 and 29 show relatively good consistency with a variance of maximal 1 Hz between measurements. On the contrary, the results of sensor 9 are scattered and the results of sensor 25 contain two outliers. Of all twelve considered sensors, only three showed good batch consistency. The lack of consistency in the results is likely to be caused by the rough and inconsistent spectra as explained in the previous paragraph.

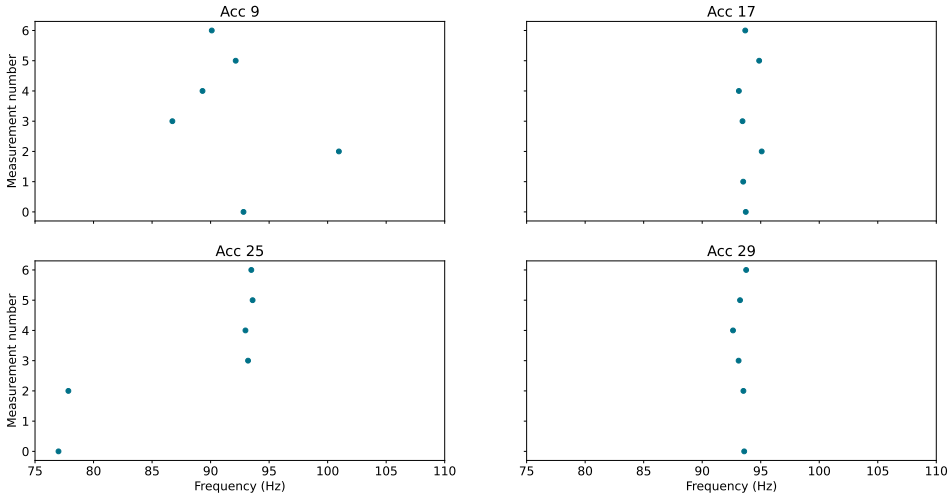

Figure 5.3: The extracted features of a batch of measurements recorded on the 14th of October from 2 to 8 AM.

Correlation between the features and temperature Based on literature, it was expected that the extracted features would show a strong correlation with the temperature. The found correlations between the features and the temperature at the bottom of the asphalt layer (this temperature sensor (sensor 12) yielded the best results) are shown in Figure 5.4. In the figure, the coefficient of determination (R^2) is used as a measure of correlation. A value of 0 indicates no correlation and a value of 1 indicates perfect correlation. Only measurements taken during dry weather and without direct sunlight were included in this analysis. The correlation is different for all sensors. Only sensor 17 shows a clear positive correlation (but still with a low R^2 value). The other sensors show no or a weak positive or negative correlation. The correlations changed significantly with changing filter coefficients. In short, the resulting correlations were not sufficient to normalise the features with respect to temperature.

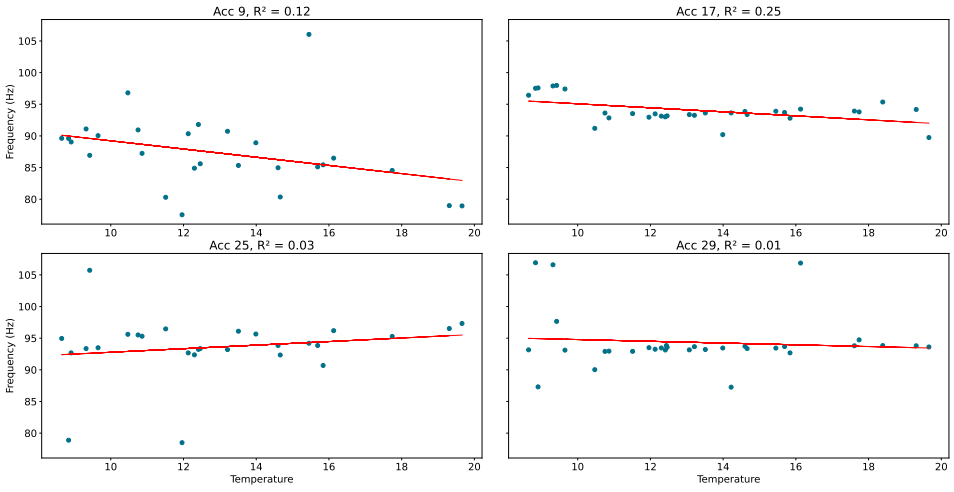

Figure 5.4: The correlation between the asphalt temperature and the extracted features of measurements recorded during moments without rain and direct sunlight from the 8th to the 18th of October.

The results of this research did not match the expectations nor the results of Milosevic (2018) and De Bruijn (2019). Unlike this research, they did get converged narrow-band processes and smooth spectra after applying SF. It was found, however, that they applied SF on malicious data. The same spikes as present in the data set of the Haringvlietbrug were also already present in the data set of the Zwartewaterbrug although smaller in magnitude. This caused SF to converge to the spikes instead of to vibrations in the eigenmodes of the structure. So, the extracted features did not contain structural characteristics. Nevertheless, good correlations between the features and the added mass (damage) were found in De Bruijn (2019) but the author concluded that these correlations were most likely caused by environmental variabilities instead of a changing added mass. With hindsight, these results of De Bruijn (2019) confirmed the observation of Greijmans (2020) that the spikes in the data show a strong positive correlation with the temperature. In this research, the spikes were removed before applying SF.

Three potential reasons why SF does not perform as expected were identified and listed below. The first reason is the high sensitivity of the proposed method to separate input samples and filter coefficients. A single deviating sample significantly influenced the total results which makes the large variance between the results possible. Also one single poor sample effected the final results. The high sensitivity is likely to be caused by the sequence of convolutions each signal is subject to. To illustrate this, if a certain frequency component is dominant during a measurement but in one sample it is only marginally present, this single sample will drastically decrease the magnitude of this frequency component in the results of the similarity filter. This is caused by the core of SF; multiplications of the frequency spectra.

Secondly, one can expect that many closely-spaced modes are present in the high-frequency domain of the structure. The aim of SF was to get a smooth spectrum with only one resonance peak. It is likely that other modes are then disregarded. If different measurements converge to another mode, it is impossible to compare them.

Lastly, it is possible that the dynamic response of the bridge deck is different for each passage. It was expected that the steady-state response of the bridge to the passages of different vehicles was approximately the same. However, the data suggested this to not be the case. This could be because the presence of certain frequency components might be influenced by the mass loading effect or that the influence of vehicle characteristics on the vibrations of the bridge deck was larger than expected. The impact of this effect was tried to limit by sample selection but it is either possible that vehicles were still (partly) present on the bridge segment or that vehicles located on different parts of the bridge influence the dynamic response causing a shift in natural frequencies. This shift would then be different for each passing vehicle which would harm the assumption that the system is time-invariant causing the method of SF to be non-applicable.

5.4. Conclusion

Similarity filtering did not score well on all three assessment criteria. The resulting frequency spectra were noisy and the location and magnitudes of the peaks were inconsistent which increased the uncertainty of extracted features. Furthermore, the results of SF appeared to be sensitive to the filter coefficients. The high uncertainty and randomness of the features are clearly visible in Figure 5.3 and Figure 5.4, in which outliers and no or low correlation between the features and the temperature can be found.

The first research question of this research was *To what extent is similarity filtering an effective method to remove operational variabilities from the signals at the Haringvlietbrug?*. The answer to this question is that SF is not an effective method to remove operational variabilities from the signal when applying it to data acquired with accelerometers attached to the bridge deck of the Haringvlietbrug and above 50 Hz. In this area of application, the method is not robust, causing the results to be inconsistent and dependent on the filter coefficients. Therefore, it is not possible to extract suitable features for damage detection.

Three reasons were identified for this inconsistency of the features: the influence of every single sample on the results, ignoring closely spaced modes and a changing dynamic bridge response for each passage. The latter reason will be further investigated in the next chapters.

6

Eigensystem Realisation Algorithm: Theory and Application

The eigensystem realisation algorithm (ERA) was applied on the Haringvlietbrug data set to investigate the influence of different vehicle passages on the dynamic response of the bridge deck. With ERA, it was tried to identify consistent mode shapes and compare these in order to see why similarity filtering (SF) did not work as expected. Section 6.1 provides the theoretical background of ERA and in Section 6.2, ERA is applied on the Haringvlietbrug data. Next, the results are presented and discussed in Section 6.3 and the conclusion are given in Section 6.4.

6.1. Theory of the Eigensystem Realisation Algorithm

ERA is an operational modal analysis (OMA) and output-only system identification technique firstly proposed by Juang & Pappa (1985). ERA has two key assumptions: the system needs to be linear time-invariant (LTI) and excited by an impulse force. The derivation of the method below is based on Brunton (2018) and Gasparis (2019).

An LTI system is described by the state-space equations of Equation 6.1 wherein the first equation is called the discrete-time state equation and the second equation is called the observation equation.

$$\begin{cases} \mathbf{x}_{k+1} = \mathbf{A}\mathbf{x}_k + \mathbf{B}\mathbf{u}_k \\ \mathbf{y}_k = \mathbf{C}\mathbf{x}_k + \mathbf{D}\mathbf{u}_k \end{cases} \tag{6.1}$$

where $\mathbf{x} \in \mathbb{R}^{n\times 1}$ is the state vector, $\mathbf{u} \in \mathbb{R}^{r\times 1}$ is the system input (force) vector $\mathbf{y} \in \mathbb{R}^{m\times 1}$ is the system output (measurement) vector, $\mathbf{A} \in \mathbb{R}^{n\times n}$, $\mathbf{B} \in \mathbb{R}^{n\times r}$, $\mathbf{C} \in \mathbb{R}^{m\times n}$ and $\mathbf{D} \in \mathbb{R}^{m\times r}$ are the state-space matrices, k is the time step, n is the order of the system, r is the amount of loaded nodes and m is the amount of sensors. Because of the impulse response assumption and the assumption of zero initial conditions, the following variables are known: $\mathbf{u}_0 = \mathbf{I}$ and $\mathbf{u}_k = \mathbf{x}_0 = 0$ if $k > 0$. By iterating the state-space equations over time, one obtains the Markov parameters as shown in Table 6.1.

Table 6.1: Markov parameters.

	$\mathbf{u}$	$\mathbf{x}$	$\mathbf{y}$
$k=0$	$\mathbf{I}$	0	0
$k=1$	0	$\mathbf{B}$	$\mathbf{CB}$
$k=2$	0	$\mathbf{AB}$	$\mathbf{CAB}$
$\vdots$	$\vdots$	$\vdots$	$\vdots$
k	0	$\mathbf{A}^{k-1}\mathbf{B}$	$\mathbf{CA}^{k-1}\mathbf{B}$

With the Markov parameters, two Hankel matrices are formed with the measurements. The regular Hankel matrix $\mathbf{H}_0 \in \mathbb{R}^{p\times q}$ is shown in Equation 6.2. The Hankel matrix is equal to the multiplication of the observability vector $\mathscr{O}$ with the controllability vector $\mathscr{C}$. Equation 6.3 shows the shifted Hankel matrix $\mathbf{H}_1 \in \mathbb{R}^{p\times q}$ which is shifted over one time step compared to $\mathbf{H}_0$.

$$\mathbf{H}_0 = \begin{bmatrix} y_1 & y_2 & \cdots & y_q \\ y_2 & y_3 & \cdots & y_{q+1} \\ \vdots & \vdots & \ddots & \\ y_p & y_{p+1} & & y_{p+q-1} \end{bmatrix} = \begin{bmatrix} \mathbf{CB} & \mathbf{CAB} & \dots & \mathbf{CA}^{q-1}\mathbf{B} \\ \mathbf{CAB} & \mathbf{CA}^2\mathbf{B} & \dots & \mathbf{CA}^{q}\mathbf{B} \\ \vdots & \vdots & \ddots & \\ \mathbf{CA}^{p-1}\mathbf{B} & \mathbf{CA}^{p}\mathbf{B} & & \mathbf{CA}^{p+q-1}\mathbf{B} \end{bmatrix} = \mathscr{O}\mathscr{C} \tag{6.2}$$

$$\mathbf{H}_1 = \begin{bmatrix} y_2 & y_3 & \cdots & y_{q+1} \\ y_3 & y_4 & \cdots & y_{q+2} \\ \vdots & \vdots & \ddots & \\ y_{p+1} & y_{p+2} & & y_{p+q} \end{bmatrix} = \begin{bmatrix} \mathbf{CAB} & \mathbf{CA}^2\mathbf{B} & \dots & \mathbf{CA}^{q}\mathbf{B} \\ \mathbf{CA}^2\mathbf{B} & \mathbf{CA}^3\mathbf{B} & \dots & \mathbf{CA}^{q+1}\mathbf{B} \\ \vdots & \vdots & \ddots & \\ \mathbf{CA}^{p}\mathbf{B} & \mathbf{CA}^{p+1}\mathbf{B} & & \mathbf{CA}^{p+q-2}\mathbf{B} \end{bmatrix} = \mathscr{O}\mathbf{A}\mathscr{C} \tag{6.3}$$

where p is the number number of rows and q is the number of columns of the Hankel matrices. These two parameters together with the order of ERA are the three parameters that have to be chosen by the user. ERA is a reduced-order method; the chosen order defines the rank of the state-space matrices. In the next step, the regular Hankel matrix is factorised using singular value decomposition (SVD) which results in the expression of Equation 6.4. In the second part of this equation, the non-dominant singular values are truncated for the model reduction.

$$\mathbf{H}_0 = \mathbf{U}\mathbf{\Gamma}^2\mathbf{V}^T = \begin{bmatrix} \widetilde{\mathbf{U}} & \mathbf{U}_t \end{bmatrix} \begin{bmatrix} \widetilde{\mathbf{\Gamma}}^2 & 0 \\ 0 & \mathbf{\Gamma}_t^2 \end{bmatrix} \begin{bmatrix} \widetilde{\mathbf{V}}^T \\ \mathbf{V}_t^T \end{bmatrix} \tag{6.4}$$

where $\mathbf{U}$ is the matrix of the left-singular vectors, $\mathbf{V}$ is the matrix of the right-singular vectors, $\mathbf{\Gamma}$ is the singular value matrix and t denotes the truncated values. With this information, the state-space matrices can be obtained. Since all modal properties of the system can be obtained from the reduced system matrix $\widetilde{\mathbf{A}}$ by solving the eigenvalue problem, only this matrix was derived:

$$\widetilde{\mathbf{A}} = \widetilde{\mathbf{\Gamma}}^{-1}\widetilde{\mathbf{U}}^T\mathbf{H}_1\widetilde{\mathbf{V}}\widetilde{\mathbf{\Gamma}}^{-1} \tag{6.5}$$

6.2. Application of the Eigensystem Realisation Algorithm

ERA was applied to the data set of the Haringvlietbrug by an existing Matlab script written by Al-Rumaithi (2022). This script has the following input parameters: the pre-processed sensor data, the ERA parameters (model order and dimensions of the Hankel matrices) and the sampling frequency (f_s = 1000 Hz). For the remaining input parameters, the default values were used. Besides the pre-processing steps and determination of the ERA parameters, also the post-processing steps are explained below.

6.2.1. Pre-Processing Steps

This research focused on higher-order modes; a frequency domain of 50 to 250 Hz was chosen as domain of interest. Therefore, a band-pass filter that passed frequencies between these values was applied to the data. The spikes in the frequency domain (Section 4.1) did not influence the results of ERA as they were recognised as fictitious modes. Before being able to apply ERA, the right data needed to be selected. This comprised two decisions: sensor selection and sample selection. With the sensor selection, it was chosen to bundle all the sensors in z-direction underneath the right driving lane and within one bridge segment. The analyses were performed with sensors 16, 17, 18, 19, 21, 25, 26, 27 and 29 as shown in Figure 3.6.

To fulfil the ERA assumptions (impulse response and LTI system) as good as possible, it was important to select the right samples. A sample starts right after the vehicle has left the bridge segment and stops after the vibrations have damped out. The samples were selected by the method explained in Section 4.3. Because the bridge deck vibrates mostly more than 2 seconds after the vehicle passage, the sample length was set to be 2 seconds which was also expected to be sufficiently long to include enough cycles of high-frequency modes.

6.2.2. ERA Parameters

As already introduced, three parameters were to be determined: the order and the dimensions of the Hankel matrices. Caicedo (2011) has published guidelines to make an educated first guess of what values to choose. The right values are different for all data sets and need to be determined based on the results. The choice of parameters is elaborated one-by-one below.

Model order Fictitious (numerical) modes of vibration occur if the model order is too high. A higher order also increases the computational costs of ERA. A too low model causes physical modes to be unidentified. A suitable model order was determined using stability diagrams. A physical mode should always be identified regardless of the model order (as long as it is not too low) which is visible in a stability diagram as shown in Figure 6.1. ERAs with different model orders were performed on the data set; for each order the identified modes are shown in the diagram. The left diagram shows the unfiltered identified modes. This diagram was filtered based on three criteria which resulted in the right diagram which most likely only contains physical modes. The three criteria were a modal assurance criterion (MAC) value of more than 0.95 (see Equation 2.5), an absolute frequency difference of the same modes in adjacent model orders of less than 0.05 Hz and a mode should have been identified in more than 20 different cycles. This resulted in the identification of three stable modes.

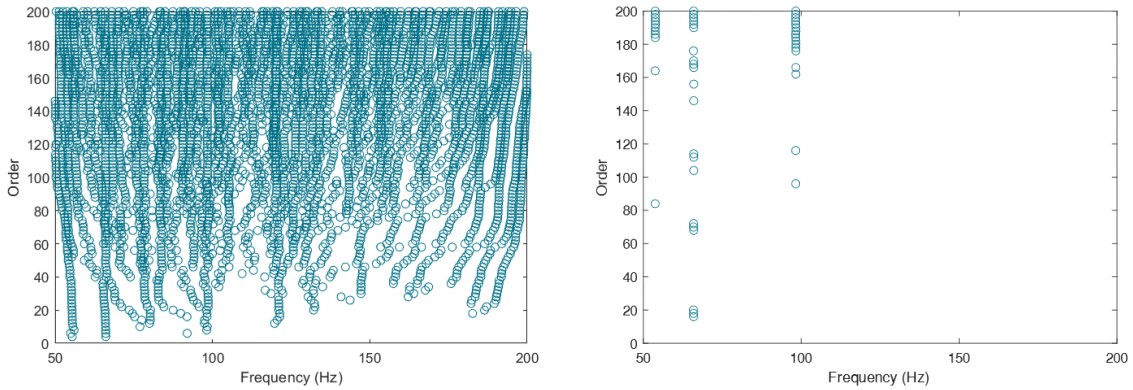

(a) Unfiltered (b) Filtered

Figure 6.1: Stability diagrams of a single vehicle passage after applying ERA.

Dimensions of the Hankel matrices Generally, the first estimation of the dimensions of the Hankel matrices is chosen based on the number of expected modes. A Hankel matrix with too few columns could lead to not identifying physical modes. A rule of thumb is to use four times the number of expected modes. When determining the number of rows of the Hankel matrix, one should choose the amount in such a way that most data is used but without including noisy data. Selecting noisy data was already prevented by sample selection. Therefore, the number of rows is equal to the number of data points (2000) minus the number of columns.

The number of expected modes can often be estimated by counting the peaks of a cross-spectral density (CSD) function as plotted in Figure 6.2 (Caicedo, 2011). In this dataset, however, almost no clear peaks were visible. Therefore, it was chosen to apply the default option: square Hankel matrices. So, $p = q = 1000$.

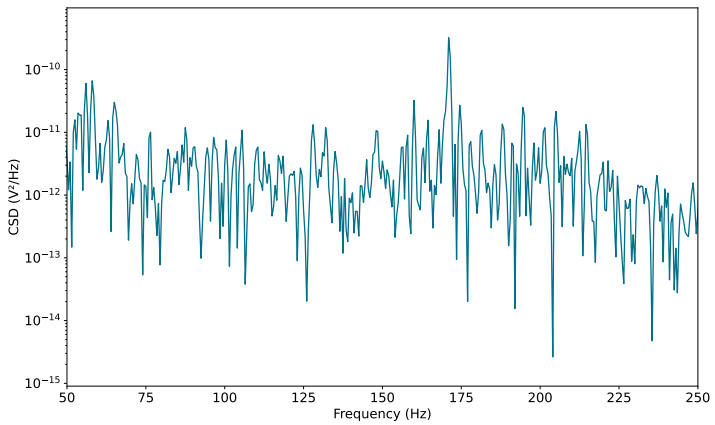

Figure 6.2: CSD of a sample of sensors 17 and 26 during the same passage.

6.2.3. Post-Processing Steps

With the determination of all input parameters of the script, ERA can be performed. The results need two post-processing steps. Firstly, the fictitious modes were separated from the physical modes and consistent modes in different passages were looked for.

Stable-modes selection Selecting the stable, physical modes from all resulting modes is crucial to compare the vehicle passages. A stability diagram is a reliable but computationally expensive way to do this (Caicedo, 2011). A more computationally efficient way to separate physical from numerical modes is the consistent-mode indicator (CMI) as proposed in Pappa *et al.* (1992). The CMI rates the spatial and temporal consistency of a mode. A CMI value higher than 80 indicates high confidence modes, while modes with a value lower than 20 are likely to be fictitious. Stable-mode selection by CMI performed well on this data set: modes marked as stable using the stability diagram also had high CMI scores (most of the time more than 40). Therefore, it was chosen to indicate modes as stable if they had a CMI value above 40 instead of using the stability diagrams. Choosing a higher CMI value would increase the chance of missing physical modes.

Mode matching To test the effectiveness of ERA, it was applied on all suitable samples of passages within a batch of measurements as defined in Section 3.3. A total of 43 suitable samples were selected in the batch recorded on the 14th of October from 2 to 8 AM. It was a nightly batch in order to minimise the presence of traffic on other parts of the bridge. Stable modes found during different vehicle passages were automatically matched by the algorithm based on two criteria: they should have a MAC value higher than 0.9 and an eigenfrequency difference less than 10%.

6.3. Results and Discussion

Performing the above steps on the Haringvlietbrug data, many different stable mode shapes were identified. Two of them were found relatively consistently throughout all investigated vehicle passages. Mode shape 1 was found in 35 of the 43 passages and had eigenfrequencies ranging from 62 to 71 Hz. Mode shape 2 was found in 33 of the 43 passages with eigenfrequencies ranging from 89 to 102 Hz. Two examples of both consistent mode shapes are shown in Figure 6.3

The results of ERA approximately matched the results of the FDD in Chapter 4 but the matched modes still had a relatively large variance in both shape and eigenfrequency. This could be explained by some characteristics of ERA that might have increased the uncertainty of the results. This research identified five potential issues:

- Violation of the impulse response assumption. All frequencies of the response of the bridge should be excited with the same intensity (a white-noise spectrum). The scalograms of the continuous wavelet transform (WT) as shown in Figure 4.10 shows this is not the case. Although the response covered most frequencies, a dominant frequency component was present. The difference in magnitude between the dominant frequency components and the other frequency components increased for larger passage peak accelerations.

- Violation of the LTI assumption. The system appeared to be not perfectly time-invariant for two reasons: firstly, the dominant frequency component as visible in Figure 4.10 was also present a couple of seconds before and after the actual passage. Secondly, it is possible that vehicles located at another part of the bridge still influenced the local behaviour of the investigated segment. An indication that this happens is visible in Figure 4.8a. In this figure, the acceleration response shortly changed around 603 seconds. This would also violate the impulse response assumption.

- Insufficient spatial density of the sensors. It can be expected that many closely-spaced modes are present in the frequency range of interest. It is possible that those closely-spaced modes cannot or can hardly be separated from each other because of an insufficient spatial density of the sensors. This could be an explanation for the fact that sometimes multiple modes of the same passage were matched by the mode-matching algorithm.

- Poor choice of ERA parameters. The ERA parameters were difficult to determine because no clear peaks were visible in the CSD (Figure 6.2). So, it was not known how many physical modes can be expected between 50 and 250 Hz. The order, as well as the dimensions of the Hankel matrices, depended on this.

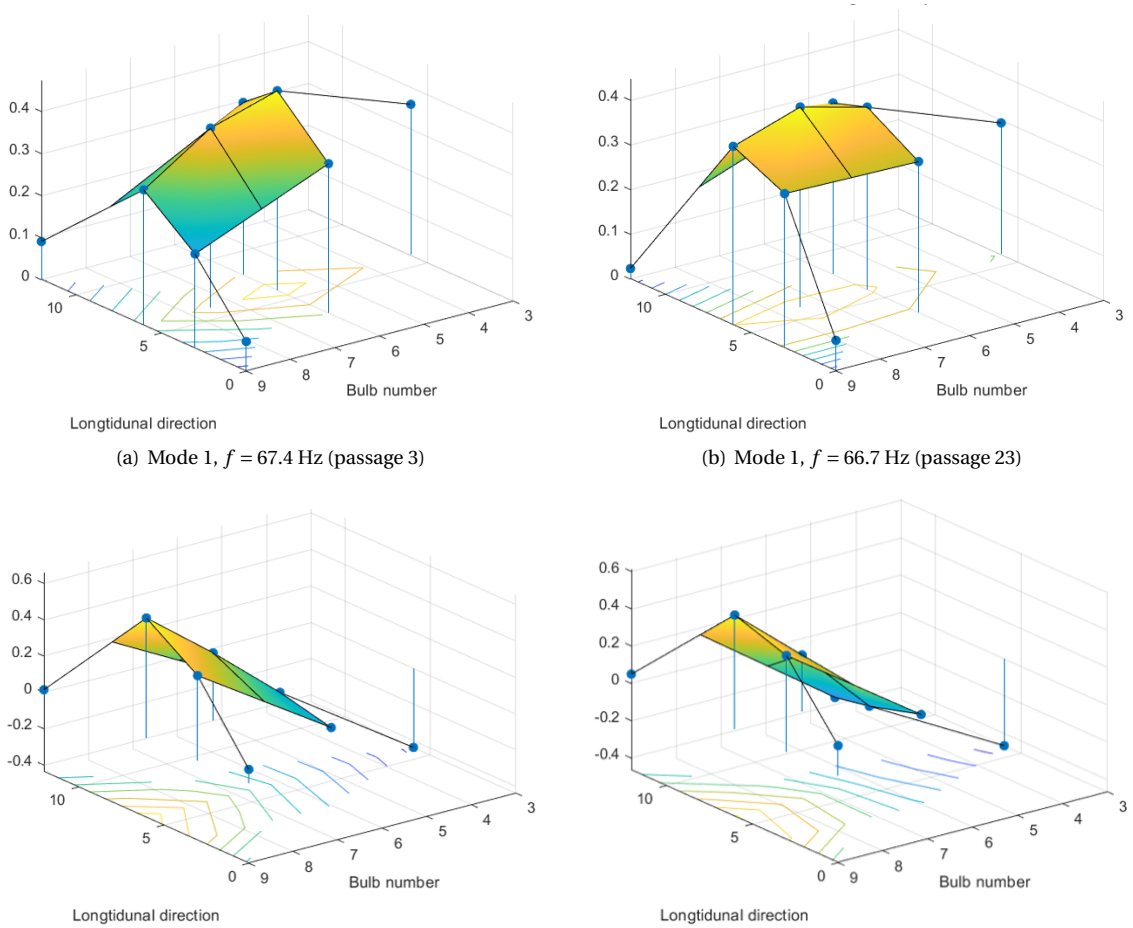

(a) Mode 1, $f = 67.4$ Hz (passage 3)

(b) Mode 1, $f = 66.7$ Hz (passage 23)

(c) Mode 2, $f = 98.9$ Hz (passage 26)

(d) Mode 2, $f = 89.3$ Hz (passage 32)

Figure 6.3: Two examples of consistent mode shapes. The bulb numbers are assigned in the sensor layout in Figure 3.6.

- Insufficient signal-to-noise ratio. In the case of vehicle passage with a relatively low peak acceleration (like the sample in Figure 4.8a), the magnitude of the free vibrations was only marginally larger than the noise. Noisy data increases the uncertainty of the results of ERA.

6.4. Conclusion

There are large uncertainties when investigating higher-order modes. Although some consistent modes were identified, the variance in mode shape and especially eigenfrequency between different passages was large. Five potential sources of the large uncertainties were identified. It is unknown what the most important source of uncertainty is. It is expected that this is related to the probably changing dynamic characteristics of the system during a vehicle passage. This would mainly harm the assumption that the system is time-invariant and was also one of the reasons similarity filtering (SF) did not produce usable damage-sensitive features. To get a better understanding of the dynamic properties of the bridge during vehicle passages, the vehicle-bridge interaction (VBI) is investigated in the next chapters.

7

Semi-Analytical Model of Bridge Vibrations

In this chapter, an analytical model is built to investigate the influence of changing parameters on the vibrations of the bridge deck as it was concluded in previous chapters that a large variety exists in dynamic bridge response to different vehicle passages. The goal of the model was to investigate the sensitivity of the response to different parameters. If this sensitivity is known and limited, it might be possible to reduce the dependency of the measurements on these parameters to make the data suitable for structural health monitoring (SHM). The model was solved numerically. A segment of the Haringvlietbrug was simplified to a simply supported beam on a viscous continuous support. The beam contains two local resonators to induce local modes and vehicles were modelled as moving mass-spring systems. The beam together with the moving load forms an interactive dynamical system. The equation of motion of an Euler-Bernoulli beam on a viscous continuous support is:

$$\frac{\partial^2}{\partial x^2}\left(EI\frac{\partial^2 w}{\partial x^2}\right)+\rho A\frac{\partial^2 w}{\partial t^2}+c_d\frac{\partial w}{\partial t}=q(t) \tag{7.1}$$

where $q(t)$ is an arbitrary distributed load. A description of the other parameters can be found in Table 7.1. Equation 7.1 can be simplified since the beam has a constant bending stiffness and no external distributed loading is applied:

$$EI\frac{\partial^4 w}{\partial x^4}+\rho A\frac{\partial^2 w}{\partial t^2}+c_d\frac{\partial w}{\partial t}=0 \tag{7.2}$$

The vehicle was modelled as a mass-spring system, described by the following equation of motion:

$$M\frac{\partial^2 w_v}{\partial t^2}+Kw_v=0 \tag{7.3}$$

Table 7.1: Description of all parameters of the standard analytical model.

Parameter	Description
EI	Beam bending stiffness (Nm^2)
c_d	Beam distributed damping (Ns/m^2)
L	Beam length (m)
ρA	Beam mass per unit length (kg/m)
$w(x,t)$	Deflection of the beam (m)
$w_v(t)$	Deflection of the vehicle (m)
g	Gravitational acceleration (m/s^2)
x	Spatial coordinate (m)
t	Time (s)
M	Vehicle mass (kg)
K	Vehicle spring stiffness (N/m)

Again, the description of the parameters can be found in Table 7.1. To reduce the amount of input parameters and to make the results of the model applicable more generally, the model was transformed into a dimensionless model. Several dimensionless parameters were introduced to do so: $x = \xi L$, $w = \bar{w}L$, $w_v = \bar{w}_v L$ and $t = \tau t_0$. An overview and description of the dimensionless parameters can be found in Table 7.2. The equation of motion of Equation 7.2 was rewritten into a dimensionless form with the following steps. First, the dimensionless parameters were substituted into the equation:

$$\frac{EI}{L^3}\frac{\partial^4 \bar{w}}{\partial \xi^4} + \frac{\rho AL}{t_0^2}\frac{\partial^2 \bar{w}}{\partial \tau^2} + \frac{c_d L}{t_0}\frac{\partial \bar{w}}{\partial \tau} = 0 \tag{7.4}$$

Both the terms of the kinetic and potential energy should have a coefficient of 1. This was accomplished by first dividing the equation by EI/L^3:

$$\frac{\partial^4 \bar{w}}{\partial \xi^4} + \frac{\rho AL}{t_0^2}\frac{L^3}{EI}\frac{\partial^2 \bar{w}}{\partial \tau^2} + \frac{c_d L}{t_0}\frac{L^3}{EI}\frac{\partial \bar{w}}{\partial \tau} = 0 \tag{7.5}$$

Then, t_0 was chosen such that also the coefficient of the term of the kinetic energy is equal to 1, leading to the following equation of motion:

$$\frac{\partial^4 \bar{w}}{\partial \xi^4} + \frac{\partial^2 \bar{w}}{\partial \tau^2} + \bar{c}\frac{\partial \bar{w}}{\partial \tau} = 0 \tag{7.6}$$

Hence, the following definitions for t_0 and $\bar{c}$ exist:

$$t_0 = \sqrt{\frac{\rho A}{EI}L^4} \quad , \quad \bar{c} = \frac{c_d L^4}{t_0 EI} \tag{7.7}$$

The vehicle was modelled as a mass-spring system whose equation of motion was given in Equation 7.3. This equation was rewritten into a dimensionless form on the same manner as the beam. One obtains:

$$\bar{M}\frac{\partial^2 \bar{w}_v}{\partial \tau^2} + \bar{K}\bar{w}_v = 0 \tag{7.8}$$

where

$$\bar{M} = \frac{M}{\rho AL} \quad , \quad \bar{K} = \frac{KL^3}{EI} \tag{7.9}$$

The definitions of $\bar{M}$ and $\bar{K}$ show that the characteristics of the vehicle are now expressed in terms of ratios between the vehicle and the beam.

In the following, two different versions of the model are presented. In Section 7.1, the total system of the beam and vehicle is presented to generate time-history data of the beam and the derivation of the eigenfrequency analysis of the beam is shown. In Section 7.2, the default values of the parameters are introduced and the performance of the model is analysed in Section 7.3. Then the model is studied parametrically in Section 7.4. After this, the case of the simultaneous presence of multiple moving masses is discussed in Section 7.5. Lastly, Section 7.6 gives some conclusions on the model.

7.1. Derivation of the Semi-Analytical Model

The analytical model presented in this thesis consists of multiple elements, some of them already introduced in the previous section. A drawing of the model is shown in Figure 7.1. The main element is a simply-supported Euler-Bernoulli beam described by Equation 7.6. The beam lies on a viscous continuous support with damping coefficient $\bar{c}$; the part of the beam in between the local resonators is not damped. These two local resonators are attached to the beam at ξ_1 and ξ_2. The local resonators are mass-spring systems of which the mass is attached to the beam rigidly. The goal of these resonators is to make local, high-frequency, beam vibrations dominant compared to the global modes. The midspan between the resonators is indicated with ξ_m in the drawing. A mass moves along the beam to simulate a passing vehicle with a dimensionless velocity α. To induce vibrations in beam and the vehicle, the contact between the spring of the moving mass and the

surface of the beam is described by the unevenness, denoted by $r(\xi)$, and is assumed to be a point contact. An overview of all dimensionless parameters can be found in Table 7.2. The system has zero initial conditions (Equation 7.10) and its boundary conditions are shown in Equation 7.11:

$$\begin{aligned} \bar{w}(\xi,0) &= \frac{\partial \bar{w}(\xi,0)}{\partial \tau} = 0 \\ \bar{w}_v(0) &= \frac{\partial \bar{w}_v(0)}{\partial \tau} = 0 \end{aligned} \tag{7.10}$$

$$\bar{w}(0,\tau) = \bar{w}(1,\tau) = \frac{\partial^2 \bar{w}(0,\tau)}{\partial \xi^2} = \frac{\partial^2 \bar{w}(1,\tau)}{\partial \xi^2} = 0 \tag{7.11}$$

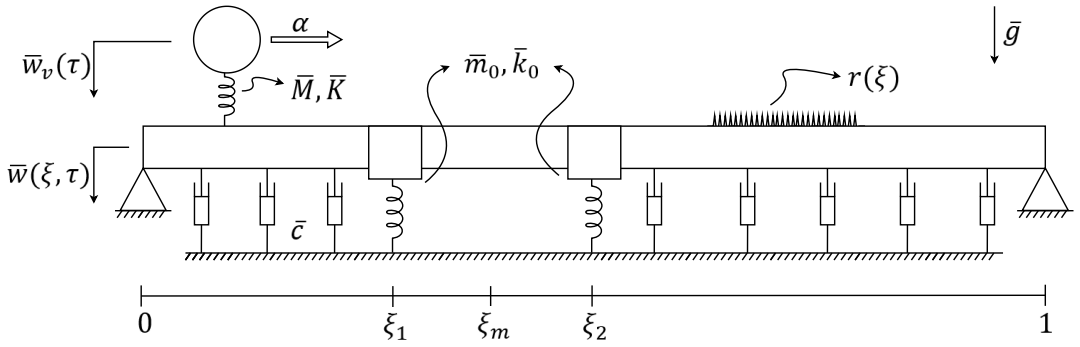

Figure 7.1: A drawing of the full analytical model.

Before the above explained model was proposed, a model with a beam containing only one local resonator was created. The elaboration of this model can be found in the Appendix Section A.3. It was chosen not to continue with the one-resonator model since it required an unrealistic high damping coefficient to induce local mode shapes. The model with two resonators enabled the option to have different damping coefficients: the damping coefficient between the resonators can take a realistic value (or be equal to 0), while the damping coefficient outside the resonators is allowed to be very high if that provides realistic wave propagation: waves should not reflect against the boundaries of the system. The damping coefficient outside the resonators are allowed to be unrealistic high because only the part of the beam in between the resonators is the actual model of the bridge deck. The parts of the beam outside the resonators have no physical relation to the bridge deck and are only meant for inducing vibrations in the resonators before the the moving mass is actually there.

The derivation of the model consists of two parts: the model is solved in the time domain for the time-history analysis of the system and in the spatial domain for the eigenfrequency analysis of the beam. The time-history analysis was desired because this data was also available for the Haringvlietbrug. This way, the effects of changing input parameters in the model could be compared to time-history recordings of the Haringvlietbrug. The eigenfrequency analysis, on the other hand, helped to improve the understanding of the model and to look for the modes of interest. Both approaches are explained below.

7.1.1. Derivation for the Time-History Analysis

A drawing of the model for the time-history analysis is shown in Figure 7.1. The model consists of a system of differential equations with equations for the beam and the vehicle. It was chosen to model the beam as one element which is the left-hand side of Equation 7.12 and already derivated in Equation 7.6. The spatially non-constant viscous damping was included by a Heaviside function. In the right-hand side of the equation, the local resonators and moving mass were included by Dirac delta functions. This led to the following dimensionless equation of motion:

$$\frac{\partial^4 \bar{w}}{\partial \xi^4} + \frac{\partial^2 \bar{w}}{\partial \tau^2} + \bar{c}_H \frac{\partial \bar{w}}{\partial \tau} = -(\delta(\xi-\xi_1)+\delta(\xi-\xi_2))\left(\bar{m}_0 \frac{\partial^2 \bar{w}}{\partial \tau^2} + \bar{k}_0 \bar{w}\right) - \delta(\xi-\alpha\tau)\left(\bar{K}(\bar{w}-\bar{w}_v-r(\xi)) - \bar{M}\bar{g}\right) \tag{7.12}$$

where

$$\bar{c}_H = \bar{c}(\mathrm{H}(\xi_1-\xi)+\mathrm{H}(\xi-\xi_2)) \tag{7.13}$$

Table 7.2: Description of all parameters of the dimensionless analytical model.

Parameter	Description
ϕ	Angular frequency (rad)
$\bar{w}(\xi,\tau)$	Beam deflection (-)
$\bar{c}$	Beam distributed damping (-)
$\bar{g}$	Gravitational acceleration (-)
$\bar{m}_0$	Resonator mass (-)
$\bar{k}_0$	Resonator spring stiffness (-)
ϕ_s	Sampling frequency (rad)
ξ	Spatial coordinate (-)
τ	Temporal coordinate (-)
η	Unevenness amplitude (-)
κ_i	Unevenness frequency components (-)
$\bar{w}_v(\tau)$	Vehicle deflection (-)
$\bar{M}$	Vehicle mass (-)
$\bar{K}$	Vehicle spring stiffness (-)
α	Vehicle velocity (-)

and the dimensionless gravitational acceleration

$$\bar{g} = \frac{g t_0^2}{L} \tag{7.14}$$

The term $r(\xi)$ describes the unevenness of the pavement and the vehicle. The reader is referred to Subsection 7.1.2 for an extensive elaboration on this term. To separate the time from the spatial domain, a general solution was assumed of the form:

$$\bar{w}(\xi,\tau) = \sum_{k=1}^{N} W_k(\tau)\sin(k\pi\xi) \tag{7.15}$$

Substitution of Equation 7.15 into the equation of motion of Equation 7.12, multiplication of the equation by $\sin(m\pi\xi)$ and integrating the equation from 0 to 1 over ξ (orthogonality principle), results in the following system of ordinary differential equations. It was hereby taken into account that $\int_0^1 \mathrm{H}(\xi_i-\xi)f(\xi)\mathrm{d}\xi = \int_0^{\xi_i} f(\xi)\mathrm{d}\xi$ and $\int_0^1 \delta(\xi-\xi_i)f(\xi)\mathrm{d}\xi = f(\xi_i)$:

$$\begin{aligned}\frac{1}{2}\ddot{W}_m + I_m + \frac{1}{2}m^4\pi^4 W_m = \\ -\left(\bar{m}_0\sum_{k=1}^{N}\ddot{W}_k\sin(k\pi\xi_1) + \bar{k}_0\sum_{k=1}^{N}W_k\sin(k\pi\xi_1)\right)\sin(m\pi\xi_1) \\ -\left(\bar{m}_0\sum_{k=1}^{N}\ddot{W}_k\sin(k\pi\xi_2) + \bar{k}_0\sum_{k=1}^{N}W_k\sin(k\pi\xi_2)\right)\sin(m\pi\xi_2) \\ -\left(\bar{K}\left(\sum_{k=1}^{N}W_k\sin(k\pi\alpha\tau) - W_v - r(\alpha\tau)\right) - \bar{M}\bar{g}\right)\sin(m\pi\alpha\tau)\end{aligned} \tag{7.16}$$

where $\dot{W}_m$ denotes the first time derivative of $W_m(\tau)$ so $\dot{W}_m = \mathrm{d}W_m/\mathrm{d}\tau$, $m = 1...N$ and

$$I_m = \bar{c}\left(\int_0^{\xi_1}\sum_{k=1}^{N}\dot{W}_k\sin(k\pi\xi)\sin(m\pi\xi)\,\mathrm{d}\xi + \int_{\xi_2}^{1}\sum_{k=1}^{N}\dot{W}_k\sin(k\pi\xi)\sin(m\pi\xi)\,\mathrm{d}\xi\right) \tag{7.17}$$

is the damping term. Substitution of the general solution (Equation 7.15) into the equation of motion of the vehicle in Equation 7.8, gives

$$\bar{M}\ddot{W}_v + \bar{K}\left(W_v + r(\alpha\tau) - \sum_{k=1}^{N}W_k\sin(k\pi\alpha\tau)\right) = 0 \tag{7.18}$$

Equation 7.16 and Equation 7.18 together form the system of differential equations that fully describes the model. The system consists of $N+1$ equations. Before the system can be solved, it needs to be transformed into a system of $2(N+1)$ first order differential equations. For the sake of computational efficiency, all values were stored as floats with eight digits. Subsequently, the system was solved numerically by direct integration with a 7th order Runge-Kutta scheme (`ode78` in Matlab) and a time step of $1/\phi_s$.

7.1.2. Unevenness of the Road and Vehicle

The expression of the unevenness plays a key role in the model. The unevenness spatially describes the contact point between the spring of the moving mass and the beam. It comprises two aspects: the roughness of the pavement of the road and profile of the tyre. The unevenness is defined as a sum of sines:

$$r(\xi) = \eta \sum_{i=1}^{M} \epsilon_i s_i \sin\left(\frac{\kappa_i + \delta_i}{\alpha}\xi + \phi_i\right) \tag{7.19}$$

The description of the parameters can be found in Table 7.2. Besides those parameters, the expression is characterised by three random numbers: ϵ_i amplifies the amplitude by a number between 0.8 and 1.2, δ_i is a number between 0 and 50 to prevent spikes in the time domain of the unevenness equation and ϕ_i is the phase shift (number between 0 and 1). The random numbers are there to induce some randomness in the unevenness to make it more realistic.

The last unexplained parameter in Equation 7.19 is the vector s_i. This vector is the amplitude amplifier enabling to manually control the amplitude of certain components of the expression for the unevenness. In the default situation, s_i is a vector of ones describing only the roughness of the road and tyres. By changing the amplitude of separate unevenness components, the unevenness is able to describe any source of vibration that can exist in the vehicle-bridge interaction (VBI) system, for example pavement or tyre irregularities.

In the expression for the unevenness, κ_i is a vector containing the frequency components of the unevenness. In this paragraph, the origin and values of this vector are elaborated on. The roughness of the pavement was assumed to be of a white-noise process. However, to be able to change certain frequency components of this process to for example introduce irregularities, it was chosen to approximate the white-noise process with a sum of sines ($M = 70$) and within a certain frequency range. To make sure all modes of interest were excited, the frequencies range from approximately the eigenfrequency of the vehicle to the theoretical eigenfrequency of the resonators ($\kappa_1 <= \phi_v$ and $\kappa_M >= \phi_R$). Recalculating these boundaries to boundaries with dimensions, the wavelengths of the unevenness components vary from about 0.06 to 10 m (note that the dimensionless angular frequency is related to angular frequency by $\phi = \omega t_0$). The rest of the κ_i vector was evenly distributed between these boundaries.

The unevenness is an important model parameter since it induces vibrations in the coupled system. The unevenness expression describes the interaction between the road surface and vehicle tyre; when setting the unevenness to zero, only the gravitational force plays a key role. The extent of the effect of the unevenness is illustrated by comparing the responses of the system with and without unevenness. Figure 7.2 shows the acceleration response of the moving mass-spring system. In case of zero unevenness, the vehicle only vibrates in its eigenfrequency. The unevenness adds high-frequency energy content to the system which increases the amplitude of the response. The same can be seen in the response of the beam: without unevenness there is only energy close the the eigenfrequencies of the beam and the moving mass. Figure 7.2 also illustrates the importance of the frequencies components κ_i of the unevenness expression: the exact values of κ_i are found in the Fourier spectrum of the response of the vehicle as well as the beam.

7.1.3. Derivation for the Eigenfrequency Analysis of the Beam

The model for the eigenfrequency analysis of the beam is a simplified version of the model for the time-history analysis: the vehicle and unevenness were removed because only the characteristics of the beam are of importance. The beam was split up into three parts separated by the local resonators. A drawing of the simplified model is shown in Figure 7.3.

The first step in deriving the model for the eigenfrequency analysis is to separate the time domain from the spatial domain. This is done by substituting $\bar{w}_i(\xi,\tau) = W_i(\xi)e^{i\phi\tau}$ into the equation of motion of the beam (Equation 7.6) which yields:

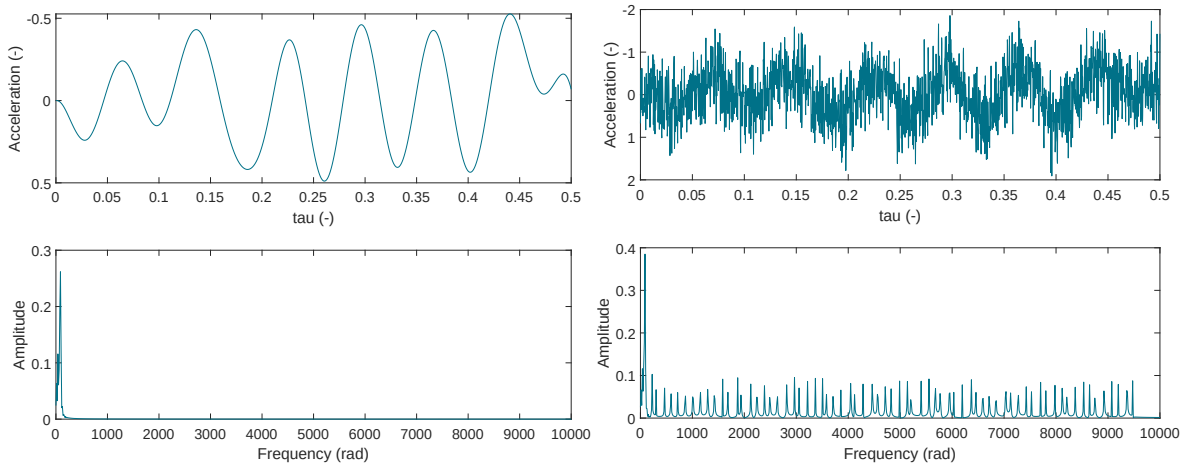

(a) Zero unevenness (b) Default unevenness

Figure 7.2: The acceleration response of the moving mass and its Fourier spectrum with and without unevenness.

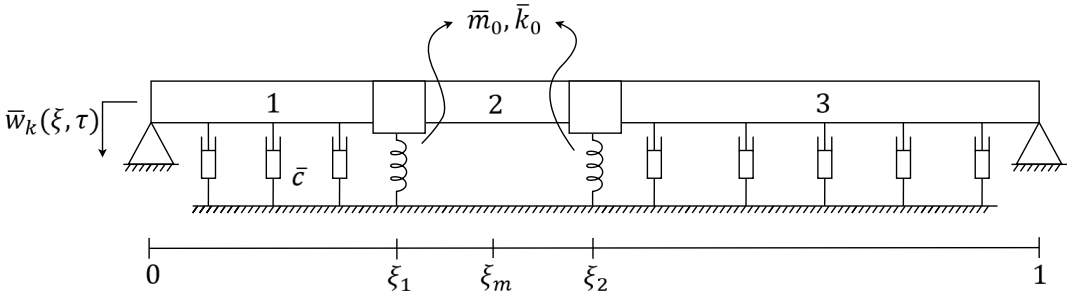

Figure 7.3: A drawing of the analytical model intended for the eigenfrequency analysis of the beam.

$$\begin{aligned} W_{1,3}'''' - \beta^4 W_{1,3} = 0 \\ W_2'''' - \gamma^4 W_2 = 0 \end{aligned} \tag{7.20}$$

where

$$\beta^4 = \phi^2 - i\phi\bar{c} \quad , \quad \gamma^4 = \phi^2 \tag{7.21}$$

For the sake of clarity, the spatial derivative is denoted with an accent in the remaining of this section, so $dW/d\xi = W'$. The general solutions of Equation 7.20 were assumed to be of the form:

$$\begin{aligned} W_1(\xi) &= A_1\cosh(\beta\xi) + B_1\sinh(\beta\xi) + C_1\cos(\beta\xi) + D_1\sin(\beta\xi) \\ W_2(\xi) &= A_2\cosh(\gamma(\xi-\xi_1)) + B_2\sinh(\gamma(\xi-\xi_1)) + C_2\cos(\gamma(\xi-\xi_1)) + D_2\sin(\gamma(\xi-\xi_1)) \\ W_3(\xi) &= A_3\cosh(\beta(\xi-\xi_2)) + B_3\sinh(\beta(\xi-\xi_2)) + C_3\cos(\beta(\xi-\xi_2)) + D_3\sin(\beta(\xi-\xi_2)) \end{aligned} \tag{7.22}$$

The general solution of the second and third part of the beam were shifted by ξ_1 and ξ_2 respectively to decrease the magnitude of the hyperbolic cosines and sines. This was necessary as the condition number of the coefficient matrix would be too high to be able to accurately solve the system for high frequencies.

Since the beam has three segments, there are a total of twelve unknown dynamic amplitudes. This system can be solved with four boundary conditions and eight interface conditions:

$$
\begin{aligned}
&W_1(0) = 0 && W_2(\xi_2) = W_3(\xi_2)\\
&W_1''(0) = 0 && W_2'(\xi_2) = W_3'(\xi_2)\\
&W_1(\xi_1) = W_2(\xi_1) && W_2''(\xi_2) = W_3''(\xi_2)\\
&W_1'(\xi_1) = W_2'(\xi_1) && W_3'''(\xi_2) - W_2'''(\xi_2) = \left(\varphi^2 \bar{m}_0 - \bar{k}_0\right) W_2(\xi_2)\\
&W_1''(\xi_1) = W_2''(\xi_1) && W_3(1) = 0\\
&W_2'''(\xi_1) - W_1'''(\xi_1) = \left(\varphi^2 \bar{m}_0 - \bar{k}_0\right) W_1(\xi_1) && W_3''(1) = 0
\end{aligned}
\tag{7.23}
$$

Substitution of Equation 7.22 into the boundary and interface conditions provides a system of 12 equations containing 13 unknowns (the 12 unknown amplitudes of the solution and the frequency ϕ). Then, a coefficient matrix $\mathbf{M} \in \mathbb{C}^{12\times12}$ can be composed containing the coefficients of the amplitudes. One obtains the eigenfrequencies of the system by solving the eigenvalue problem of this matrix

$$\det|\mathbf{M}| = 0 \tag{7.24}$$

which results in the complex frequency equation. The eigenfrequencies of the system are the roots of the frequency equation. Before these can be found, an intermediate step is required as the equation has entries with hyperbolic functions (e.g. $\sinh(\beta)$) which explodes for high frequencies decreasing accuracy and computational efficiency. This was done as follows: first, the hyperbolic functions were rewritten into exponential functions. Then, the positive exponentials were eliminated by dividing the equation by the exponential. Subsequently, the real part of the frequency equation was plotted to manually find its approximate roots. These real valued roots were used as starting point for the numerical Matlab solver `fsolve` (with a function tolerance of 1×10^{-10}) to find the complex valued roots of the frequency equation: the eigenfrequencies of the beam.

After obtaining the complex eigenfrequencies of the system, the mode shapes were plotted. This required the evaluation of the unknown amplitudes of Equation 7.22. Again, the general solution was substituted into the boundary and interface conditions of Equation 7.23. A coefficient matrix $\mathbf{A} \in \mathbb{C}^{11\times11}$ and vector $\mathbf{b} \in \mathbb{C}^{11\times1}$ were composed from the first eleven equations. The exploding hyperbolic terms in the matrix were eliminated by the following steps: $\mathbf{A}$ was rewritten into exponential functions, the rows of $\mathbf{A}$ and $\mathbf{b}$ containing positive exponential terms were divided by this term and the rows were divided by its belonging factor of β or γ. These steps reduced the condition number of the matrix significantly which was necessary to produce results that complied with the boundary conditions. After this, the found eigenfrequencies were substituted into the matrix. The amplitudes were obtained by solving the matrix equation:

$$\mathbf{A}\mathbf{x} = \mathbf{b} \tag{7.25}$$

where $\mathbf{x} \in \mathbb{C}^{11\times1}$ is a vector containing the first eleven unknown amplitudes. The solution depends on the 12th unknown amplitude D_3. Dividing the solution by D_3 provides the relative mode shapes. The results of the model can be found in the next sections.

7.2. Model Parameter Selection

This section introduces and explains the default values of the input parameters of the model. Table 7.3 presents the default input parameters used for the analyses. Later in this chapter, parametric studies are performed in which the input parameters are varied to see their influence on the results. As a reminder, a description of the parameters can be found in Table 7.2. One should note that the precise choice of the parameters is arbitrary: the optimal or most realistic values are not known. The model is not a direct representation of the Haringvlietbrug. Still, there were guiding lines (e.g. ratios between different parameters) when selecting the input parameters. They are explained below for each parameter.

First of all, the mass of the vehicle was chosen to be 5% of the mass of the bridge, a realistic value for the situation at the Haringvlietbrug. The vehicle suspension stiffness was subsequently chosen such that the eigenfrequency of the mass-spring system equalled about 90 rad (or 1 Hz in the system with dimensions). The parameters of the local resonators were selected based on two conditions: the stiffness should by far higher than the stiffness of the beam and the eigenfrequency of the resonators should be about 100 times higher than the eigenfrequency of the moving mass. Note that the eigenfrequency of the resonators is an approximation as the mass of the resonators is attached to the beam (the approximation is quite accurate because the stiffness of the resonator is far higher than the stiffness of the beam). In the current configuration, the eigenfrequency of the uncoupled resonator is 8.8×10^3 rad. It was important to be able to distinguish

Table 7.3: The input parameters of the analytical model with two resonators.

Parameter	Value
ξ_1	38/100
ξ_2	45/100
$\bar{k}_0$	6.0×10^6
$\bar{m}_0$	7.6×10^{-2}
$\bar{K}$	4.0×10^2
$\bar{M}$	5.0×10^{-2}
α	2.0
$\bar{c}$	1.0×10^3
η	1.0×10^{-5}
ϕ_s	$10{,}000\pi$ rad

the modes in which the resonators are excited from the modes labelled as local mode shapes (belonging to the middle beam). This was controlled by changing the distance between the resonators: a larger distance decreases the eigenfrequencies of the local modes. With the current choice of parameters, a velocity of 50 km/h (the speed limit on the Haringvlietbrug) can be rewritten to a dimensionless velocity of approximately 2.0. Lastly, for the damping coefficient, the lowest possible value was chosen with which vibrations damped out sufficiently fast enough and did not reflect against the boundaries of the system.

7.3. Model Performance Analysis

The performance of the semi-analytical model was tested by analysing and comparing the results of the eigenfrequency analysis and the time-history analysis when using the default input parameters. The goal of the eigenvalue analysis was to obtain the eigenfrequencies and mode shapes of the beam as shown in Figure 7.3. This was done according the methodology presented in Subsection 7.1.3. The eigenfrequencies were complex because of the damping but in the remaining of this section only the real part of the eigenfrequencies are shown. The model produced 33 eigenfrequencies and mode shapes in the frequency domain between 0 and 10,000 rad. Mode shapes in which either the part of the beam in between the resonators or the resonators themselves had a large amplitude relative to the rest of the beam belonged to modes of interest. Five modes were identified in the former category (in the frequency range from 2068 rad to 4716 rad, one of them shown in Figure 7.4a) and two in the latter (at 7314 rad and 7326 rad and displayed in Figure 7.4b). Lastly, three modes were found in which both ξ_m and the resonators were excited (between 8041 rad and 9445 rad, Figure 7.4c). This mode is a global mode of the beam as the amplitude of the mode shape is spatially almost constant. The dominance of the modes in which the middle beam or the resonators are dominantly excited makes sense as no damping is present at this part of the beam. This behaviour is also visible considering the complex eigenfrequencies: the imaginary part of the above modes is significantly smaller than the imaginary part of global modes.

With the same input parameters, the time-history analysis was performed. The eigenfrequency analysis showed there are 33 modes in the frequency domain of 0 to 10,000 rad. Therefore, also 33 modes were included in the time-history analysis ($N = 33$). Figure 7.5 shows the acceleration response in both the time and frequency domain (Fourier spectrum) on two different locations at the beam: Figure 7.5a at midspan ξ_m in between the local resonators and Figure 7.5b right above the resonator at ξ_2. The frequency response at ξ_m is characterised by two dominant energy fields: between the frequencies 2500 rad and 6000 rad (with a maximum around 3000 rad) and 8000 rad and 9500 rad (with a peak around 9000 rad). The frequency spectrum at ξ_2 only contains a significant concentration of energy between 7000 rad 9500 rad with a very clear peak at about 7565 rad. The eigenfrequencies of the bridge are difficult to identify in the spectrum due to the dominant presence of the components of the unevenness in the spectrum and the high damping.

The Fourier spectrum of the acceleration response of the beam shows the effect of the local resonators. Without the resonators, most energy most energy would be concentrated at fundamental modes of the system. Now, the high-energy modes are higher-order modes which means the local resonators do what they were meant to do: induce local modes of vibration more dominantly than global modes. In addition, it is clear that the current model settings provide a realistic signal-to-noise ratio in the time domain compared with the analysed passages in Chapter 4 and that the reflection of the waves against the boundaries of the

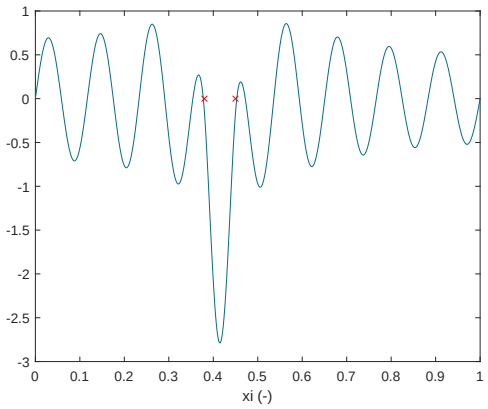

(a) 17th mode: $\phi = 3015$ rad

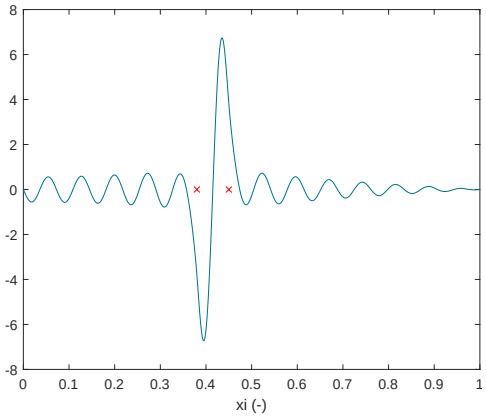

(b) 27th mode: $\phi = 7326$ rad

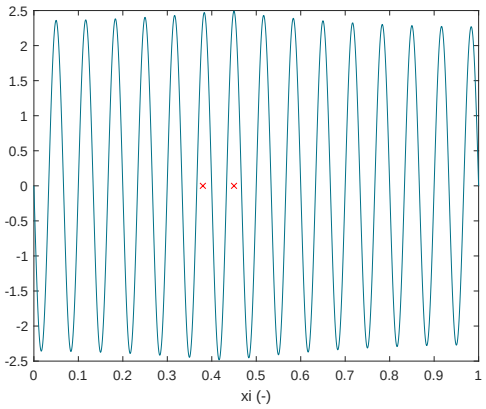

(c) 31st mode: $\phi = 8858$ rad

Figure 7.4: Three mode shapes of the model with default input parameters. The locations of the local resonators are indicated with the red crosses. The mode in a was identified as local mode in the beam in between the resonators, the mode in b as mode induced by the resonators and the mode in c by both. The real part of the eigenfrequency is shown as subscript.

system does not occur.

The results of the time-history analysis confirm the results of the eigenfrequency analysis as the modes found in the eigenfrequency analysis can also be found in the results of the time-history analysis: for example, the eigenfrequencies of the modes in which the middle beam is most dominantly excited according to the eigenfrequency analysis (Figure 7.4a), contain most energy in the time-history analysis at ξ_m (Figure 7.5a). The same similarities between the analyses are found considering the modes in which the resonators are excited and the global modes. This also means that including 33 modes in the time-history analysis was sufficient as all modes of interest were included in this frequency range.

However, the results of the two analyses do not match perfectly as the peaks in the Fourier spectrum of time-history analysis were slightly shifted compared to the identified eigenfrequencies in the eigenfrequency analysis. For example, the mode in which the local resonators were excited dominantly had an eigenfrequency of 7327 rad according to the eigenfrequency analysis (Figure 7.4b) while the peak belonging to the same mode was at 7565 rad in the time-history analysis (Figure 7.5b); a shit of about 3%. Two potential reasons were identified for this frequency shift. Firstly, there was no vehicle present in the eigenfrequency analysis but there was in the time-history analysis. The peaks in the resulting spectrum of the time-history analysis represent the instantaneous eigenfrequencies of the beam: time-variant eigenfrequencies determined by the interactive system between the beam and the vehicle. Secondly, the shift might partly be explained by numerical errors as the system was solved numerically in both analyses.

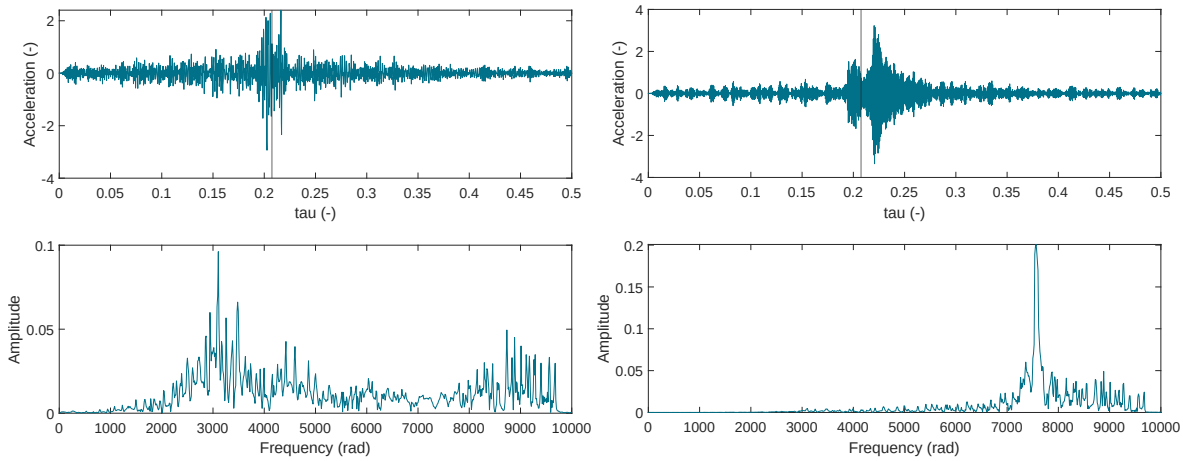

(a) $\xi = \xi_m$ (b) $\xi = \xi_2$

Figure 7.5: The acceleration response of the beam and its Fourier spectrum obtained with the model with default parameters. The vertical line in the time domain is when the moving mass passes ξ_m.

7.4. Parametric Studies: Results and Discussion

All input parameters of the model were varied to investigate their influence on the response of the beam in the time and frequency domain by inspecting the results of the time-history and eigenfrequency analyses. The results of the parameter shifts were compared to the results of the model with default input parameters (the eigenfrequency analysis in Figure 7.4 and the time-history analysis in Figure 7.5a). The parameters of the model were divided into two categories: fixed parameters belonging to the beam and variable parameters belonging to the vehicle and unevenness. Firstly, the influence of the fixed parameters are discussed and after that the variable parameters.

7.4.1. Fixed Parameters

The fixed parameters of the presented model are the distance between the local resonators, the damping coefficient and the characteristics of the local resonators.

Distance between the resonators $\xi_2 - \xi_1$ The distance between the resonators in the default settings was 7/100. This distance was increased to 13/100 to investigate its influence on the results. The response of the beam at midspan is shown in Figure 7.6. The Fourier spectrum shows now three high-energy frequency bands: around 1000 rad, 6000 rad and 9000 rad. According to the mode shapes obtained from the eigenfrequency analysis, the band around 1000 rad belongs to the first local mode shape of the middle beam (which peaked around 3000 rad in the model with default parameters), the second band belongs to the third local mode shape of the middle beam and the third band to global modes of the beam (the latter modes were not shifted compared the model with default settings). The first local mode of the middle beam shifted to a lower frequency when increasing the distance between the local resonators. This was as expected because it makes sense that increasing the distance between the resonator, so increasing the length of the middle beam and decreasing its stiffness, decreases the eigenfrequencies of this part as well.

Damping $\bar{c}$ Decreasing the damping coefficient decreased the signal-to-noise ratio in the time domain as visible in Figure 7.7. In the frequency domain, the peaks are more distinguishable because they are narrower which is as expected when decreasing the amount of damping. In addition, the peak at about 9000 rad has the largest magnitude in this case. This peak belongs to a global mode as became clear from the eigenfrequency analysis. Hence, the damping coefficient is here too low to make local modes the most dominant modes. Keep here in mind that global modes are damped most severely compared to local modes of the middle beam as there is no damping in between the local resonators.

Resonator eigenfrequency ϕ_R When decreasing the eigenfrequency of mass-spring system of the resonators by about 30% by either decreasing the stiffness or increasing the mass, two main changes are visible in Fig-

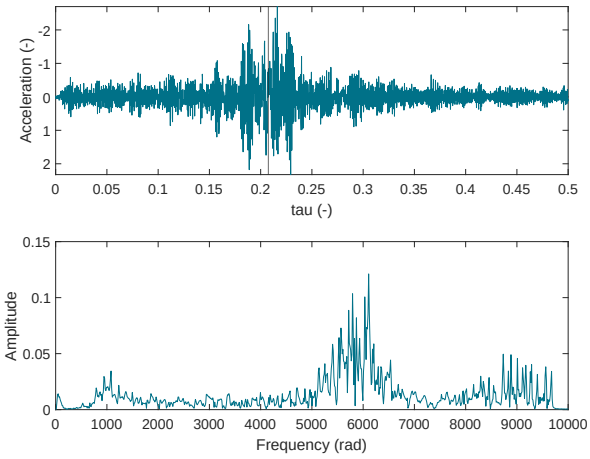

Figure 7.6: The acceleration response of the beam at ξ_m and its Fourier spectrum with $\xi_2 - \xi_1 = 0.13$. The vertical line in the time domain is when the moving mass passes ξ_m.

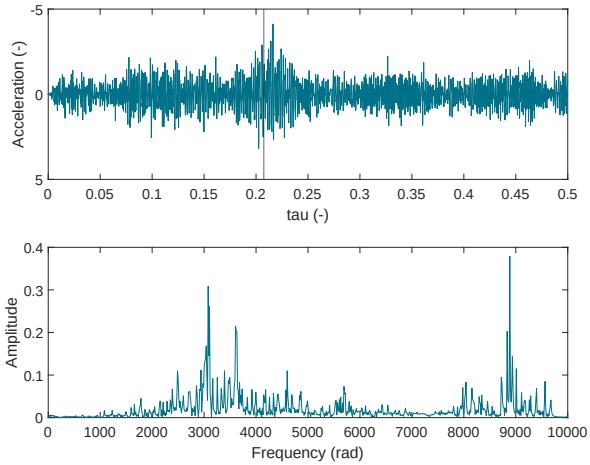

Figure 7.7: The acceleration response of the beam at ξ_m and its Fourier spectrum with $\bar{c} = 100$. The vertical line in the time domain is when the moving mass passes ξ_m.

ure 7.8 for which the mass of the local resonators was doubled. In Figure 7.8a, the second high-energy frequency band of the spectrum decreased in amplitude and spread over more frequencies (from 6000 rad to 9500). In Figure 7.8b, the frequency of the high and distinctive peak decreased with about 25% compared to the model with default settings. The frequency shift in the response of the beam is smaller than the eigenfrequency shift of the resonator because the mass of the resonator is rigidly attached to the beam: the stiffness of the beam limits the frequency shift.

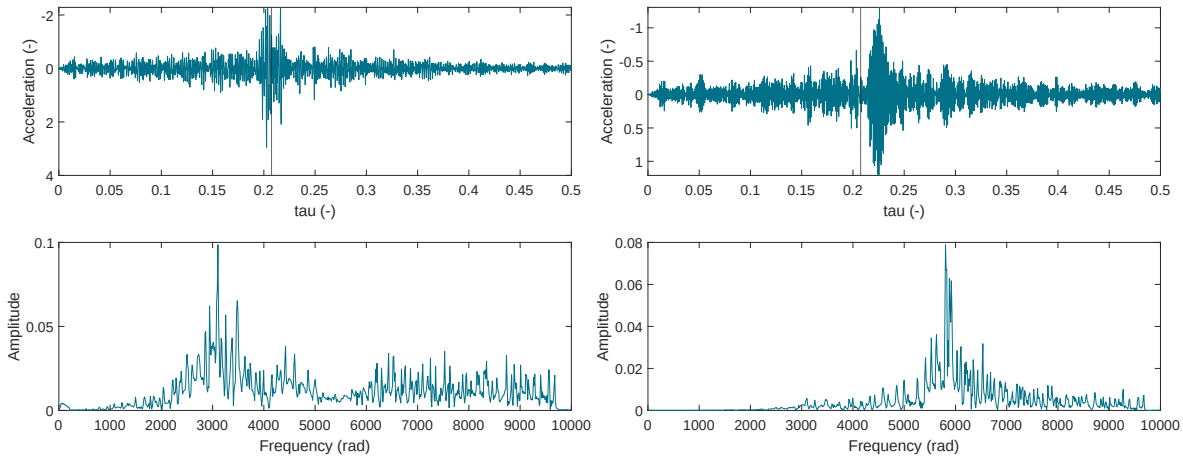

(a) $\xi = \xi_m$ (b) $\xi = \xi_2$

Figure 7.8: The acceleration response of the beam at and its Fourier spectrum with when the eigenfrequency of the local resonators is reduced by 30%. The vertical line in the time domain is when the moving mass passes ξ_m.

Resonator parameters $\bar{k}_0$ and $\bar{m}_0$ In this analysis, the stiffness and mass of the resonator were both decreased by 90%. Hence, the eigenfrequency of the resonators did not changed. Both the spectra of Figure 7.9a and b, however, show a distinctive peak at 2300 rad, which was not present in the results of the model with default parameters. Apparently, both the midspan between the resonators and the resonators themselves were excited. This was confirmed by the resulting mode shape from the eigenfrequency analysis in Figure 7.9c. It can be concluded that the resonators were not sufficiently stiff to induce local mode shapes in the middle beam.

The above parametric studies of fixed input parameters confirm the results of the eigenfrequency analysis of which high-energy frequency band belongs to which mode. Three high-energy frequency bands were distin-

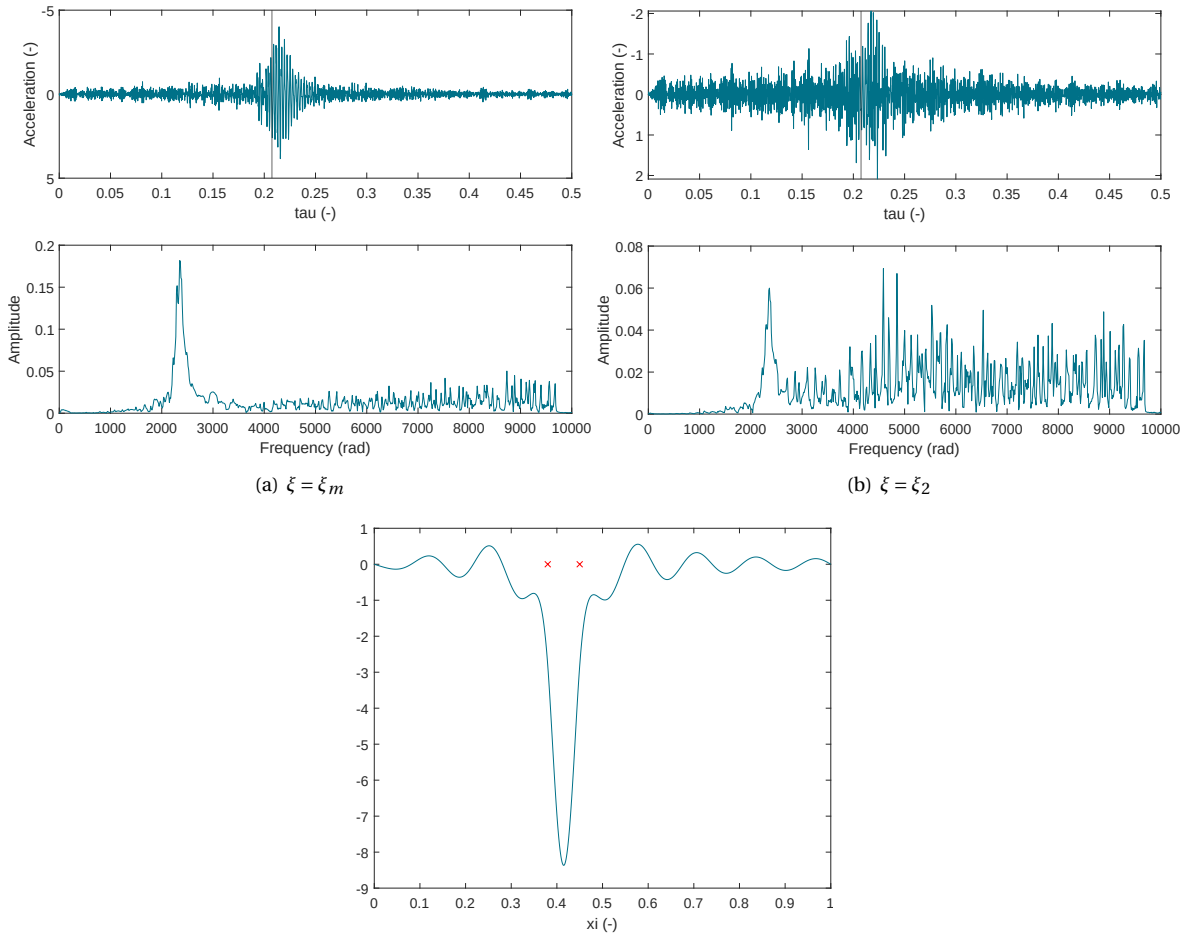

(a) $\xi = \xi_m$ (b) $\xi = \xi_2$

(c) $\phi = 2305$ rad

Figure 7.9: The acceleration response of the beam and its Fourier spectrum (a and b) and a mode shape (c) with $0.1\bar{k}_0$ and $0.1\bar{m}_0$. The vertical line in the time domain of a and b is when the moving mass passes ξ_m.

guished in the response with default settings in Figure 7.5: a band between 2500 and 6000 rad, a sharp peak at 7500 rad and a band between 8000 and 9500 rad. The first frequency band is likely to belong to local modes of the middle beam, the second peak to the mode induced by the local resonators and the third band to modes where both the resonators and the midspan of the middle beam are excited. As this research focused on the local modes of the beam between the resonators, the first frequency band is the most interesting one for further analyses. It became clear that most fixed parameters significantly influence the response of the beam but for the remaining of this report they are fixed and their default values are used.

7.4.2. Variable Parameters

The variable parameters of the model are the characteristics of the moving mass, the velocity of the moving mass and the unevenness.

Vehicle parameters $\bar{K}$ and $\bar{M}$ The influence of the vehicle parameters on the bridge response was limited as the eigenfrequency of the vehicle is far lower than the eigenfrequencies of the local modes of the beam. This is illustrated by Figure 7.10a where both the stiffness and mass of the vehicle were multiplied by 100 (so the eigenfrequency of the vehicle remains equal): the shape of the response did not changed compared to the response with default settings in Figure 7.5a. Only the amplitudes of the response in both the time and frequency domain increased more or less proportionally. This was expected: since the system is linear, a stiffer spring causes a linear amount of extra energy to be present in the system. The same holds for the vehicle mass: when increasing the mass, the static load of the gravity also increases. Its influence on the magnitude of the response was, however, smaller (the peak acceleration of the beam increased linearly from

4.29 to 4.31 when increasing $\bar{M}$ from 0.01 to 0.1).

The vehicle did influence the shape of the response spectrum of the beam (slightly) when increasing its eigenfrequency drastically to 2000 rad to get close to the dominant eigenfrequencies of the beam as visible in Figure 7.10b. To do this, the stiffness of the vehicle was multiplied by 500. The effect is still limited. Yet, frequencies in the response close to the eigenfrequency of the vehicle contain relatively more energy compared to the modes around 8500 rad than before. However, it should be noted that the latter vehicle characteristics are not realistic.

Also the more realistic quarter-vehicle model instead of the single degree-of-freedom (SDOF) vehicle model was introduced to see if that would increase the influence of the vehicle on the response of the beam. This, however, appeared not to be the case while making the model computationally more expense to execute. Therefore, it was chose to continue with the SDOF vehicle model. More information on the 2DOF quarter-vehicle model can be found in Appendix Section A.4.

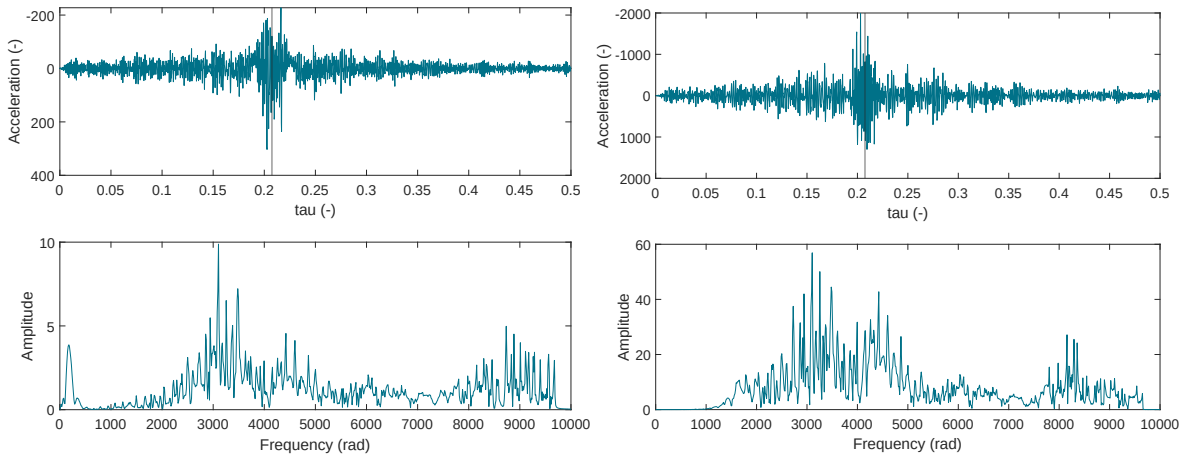

(a) $100\bar{K}$ and $100\bar{M}$ (b) $\phi_v = 2000$ rad

Figure 7.10: The acceleration response of the beam at ξ_m and its Fourier spectrum with changing vehicle parameters. The vertical line in the time domain is when the moving mass passes ξ_m.

Vehicle velocity α In Figure 7.11a, the peak response acceleration of the beam is plotted against the vehicle velocity. The peak acceleration on the y-axis of the graph is the maximum acceleration of the beam over time and spatially (the peak response is not necessarily at midspan because of the oscillating vehicle mass). Although a weak downwards trend is visible, the graph is characterised by peaks. These peaks are critical velocities α_{cr}. Approximately the same pattern was visible when doing the same analysis with zero unevenness. Hence, the peaks were not caused by resonance with the unevenness frequency components. The downwards trend (this trend is more dominant when considering the peak displacement of the beam) is likely to be caused by the fact that with increasing velocity the vehicle is shorter present on the beam. This way, less energy can be transferred. Figure 7.11b shows that for an further increasing velocity the trend becomes upwards and peaks when the vehicle velocity approaches the phase velocity of the beam. In literature, many examples of the relation between the vehicle velocity and peak acceleration of the beam can be found (e.g. Gonzalez & Schmidt, 2018) and most of them have approximately the same results: the amplitude of the response oscillates for low frequencies and significantly increases when the velocity approaches the phase velocity of the beam.

In contrast to the significant influence of the velocity in the time domain, the influence in the frequency domain is limited. No significant energy shifts occur as can be seen in Figure 7.11c in which the velocity is quadrupled between the upper and lower graph. It makes sense that the shape of the response of the beam did not change because the unevenness was defined so that the boundaries of the unevenness components were independent from the vehicle velocity. Only the influence of the eigenfrequency of the vehicle on the response of the beam gets more dominant for an increasing vehicle velocity. Additionally, one should note that the resolution of the frequency spectrum decreases for an increasing velocity since the vehicle is shorter on the beam.

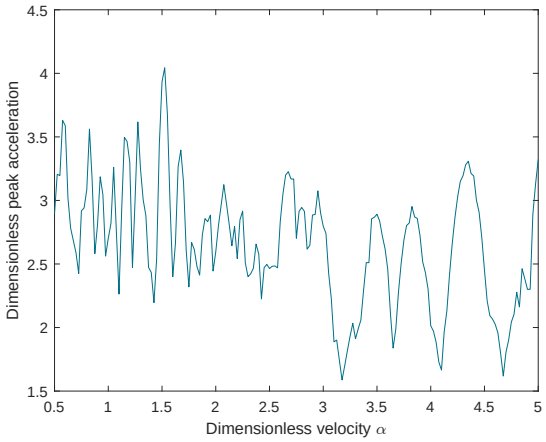

(a) The peak acceleration of the beam with a vehicle velocity between 0.5 and 5.0

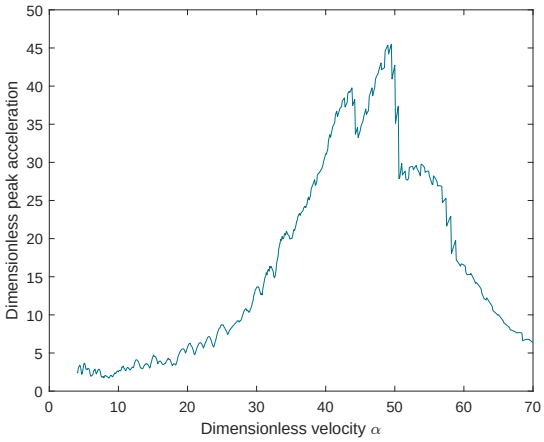

(b) The peak acceleration of the beam with a vehicle velocity between 4 and 70

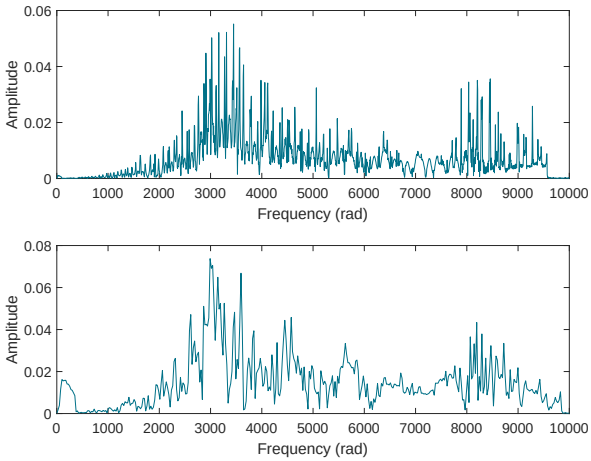

(c) The Fourier spectra of the acceleration response of the beam at ξ_m for two vehicle velocities ($\alpha = 1$ in the top figure and $\alpha = 4$ in the bottom figure)

Figure 7.11: Response of the beam to changes in vehicle velocity.

Unevenness of the road and vehicle $r(\xi)$ In Subsection 7.1.2, the expression for the unevenness of the road and tyre was introduced. This section investigates the sensitivity of the model to changes in the unevenness. The influence of two variables in the expression on the response of the beam were investigated: amplitude η and amplifier s_i. When changing η the amplitudes of all frequency components were changed while changing s_i can change the amplitudes of separate components.

Changing the amplitude of all components of the unevenness by changing η has the same effect on the results as changing the stiffness of the moving mass: only the amplitude of the response of the beam changes, not the shape of the response. As the system is linear, the amplitude of the response increases proportionally with the amplitude of the unevenness components which is shown in Figure 7.12. Here, the amplitude was multiplied by 10 which also approximately resulted in a beam response with an amplitude multiplied by 10 compared to the model with default settings. This approximate relation was also found by the numerical model of Gao *et al.* (2015).

Next, the sensitivity of the model to the unevenness is investigated by playing with the the amplifier vector s_i. With this vector, certain frequency components or groups of frequency components of the unevenness can be either damped or amplified. It is not complicated to make a parallel to reality. The unevenness is a combination of two physical processes: the unevenness of the road surface and irregularities of the vehicle's tyre. A situation in which all frequency components of the unevenness are equal in magnitude is unlikely; for example, the road could have a pattern in a certain frequency or the tyre could have non-uniformities

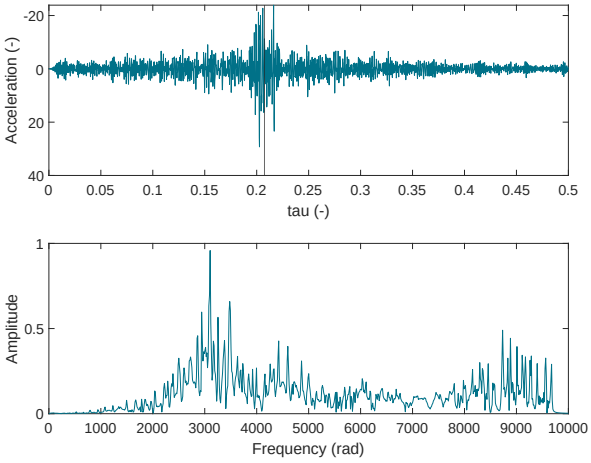

Figure 7.12: The acceleration response of the beam at ξ_m and its Fourier spectrum with $\eta = 1.0 \times 10^{-4}$. The vertical line in the time domain is when the moving mass passes ξ_m.

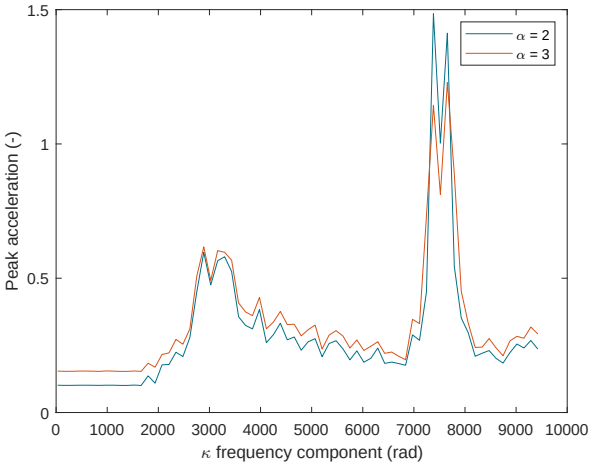

Figure 7.13: The peak acceleration with a varying single component of κ.

(as explained in Section 2.2). It can be said that the unevenness determined the load frequencies of the system. Two configurations of s_i were investigated: setting all but one entry to zero and amplifying a single component or a group of components.

Firstly, the sensitivity to the load frequencies κ_i was analysed by running the model with one unevenness component at the time. The result is shown in Figure 7.13. Here, the peak acceleration of the response of the beam is compared to the unevenness frequency. As expected, the largest response was obtained when the unevenness component was close to the eigenfrequencies of the beam.

Next, the effects of the amplification of (groups of) certain unevenness components using vector s_i were investigated. Two cases are displayed in Figure 7.14: a shows the case where one frequency component ($\bar{\kappa}_{40} = 6029$ rad and $s_{40} = 8$) is dominant for example caused by irregularities of the tyre. A distinctive concentration of energy consisting of three peaks is clearly visible in the spectrum. In Figure 7.14b, there is a group of dominant frequency components (from $\bar{\kappa}_{40} = 5400$ rad to $\bar{\kappa}_{45} = 6029$ rad and $s_{40:45} = 8$). The same was observed as changing η: if an unevenness component was doubled in magnitude, the response of the beam at this frequency also approximately doubled. No literature was found about the effect of a single dominant unevenness frequency on the dynamic response of the bridge deck but considering the dynamic response of the vehicle, the results of the model are in accordance with Camara *et al.* (2017).

Changing the amplitude of certain unevenness components can change the shape of the frequency spectrum of the beam response drastically. Peaks can form at frequencies containing low energy with the default input parameters. Or the other way around, peaks in the spectrum can almost disappear if the unevenness does not contain those frequencies. However, no energy shift occurs: peaks belonging to eigenfrequencies of the beam remain in the spectrum at equal frequency and with equal magnitude. In the time domain, a dominant unevenness component can cause a significant increase in peak acceleration which is in accordance with literature investigating the effect of tyre or pavement irregularities (e.g. Michaltsos & Konstantakopoulos, 2000).

The sensitivity of the model to its variable parameters varied. On the one hand, the influence of the mass, stiffness and velocity of the moving mass was limited to changes in amplitude of the response of the beam. The unevenness, on the other hand, was able to influence both the amplitude and the shape of the Fourier spectrum of the response. In the next section, another variable parameter is introduced: the presence of multiple moving masses on the beam.

7.5. Multiple Moving Masses

In addition to the model parameters discussed previously, the effects of multiple moving masses on the dynamic response of the beam were explored. The masses represent different axles of a vehicle or axles of different vehicles. The model with two moving masses is depicted in Figure 7.15 in which the distance between the masses is indicated by θ_2.

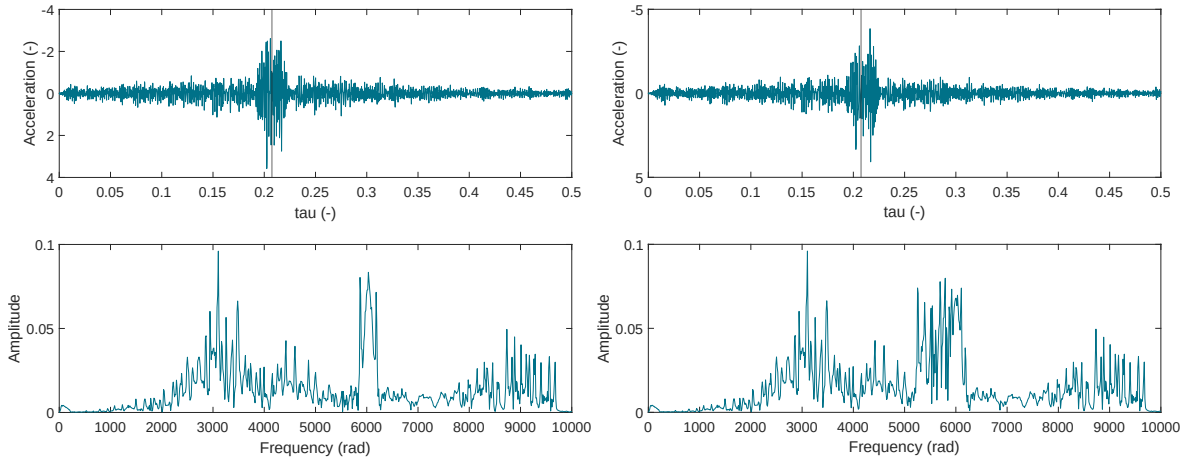

(a) One dominant unevenness component ($\bar{\kappa}_{40}$ = 6029 rad and s_{40} = 8)

(b) A group of dominant unevenness components (from $\bar{\kappa}_{40}$ = 5400 rad to $\bar{\kappa}_{45}$ = 6029 rad and $s_{40:45}$ = 8

Figure 7.14: The acceleration response of the beam at ξ_m and its Fourier spectrum and the effect of changes in the unevenness amplitude amplifier. The vertical line in the time domain is when the moving mass passes ξ_m.

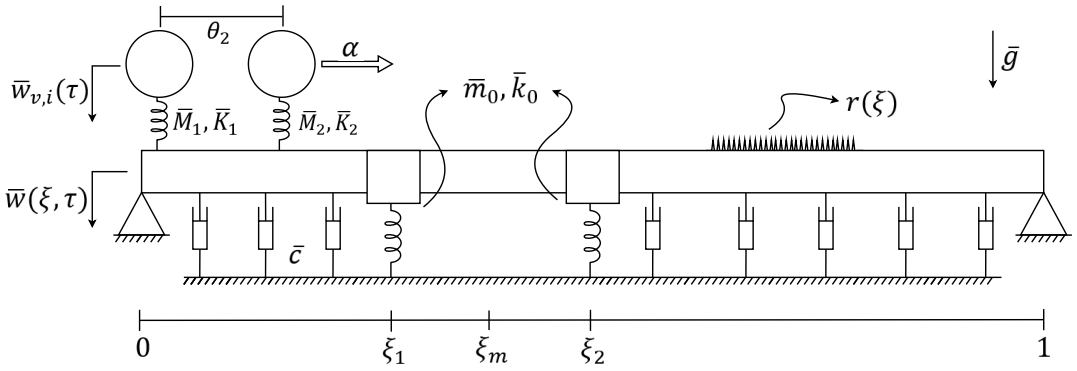

Figure 7.15: A drawing of the full analytical model with two moving masses.

The model can be extended to also include more moving masses. For this, additional components and equations were added to the system of differential equations which describes the model (Equation 7.16 and Equation 7.18), leading to a new system of equations:

$$\begin{aligned}\frac{1}{2}\ddot{W}_m + I_m + \frac{1}{2}m^4\pi^4 W_m = \\ -\left(\bar{m}_0\sum_{k=1}^{N}\ddot{W}_k\sin(k\pi\xi_1) + \bar{k}_0\sum_{k=1}^{N}W_k\sin(k\pi\xi_1)\right)\sin(m\pi\xi_1) \\ -\left(\bar{m}_0\sum_{k=1}^{N}\ddot{W}_k\sin(k\pi\xi_2) + \bar{k}_0\sum_{k=1}^{N}W_k\sin(k\pi\xi_2)\right)\sin(m\pi\xi_2) \\ -\left(\bar{K}_i\left(\sum_{k=1}^{N}W_k\sin\big(k\pi(\alpha\tau-\theta_i)\big) - W_{v,i} - r_i(\alpha\tau-\theta_i)\right) - \bar{M}_i\bar{g}\right) \\ \cdot\sin(m\pi(\alpha\tau-\theta_i))\,H\left(\tau-\frac{\theta_i}{\alpha}\right) \qquad (7.26)\end{aligned}$$

$$\bar{M}_i\ddot{W}_{v,i} + \bar{K}_i\left(W_{v,i} + r_i(\alpha\tau-\theta_i) - \sum_{k=1}^{N}W_k\sin(k\pi(\alpha\tau-\theta_i))\right) = 0 \qquad (7.27)$$

where $i = 1..N_{\text{axles}}$ and N_{axles} is the total amount of moving masses. One should note that θ_1 is always equal

to 0 and that θ_i is the distance between the first and i-th axle. A Heaviside function is used to only include the moving mass as soon as it enters the beam. The extended system consists of $N + N_{\text{axles}}$ equations.

For now, only the presence of two moving masses is investigated. With the presence of an additional and similar moving mass, there is a period of time within which a point on the beam is subjected to the same point load twice: the time delay. The time delay results in the modulation of the signals: some frequencies are amplified and others are damped in the Fourier spectrum of the sum of the loads. The amplified frequencies are equal to the inverse of the time delay and its infinite number of integer multiples. The frequency amplification is dependent on the the vehicle velocity and axle distance:

$$\phi_d = \frac{2\pi n\alpha}{\theta_2} \tag{7.28}$$

where ϕ_d are the amplified frequencies and n is any integer with a value of zero or larger. If the force subjected by both masses is equal, the envelope of the load in the frequency domain is given by Equation 7.29 (adapted from Milne *et al.*, 2017). This expression originates from the Fourier transform of the loads in case of a white-noise unevenness (spacing between the unevenness frequency components going to zero).

$$U = \left| P\cos\left(\frac{\theta_2}{2\alpha}\phi\right)\right| \tag{7.29}$$

where P is the magnitude of the amplified frequencies.

Whereas the load spectrum of the model with one moving mass is dominated by the eigenfrequency of the mass-spring system and the unevenness components, the load spectrum of the model with two moving masses is strongly influenced by the frequency amplification caused by the time delay between the moving masses. The extent of the effect is clearly visible in Figure 7.16. The effect was extensively studied for trains as the frequently repeated axle spacing makes the effect extra dominant (e.g. Fuchs & Bokelmann, 2018; Milne *et al.*, 2017). These studies show very similar behaviour of the dynamic response of the structure or soil (both measured and modelled) as the results of the semi-analytical model. Studies on this effect regarding road bridges are less common; the time delay effect was observed by some authors (Brady & O'Brien, 2006; Cantieni, 1992; Meyer, 2022) but its influence on the bridge deck was not investigated. No literature was found on that specific subject.

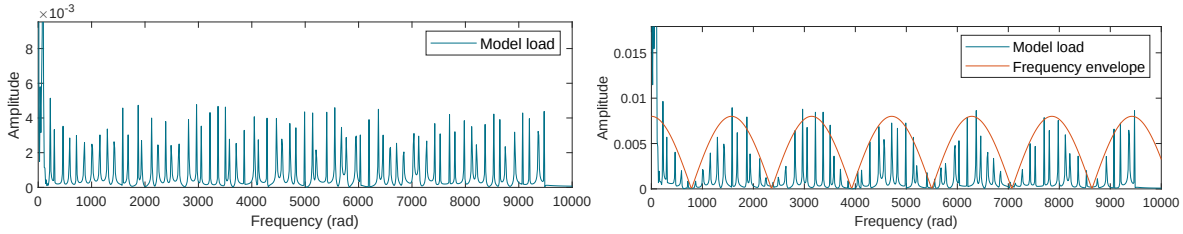

(a) One moving mass

(b) Two moving masses with $\theta_2 = 0.008$

Figure 7.16: The spectrum of the FT of the force in the spring of the moving mass (a) or the sum of forces in the springs of the moving masses with the same characteristics (b) on the beam.

The amplified frequencies alternate with frequencies with hardly any energy. A condition for this phenomenon to happen is that both masses move in phase. In addition, the effect is dominant when the subjected force on the beam is similar for both moving masses: when changing the characteristics of one of the moving masses, the energy is more evenly distributed along the width of the spectrum and peaks of the frequency envelope are smaller in magnitude. One cannot speak of a delayed force when either the phase or the load itself is different. Characteristics of the beam, including the damping coefficient, local resonator characteristics and the distance between the local resonators, do not influence the frequency amplifications.

Based on the results in the previous sections and the fact that the moving masses are the only loads the beam is subjected to, it was expected that the presence of the dominant frequencies caused by the time delay strongly influence the dynamic response of the beam. The expectation was confirmed by the time-history analysis of the model as shown in Figure 7.17 for two different axle distances: the frequency envelope of the load spectrum is directly transferred to the Fourier spectrum of the acceleration response of the beam. Modes

of the beam which frequency equals a frequency where the load energy approaches zero are barely excited. This is illustrated by Figure 7.17a, in which a low concentration of energy around a frequency of 3000 rad is present which is in contrast to the model with default parameters where most energy was concentrated around this frequency.

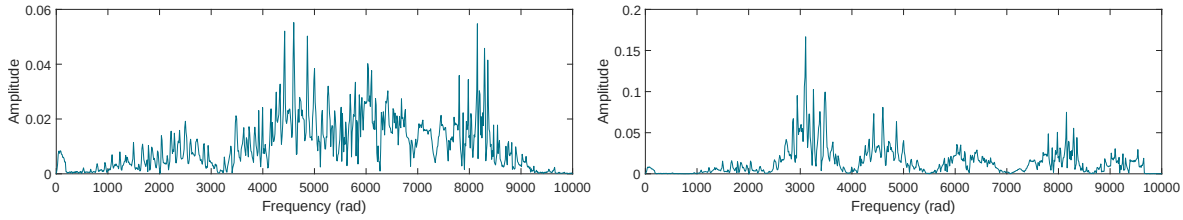

(a) $\theta_2 = 0.002$ (b) $\theta_2 = 0.008$

Figure 7.17: The spectrum of the FT of the acceleration response of the beam at ξ_m loaded with two moving masses.

7.6. Conclusion

In this chapter, a semi-analytical model was proposed to simulate local modes of vibration in the Haringvlietbrug. The model consisted of a damped Euler-Bernoulli beam with two local resonators and one or more moving mass(es). The model was studied parametrically to investigate the sensitivity of the model to the various input parameters.

The model parameters were divided into two groups: the fixed parameters belonging to the beam and local resonators and variable parameters like the vehicle characteristics and unevenness. In addition, the situation when multiple moving masses are on the beam at the same time was looked into. Below the variable parameters are arranged from most influential to less influential to the dynamic response of the bridge deck according to the results of the semi-analytical model as presented in this chapter:

- Multiple moving masses: the presence of multiple moving masses introduced a time delay between the point loads which strongly influenced the dynamic response of the beam. The time delay was dependent on the distance between the moving masses and their velocity. If the moving masses had the same characteristics and were moving in phase, frequencies which were integer multiples of the inverse of the time delay were amplified while intermediate frequencies were strongly damped. This caused that some modes of the beam, which were dominant in the model with default input parameters, were hardly excited for some time delay values.

- Unevenness: the combined unevenness of the pavement of the road and the tyres of the vehicle had a large impact on the results of the system as the unevenness can describe any source of vibration in the VBI system. A dominant frequency component of the unevenness can induce a concentration of energy at other frequencies than expected based on the eigenfrequency analysis. Furthermore, absence of unevenness frequency components close to the eigenfrequency of a mode could prevent this mode to be excited.

- Vehicle velocity: the acceleration response of the beam was sensitive to the velocity of the passing vehicles. However, changing only the velocity did not influence the shape of the Fourier spectrum of the response. The velocity did influence the frequency spectrum when also considering dominant unevenness frequencies and the time delay effect.

- Vehicle mass and spring stiffness: as the system was linear, the magnitude of the response increased proportionally to an increasing stiffness. A changing vehicle mass only influenced the response of the beam marginally. The shape of both the acceleration and frequency response did not change. The limited influence of these characteristics was mostly explained by the fact the eigenfrequency of the moving mass was much lower than the eigenfrequencies of interest of the beam.

These conclusions are coupled to the Haringvlietbrug recordings in the next chapter. This way, it was aimed to find important sources of the variability in the dynamic response of the Haringvlietbrug by inspecting the results of the model with variations of input parameters and to compare these with the recordings.

8

Characteristic Load Cases in the Model

The goal of this chapter is to improve the understanding of the large variability in the dynamic response of the Haringvlietbrug by comparing characteristic passages in the measurements with the output of the in Chapter 7 presented semi-analytical model. The parameters of the model were tuned to give potential explanations for these large variabilities. Environmental variabilities were ignored in this chapter as they are not of importance when considering short-term effects and they only cause a shift in the frequency spectrum rather than a change of shape. In this chapter, four characteristic cases as observed in the Haringvlietbrug measurements are discussed:

- Case I: Doppler effect
- Case II: wide-band frequency spectra
- Case III: semi-trailer trucks
- Case IV: passenger cars

The cases were based on either the acceleration response or its the Fourier spectrum of passages measured at the Haringvlietbrug and within a frequency range of 50 to 250 Hz. Furthermore, it is important to realise that these cases do not fully describe the variability found when considering all vehicle passages: the four cases represent the most characteristic or most interesting passages. Case IV illustrates the situation of a case without characteristic passages as a large variation in the recorded response exist. Hence, special attention is paid on other potential causes of variability.

One should note that the measurements of the Haringvlietbrug cannot be directly compared to the results of the model as the modelled structure does not resemble the actual structural characteristics of the Haringvlietbrug: the model is neither scaled, calibrated nor validated in respect to the actual structure of the Haringvlietbrug. Therefore, it was not expected that the shape and amplitudes of the resulting frequency spectra of the measurement and the model were similar. The model was only used to investigate the effect of changing parameters on the resulting response. Thus, the resulting changes can be compared with the measurements only qualitatively, not quantitatively.

The last statement also justifies the different frequency domains considered for the analyses. For the Haringvlietbrug, the frequency domain of interest was between 50 to 250 Hz because it was the aim to perform SHM with local modes of vibration somewhere in this domain. This domain was only used to observe characteristic behaviour. The model, on the other hand, simulated local modes with a dimensionless frequency range of 0 to 10,000 rad as determined by the frequency components of the expression of the unevenness. That is about 0 to 150 Hz recalculated to a domain with dimensions but as only relative shifts and changes of shapes in the frequency domain of the response were considered, the domains do not necessarily have to align.

8.1. Case I: Doppler effect

Numerous vehicle passages were found containing a large concentration of energy in one or two frequency bands with three peaks each in the Fourier transform of the Haringvlietbrug acceleration measurements. All

considered passages belonging to this case were also characterised by a large peak acceleration (> 0.2 m/s^2), but the location of the peaks in the frequency domain was different for all passages. Examples of case I passages are shown in Figure 4.9a and Figure 8.1.

The three peaks were caused by the Doppler effect. The Doppler effect is the phenomenon that the perceived frequency of the propagated wave by a source is increased when the source and observer move towards each other and decreased when they move away from each other. This behaviour can be observed in the spectrogram of the passage in Figure 8.1b: as soon as the vehicle passes the sensor (at $t = 1.4$ s), the dominant frequency decreases. This explains the three peaks in the Fourier spectrum: the peak with the lowest frequency is caused by the vehicle moving away from the sensor, the middle peak is caused when the vehicle is near the sensor (the frequency of this peak is equal to the source frequency) and the peak with the highest frequency is caused when the vehicle moves towards the sensor. The magnitude of the frequency shift depends on the vehicle velocity, the source frequency and the phase velocity. Both an increasing velocity and frequency result in a larger frequency shift. The Doppler effect can only exist when a system is time-variant. The current system is only time-variant by the operational variabilities when the environmental and structural conditions are assumed to be constant. It can, therefore, be concluded that the Doppler effect is caused by characteristics of the vehicles.

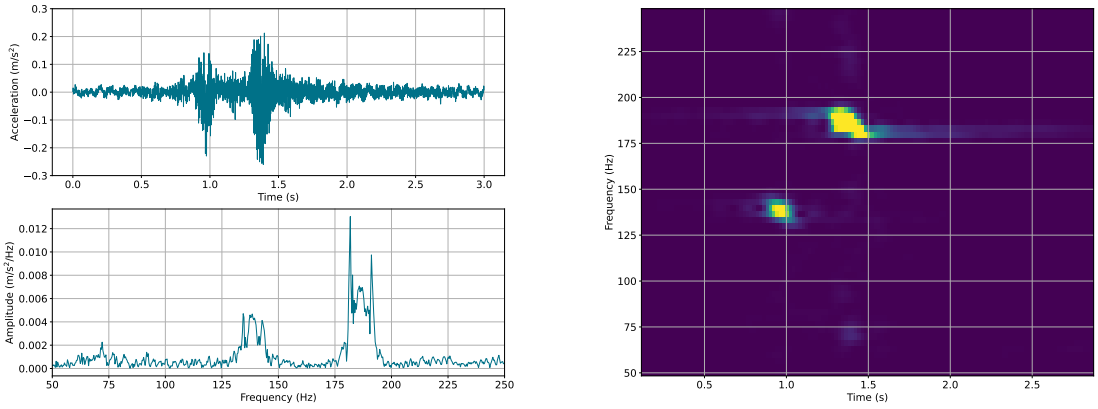

(a) Acceleration response and its Fourier spectrum

(b) Spectrogram

Figure 8.1: The acceleration response of sensor 17 at the Haringvlietbrug to a passage which belongs to load case I.

The case of a clear Doppler effect in the frequency response of the Haringvlietbrug was simulated with the semi-analytical model presented in the previous chapter. The recorded passage of Figure 8.1 was simulated using the model with two moving masses and default input parameters. The distance between the masses was chosen large enough that the masses do not influence each other by the time delay effect. The distinctive high-energy frequency bands were created by amplifying one unevenness frequency component for each moving mass significantly (25 times the original amplitude in this case). The dynamic beam response outputted by the model (Figure 8.2) shows strong similarities with the measurements. Again, the influence of the Doppler effect is also visible in the spectrogram of the passage.

What caused the passages with such a dominant Doppler effect to occur? In the model, it happened when there was a single very dominant unevenness component per axle. The model unevenness describes the roughness and irregularities of the road as well as the roughness of the tyre. Concluded earlier, the dominant frequency belongs to a time-variant source, so pavement irregularities did not cause the Doppler effect. Moreover, if the pavement would be the cause, the peaks were expected to be at approximately the same frequency for all passages. So, the case I passages are likely due to vibrations in the crossing vehicles for example caused by tyre irregularities or a crooked car suspension.

8.2. Case II: wide-band frequency spectra

Vehicle passages resulting in an acceleration response with a wide-band frequency spectrum belong to case II. Various examples of such passages were found in the data set. However, these passages had significant

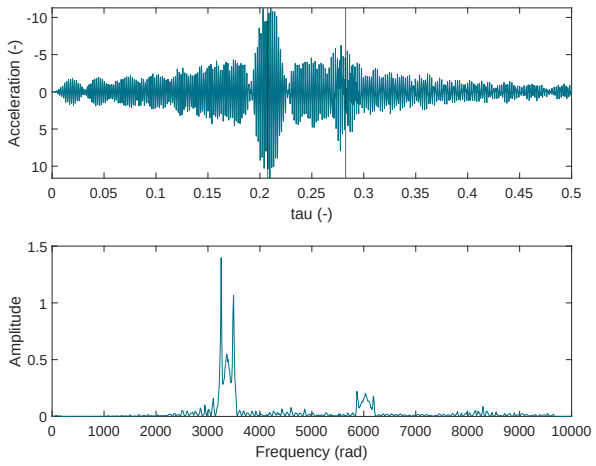

(a) Acceleration response (the vertical lines indicate the time a moving mass crosses ξ_m) and its Fourier spectrum

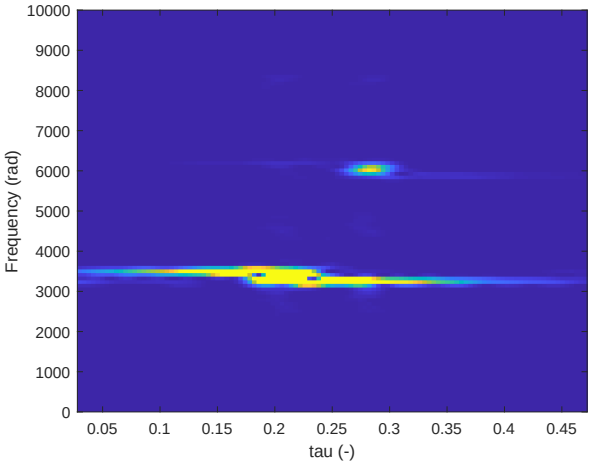

(b) Spectrogram

Figure 8.2: The acceleration response of the model at ξ_m simulating load case I.

differences between them in both the time and frequency domain. An example of a passage with a broad frequency response spectrum is given in Figure 8.3 which spectrum is characterised by a wide band containing a significant amount of energy and one distinctive peak at about 100 Hz. The spectrogram shows that the frequency content of the passage is rather constant in time.

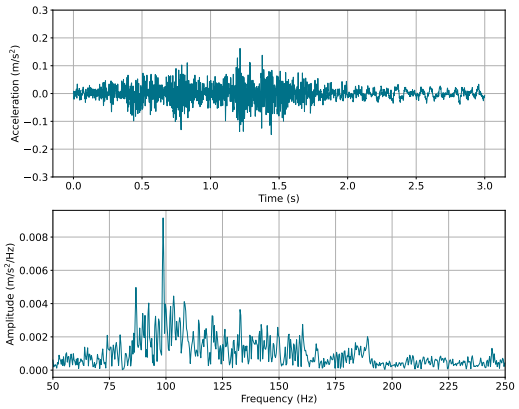

(a) Acceleration response and its Fourier spectrum

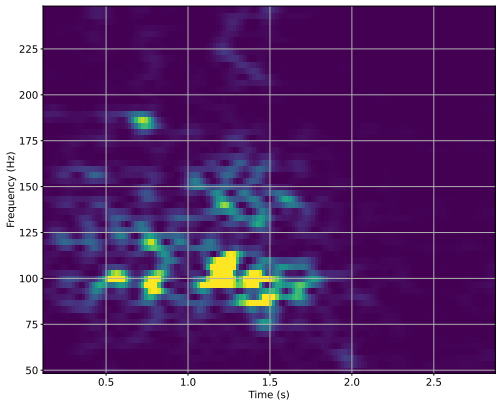

(b) Spectrogram

Figure 8.3: The acceleration response of sensor 17 at the Haringvlietbrug to a passage which belongs to load case II.

In the model, one way to obtain a wide-band spectrum was by implementing three moving masses with different axle distances: two axles were placed close to each other creating a modulated signal by the time delay between these axles and the axle distance to the third mass was large enough that it was not influenced by the other masses ($\theta_2 = 0.1$ and $\theta_3 = 0.102$, the other parameters were set to their default values). This way, the closely-spaced axles induced other frequencies than the third axle. This resulted in a wide-band spectrum as visible in Figure 8.4. However, there were more configurations with different axle distances between the moving masses possible for obtaining wide-band spectra.

Coupling these findings to the Haringvlietbrug recordings, two potential situations for the wide-band frequency spectra to occur were found: case II passages could occur when a vehicle with a specific axle configuration passes or when multiple vehicles drive close to each other.

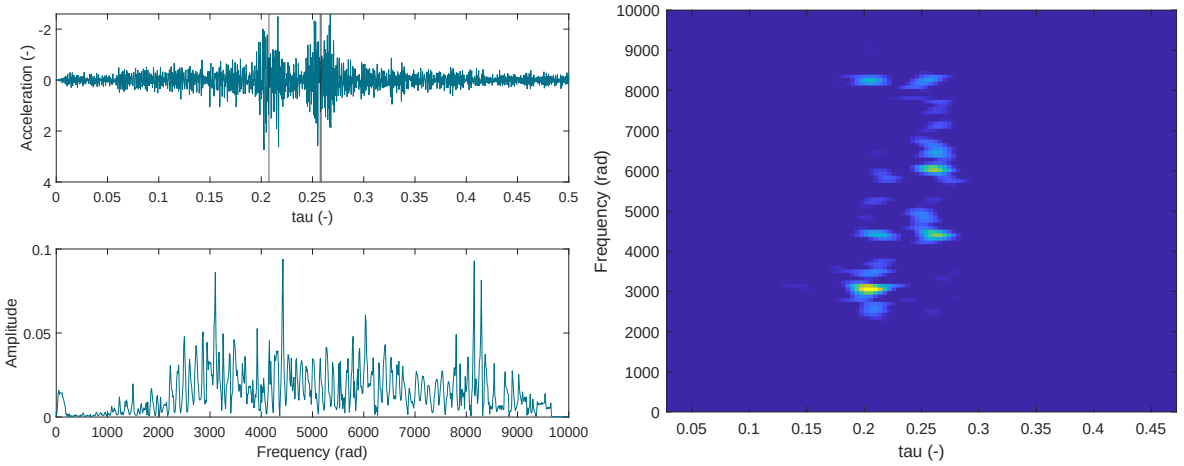

(a) Acceleration response (the vertical lines indicate the time a moving mass crosses ξ_m) and its Fourier spectrum

(b) Spectrogram

Figure 8.4: The acceleration response of the model at ξ_m simulating load case II.

8.3. Case III: semi-trailer trucks

Case III and case IV are about two vehicle categories: semi-trailer trucks and passenger cars respectively. The classification of the vehicles was done based on the acceleration data in the time domain. Assuming a vehicle velocity of 50 km/h, the time between the peaks was recalculated to axle distances. Comparing these to the approximate axles distances of semi-trailer trucks (Figure 8.5), the passages shown in Figure 8.6 and Figure 8.8 are likely to belong to a semi-trailer truck.

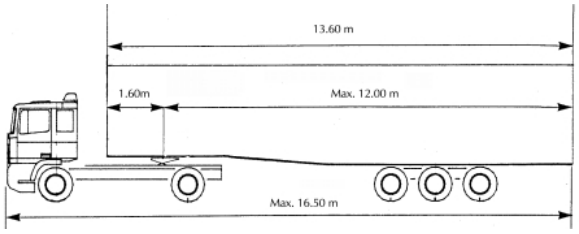

Figure 8.5: The maximal dimensions of a semi-trailer truck in the Netherlands (source: Evofenedex).

The passage shown in Figure 8.6 is a passage whose characteristics in the frequency domain were found frequently in the Haringvlietbrug measurements. It is, however, important to note that this passage is just one example of a semi-trailer truck passage: the variance in frequency response of passages also classified as semi-trailer trucks was large. This was to be expected as also large differences exist between different semi-trailer trucks (for example dimensions, amount of wheels and truckload). Nevertheless, the response shown in Figure 8.6 was observed often and therefore selected to investigate its sources of variability.

The Fourier spectrum is characterised by four high-energy frequency bands: located around 70, 90, 130 and 200 Hz. These are frequencies which often reoccur in the acceleration response of the Haringvlietbrug. The spectrogram shows that the dominant frequency and amplitude is different for each axle: especially the axles of the trailer show an increased response amplitude likely to be caused by a heavy truckload.

Also the variance of the semi-trailer truck case was looked into using the semi-analytical model. Five moving masses, simulating the five wheels as depicted in Figure 8.5, were placed on the beam ($\theta_2 = 0.1$, $\theta_3 = 0.24$, $\theta_4 = 0.246$ and $\theta_5 = 0.252$). The masses belonging to the trailer were increased to model the heavy truckload. This resulted in the response shown in Figure 8.7. Recall that the amplitudes and shapes of the measured and modelled response cannot be directly compared to each other. Yet, the model is able to describe the variance as seen in the semi-trailer truck passage quite accurately. As seen in the response of the Haringvlietbrug, multiple high-energy frequency bands appear in the Fourier spectrum of the acceleration response. In addition, the spectrogram also shows a significant variation in response for each moving mass.

Not all passages labelled as semi-trailer truck passages had a frequency spectrum looking like the one

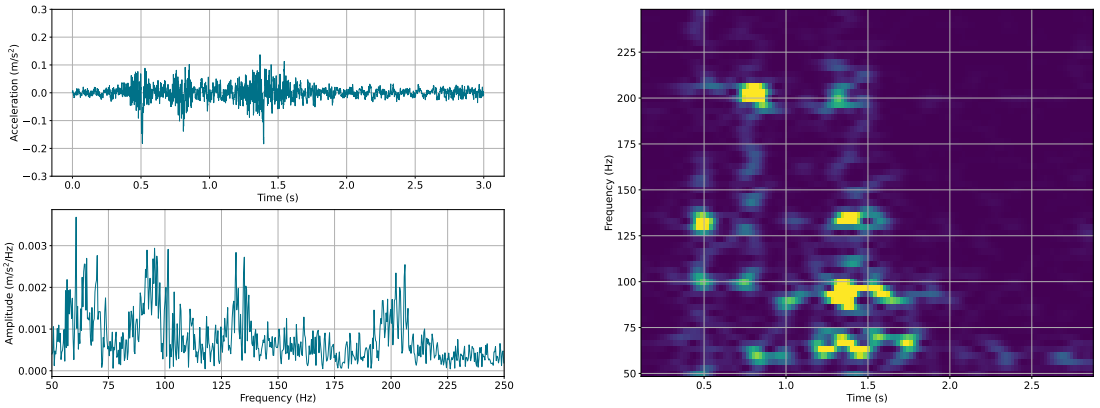

(a) Acceleration response and its Fourier spectrum

(b) Spectrogram

Figure 8.6: The acceleration response of sensor 17 at the Haringvlietbrug to a passage which belongs to load case III.

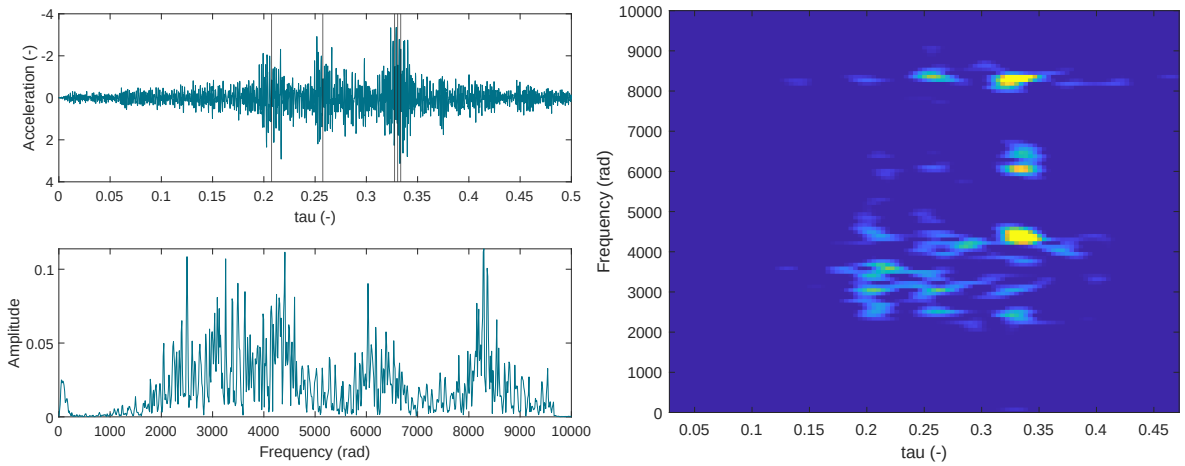

(a) Acceleration response (the vertical lines indicate the time a moving mass crosses ξ_m) and its Fourier spectrum

(b) Spectrogram

Figure 8.7: The acceleration response of the model at ξ_m simulating load case III.

shown in Figure 8.6. Figure 8.8 shows one example of a passage looking similar to the former passage in the time domain. In the frequency domain, however, the differences are large. The spectrogram of Figure 8.8b is characterised by similar frequency magnitude for each axle whereas the spectrogram in Figure 8.6b showed a clear difference in magnitude between the truck and trailer axles. This difference is likely caused by the difference in truckload: a loaded versus an empty trailer (keep here in mind that each spectrograms is normalised). In addition, some other frequencies were excited. By changing the parameters of the model, it was aimed to find the source of these difference. The spectrogram in Figure 8.9a was modelled by decreasing the mass of the axles belonging to the trailer and increasing the axle distance between the wheels of the trailer (in this case $\theta_2 = 0.1$, $\theta_3 = 0.24$, $\theta_4 = 0.26$ and $\theta_5 = 0.28$) which changed the amplified frequencies by the time delay between the axles.

The latter model settings were also used to investigate the effect of the velocity. Changing the velocity of exactly the same passing truck as in the former analysis illustrates the high sensitivity of the model to its parameters. The result in shown in Figure 8.9b. When comparing the spectrograms in Figure 8.9, it can be seen that the increased velocity resulted in a shift in dominant frequencies and their relative magnitudes in the response of the beam. The velocity was increased by 25% which is equivalent to an increase in velocity from 50 to 62.5 km/h. The shifts in the spectrogram were mainly caused due to the changing time delay

between the point loads.

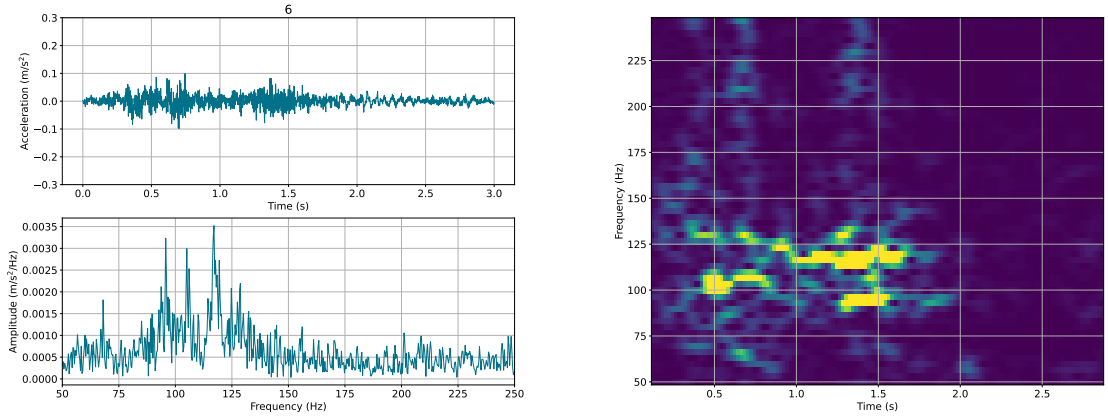

(a) Acceleration response and its Fourier spectrum

(b) Spectrogram

Figure 8.8: The acceleration response of sensor 17 at the Haringvlietbrug to another passage which belongs to load case III.

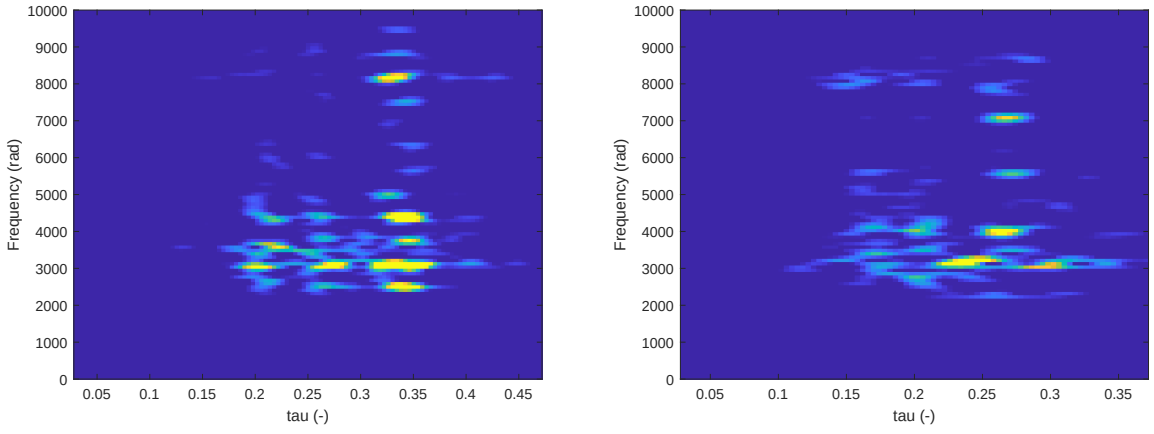

(a) $\alpha = 2$

(b) $\alpha = 2.5$

Figure 8.9: Spectrograms of the acceleration response of the model at ξ_m simulating load case III with two different vehicle velocities.

8.4. Case IV: passenger cars

A passage was classified as passenger car passage if two peaks with a mutual distance between 0.15 and 0.4 seconds were present in the time domain of the acceleration response (equivalent to an axle distance of about 2 to 5 m assuming a velocity of 50 km/h). Data analysis showed that a lot of the noticed passenger car passages in the Haringvlietbrug measurements had a too low signal-to-noise ratio to meet the set threshold value in the sample selection algorithm. The passenger car passages which did meet the threshold showed a large variance in both the time and frequency domain. This is illustrated in Figure 8.10 in which three passenger car passages are shown all with high concentrations of energy at different frequencies. Unlike the semi-trailer truck case in which a characteristic passage could be appointed, no characteristic patterns were found in case IV.

With the model, the aim was again to find the important sources of the large variation in case of passenger cars. The only model parameters capable of causing shifts in the frequency response were the unevenness and the time delay between multiple axles. Assuming only one vehicle was present at the bridge segment of the sensor during the passage, it is unlikely that the time delay caused the frequency shift since the time

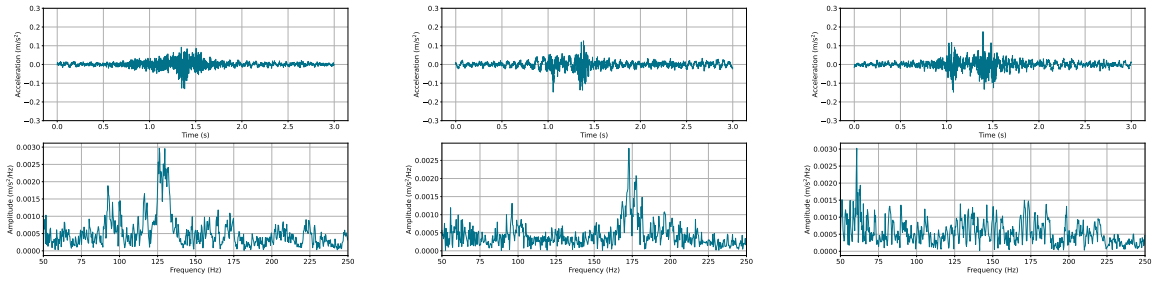

(a) Passage 9 (b) Passage 27 (c) Passage 63

Figure 8.10: The acceleration response and its Fourier spectrum of sensor 17 at the Haringvlietbrug to passages which belong to load case IV.

delay between the axles of a passenger car is too large to significantly influence the load spectrum according to the model. Hence, the shifts should be caused by the unevenness based on the model parameters. This was modelled by increasing the amplitude of a group of unevenness frequency components simulating that the pavement of the road contained a high-energy frequency band. The group of dominant frequency components is clearly visible in Figure 8.11 around 6000 rad. When decreasing the velocity of the moving mass by 25% (which is equivalent to a decrease in velocity from 50 to 37.5 km/h) the group of dominant frequencies not only shifted, it also increased in amplitude. This is another example of the importance of the vehicle velocity as source for variability in the dynamic response of the bridge deck.

The unevenness is a powerful tool to simulate all the observed variability in the response spectra of the Haringvlietbrug as the amplitude of the separate frequency components can be adjusted making it theoretically possible to manually exactly reproduce each possible spectrum. However, the question was raised whether it is realistic to explain all variability in the measurements with the unevenness; it is unlikely that this is the only source of variability in case of passenger cars and other kind of passages. It cannot be excluded that other variabilities, which were not modelled, also play a role in the variability of the dynamic response of the bridge deck of the Haringvlietbrug.

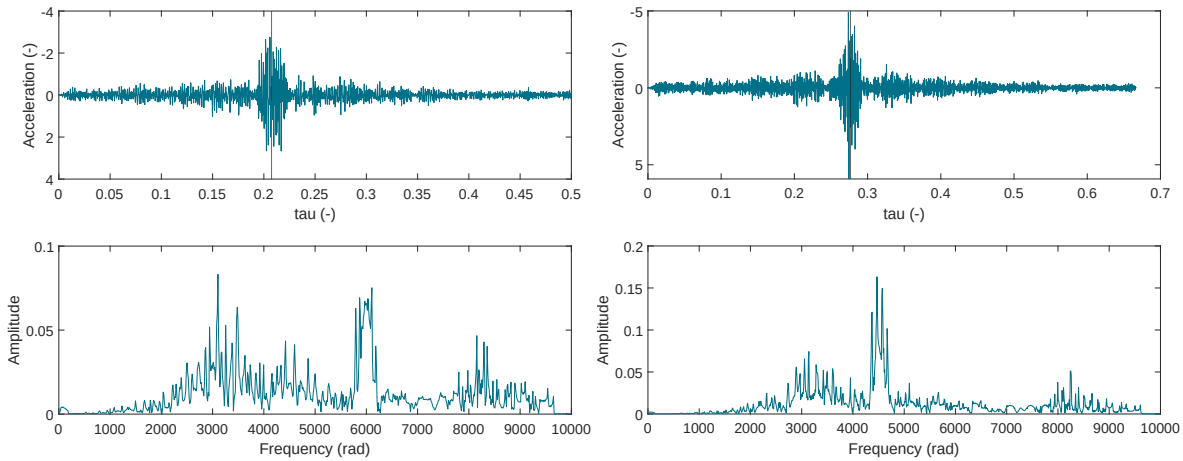

(a) $\alpha = 2$ (b) $\alpha = 1.5$

Figure 8.11: The acceleration response of the beam at ξ_m and its Fourier spectrum and the effect of changes in the unevenness amplitude amplifier and the velocity. The vertical line in the time domain is when the moving mass passes ξ_m.

8.5. Conclusion

This chapter aimed to improve the understanding of the large variability in the Haringvlietbrug response if one compares different vehicle passages. This was done by investigating four characteristic load cases with

the built semi-analytical model. Finding the right model parameters to simulate the recordings revealed potential sources of this variability. In the model, the main sources for the varying beam response were the unevenness and frequency amplification related to the time delay between axles. These two parameters combined with a changing velocity of the moving masses increased the variability significantly. With these three parameters, a large part of the variability in the Haringvlietbrug recordings could be explained. It is likely that these parameters play an important role in the dynamic response of the Haringvlietbrug. Changing vehicle characteristics and different unevenness components increased the variability even more. However, it is important to realise that the above conclusions are not proven; they are hypotheses for the source of variation but more research is needed to confirm the hypotheses. In addition, it is likely that there are more sources of the variability which were not included in the model.

9

Discussion, Conclusions and Recommendations

Literature showed that most currently existing vibration-based structural health monitoring (SHM) techniques focus on fundamental modes of the structure. Fundamental modes, however, are not or hardly affected by small damages in the structure. In vibration-based SHM, a shift in eigenfrequencies of the structure indicates potential damage. This research focused on applying SHM to local modes of vibration of the Haringvlietbrug with the idea that also small-scale faults such as weld cracks could be detected automatically. This brought new challenges along: when considering local modes of vibration, the influence of environmental and operational variabilities (EOV) on the eigenfrequencies of the structure was often larger than the influence of small damage. Hence, the EOVs should be filtered out of the recorded acceleration data. The goal of the research was, therefore, defined as:

To investigate the applicability of similarity filtering on steel bridge deck structures under the influence of EOVs and to improve the understanding of the effect of vehicles on local bridge vibrations for the application of vibration-based SHM using local modes.

This chapter is built up as follows. Section 9.1 summarises the points of discussion and conclusions of similarity filtering given in Chapter 5 and Section 9.2 of the eigensystem realisation algorithm as explained in Chapter 6. In Section 9.3, the semi-analytical model for traffic-induced vibrations and its results, presented in Chapter 7 and Chapter 8, are discussed and conclusions based on the model are drawn. Lastly, Section 9.4 contains numerous recommendations for further research.

9.1. Similarity Filtering

The first goal of this research was to investigate the applicability of similarity filtering (SF) on steel bridge deck structures under the influence of EOVs. SF was applied to the data set of the Haringvlietbrug to investigate its effectiveness in removing operational variabilities from the signals, as it had been shown to be useful in previous research. First, suitable samples were extracted from the data. Various sampling approaches were investigated but, eventually, the samples only consisting of the vibrations after a vehicle had left the bridge segment were selected. SF was based on the convolution theorem with the idea to convolve a certain amount of samples within a 15-minute measurement (to minimise environmental variabilities) with each other to amplify similarities and damp differences between the samples. This way, consistent modal vibrations were supposed to remain in the signals while variabilities were cancelled out. After this operation, a frequency spectrum containing only one or two peaks should remain whose frequencies were subsequently used as damage-sensitive features for SHM.

Discussion The quality of the resulting features was judged based on three criteria. Firstly, it was expected that the spectra of the measurements were smooth and consistent after applying SF. This was not the case as the spectra still consisted of multiple peaks and noise and the frequency of the peaks was highly sensitive to the similarity filter coefficients. Secondly, batches of measurements with highly similar environmental

conditions were composed by the measurement database. It was expected that the results of SF were similar for the measurements within a batch but many outliers were present in the resulting features. Lastly, previous research showed that the features have a strong correlation with the temperature and should be normalised with respect to temperature before being useful for damage detection. However, the resulting features from SF had no or a weak correlation with temperature.

The performance of SF in this research debunks the conclusions made by earlier research in which the effectiveness of SF was better (De Bruijn, 2019; Milosevic, 2018). They were able to extract features which seemed damage-sensitive and temperature-dependent but the current research found that their conclusions were based on crooked data. Instead of consistent behaviour between samples, SF converged to spikes, visible in the Fourier spectra of the accelerometer data (Figure 4.2) and caused by aliasing of the sensors.

Three reasons were listed for the bad performance of SF. Firstly, the method was not robust due to its high sensitivity to separate input samples and filter coefficients: a single sample or filter coefficient significantly influenced the results. Secondly, as one or two features per measurement were extracted, it is likely some closely-spaced modes were missed which could have contributed the inconsistency of the results. The third reason is that the variability of the response of the Haringvlietbrug bridge deck to each vehicle passage might be too great for SF to converge to similar behaviour in the samples. The latter hypothesis was supported by the data analysis as Figure 4.9 showed a large variance in bridge response when comparing different vehicle passages.

Conclusion So the results of SF failed on all three judgement criteria which clearly answered the first research question *To what extent is similarity filtering an effective method to remove operational variabilities from the signals at the Haringvlietbrug?*. Based on the data set of the Haringvlietbrug, SF is not an effective method to remove operational variabilities considering frequencies between 50 and 250 Hz.

One of the potential reasons for the bad performance of SF was that the system is effectively different for each vehicle passage and therefore also the dynamic response does not show clear similarities. To learn more about the bridge response and to investigate this hypothesis, the second part of the research goal was about improving the understanding of the effect of vehicles on local bridge vibrations for the application of SHM. Two approaches were considered: applying eigensystem realisation algorithm (ERA) and building a semi-analytical model.

9.2. Eigensystem Realisation Algorithm

The eigensystem realisation algorithm (ERA) is an operational modal analysis (OMA) and output-only system identification technique. The goal of using ERA on the Haringvlietbrug acceleration data was to find patterns in the eigenfrequencies of modes and to identify and compare consistent mode shapes to better understand the vibrations of the bridge deck. Although ERA was able to find consistent modes in the data, these consistent modes had a large variance in shape and eigenfrequency.

Discussion It turned out that there were numerous potential reasons for the large variance in the results of ERA. ERA had two key assumptions that were not perfectly met: the impulse response and the linear time invariant (LTI) assumptions. Furthermore, the spatial density of the accelerometers on the Haringvlietbrug was potentially too low to separate closely-spaced modes. In addition, the uncertainty of the results was increased because the duration of the samples was relatively short and some had a low signal-to-noise ratio which made it also difficult to estimate the right ERA parameters.

Conclusion ERA was able to identify two consistent modes: the first mode between 62 and 71 Hz and the second mode between 89 and 102 Hz. However, the large variance within the results of ERA and the potential issues make the results too uncertain to be useful when considering higher-order modes. Therefore, applying ERA on the data set of the Haringvlietbrug did not provide suitable answers to the research questions.

9.3. Semi-Analytical Model

A semi-analytical model was built to simulate some important sources of the variability as found in the acceleration recordings of the Haringvlietbrug. The goal of the model was to investigate the sensitivity of the response of the bridge deck to variations of input parameters. The conclusions drawn based on the model

should be seen as hypotheses about which parameters are the most influential and interesting to investigate further with experimental studies.

Discussion The first part of the discussion of the semi-analytical model is about the derivation and solving of the model, the second part examines the results of the model and the last part the influence of the most important model parameters.

The first point of discussion is about the composition of the model and its limitations (a drawing of the model was shown in Figure 7.1). A segment of the Haringvlietbrug is modelled as an Euler-Bernoulli beam with local resonators to make the local modes dominant compared to global modes. Outside these resonators, the beam is supported by a viscous continuous support. The distributed damping simulates the structural damping of the Haringvlietbrug and prevents the reflection of waves against the boundaries of the model. The model is dimensionless in order to reduce the number of input parameters and make the results generally applicable. The composition of the model allows for investigating the variability of local vibrations, generated by a passing vehicle interacting with the structure. An important limitation is that the model is 2D; the effect of 3D wave interference and the influence of axles next to each other or on a different bridge segment were not investigated. The axles of vehicles are modelled with a single degree-of-freedom (SDOF) mass-spring system. The vehicle model implements basic vehicle characteristics and induces vibrations into the interactive system of the beam and vehicle enabling parametric studies.

The second issue is about the choice of default fixed model parameters. The model parameters were set based on a number of assumptions. The eigenfrequency of the local resonators was chosen to be approximately 100 times that of the vehicle and these eigenfrequencies were the boundaries of the unevenness frequency components as a result of which all modes of interest were excited. The locations of the resonators were chosen in such a way that modes that excited the resonators could be distinguished from modes that most dominantly excited the middle beam. By this means, the acceleration response obtained was similar to the acceleration response observed from the measurements of the bridge in the time domain. In the frequency domain, the influence of the fixed parameters was large but changing them would not change the conclusions drawn based on the model according to the robustness analysis in Appendix Section A.5.

Thirdly, it was noticed that the model had difficulties converging for certain combinations of input parameters. During the analyses in this thesis, the issue was solved by including fewer modes in the time-history analysis (for example by decreasing N from 33 to 30), which slightly influenced the high-frequency components of the response of the beam. The vehicle velocities for which convergence issues resulted could not directly be related to the maximum response of the beam as plotted in Figure 7.11.

The model results were analysed. Both frequency and time domain calculations were performed. It was concluded that the three most important model parameters are the time delay between axles, the unevenness and the velocity. The time delay altered the spectrum of the loads: some frequencies were amplified while others were damped. This could prevent certain modes of the bridge deck to be excited. Vibration-based SHM uses the shifts of eigenfrequencies to detect damage. It is therefore important to know how the response signal of the monitored bridge is altered by its loading. Processing the signals requires information on both the axle distances of the passing vehicles and their velocity as these parameters determine the modulation of the signal. With the acceleration data, it is possible to estimate these parameters roughly but high accuracy is necessary as a small shift of the parameters can have a large impact on the response of the bridge deck according to the model.

In literature (e.g. Fuchs & Bokelmann, 2018; Milne *et al.*, 2017), the time delay effect was investigated extensively for trains as they consist of a lot of vehicles with the same axle configuration, making the amplified frequencies (or train load frequencies) dominant in the response of the structures and soil. The effect has also been studied for semi-trailer trucks, though to a lesser extent. Brady & O'Brien (2006), Cantieni (1992) and Meyer (2022) saw the effect of time delay between the axles of vehicles in their results. Considering fundamental bridge frequencies, Meyer (2022) concluded that the distance between axle groups was more influential than the distance between the axles within an axle group as these loading frequencies were closer to the dominant eigenfrequencies of the structure. However, the author acknowledged the complexity of this effect due to the presence of the harmonics of the amplified frequency, which also played a dominant role in the semi-analytical model. This thesis concluded that the effect was most influential when considering closely-spaced axles (axles within an axle group). The different conclusion might be explained by the fact that the current research focused on local bridge vibrations instead of fundamental modes.

In the semi-analytical model, the unevenness described the roughness and irregularities of both the pave-

ment and the tyre in the model and determined to a large extent which frequencies were excited in the system and thus the shape of the response of the system. The dominant role of unevenness is supported by literature. For example, Gao *et al.* (2015) indicated the roughness as the most important parameter of their numerical model, influencing the amplitude of the response of the bridge linearly. Not much research has been performed on the influence of a single dominant spatial unevenness frequency on the dynamic response of the bridge deck. Camara *et al.* (2017) did investigate this effect on the response of the vehicle and the adjacent sidewalk in an extensive numerical model. They concluded that the acceleration response of the vehicle was directly influenced by a dominant unevenness component (especially when the frequency was close to an eigenfrequency of the vehicle). The dynamic response of the sidewalk was less sensitive which was probably caused by the fact that the vehicles only indirectly influenced the response of the sidewalks as the vibrations were transferred from the bridge deck by transverse beams. Comparing the results of Camara *et al.* (2017) to this research, the challenges of vibration-based SHM on a small scale are highlighted as the influence of the unevenness on larger structural elements is smaller.

Next, four characteristic passages were selected from the Haringvlietbrug measurements which were simulated by the model in Chapter 8. The model successfully reproduced most of the behaviour of the characteristic cases and showed that the three dominant parameters were able to induce large variability in the response of the beam. Modifying the unevenness parameters allowed to reproduce the variability of the measurements in the frequency domain but not always in the time domain as the influence of the unevenness on the bridge response in the time domain was often limited. For this, adapting the axle configuration of the vehicles was more effective.

In addition, it could not be excluded that other, non-modelled, factors also contributed to the variability in the bridge response. An example is that only longitudinal wave propagation was investigated since the model is 2D; the effect of traffic on the other segments of the bridge causing vibrations could also be of significance. The importance of the pre-existing vibrations in bridges was highlighted by Rattigan *et al.* (2009): depending on the distance between the vehicles, their velocity and the condition of the road, the amplitude of the response of the beam increased up to 30% compared to the presence of one vehicle.

Lastly, data analysis showed a pattern: a large part of the passages of mostly semi-trailer trucks had high-energy frequency bands around 70, 90 and 130 Hz. This is in line with the (uncertain) results of ERA which found consistent modes between 62 and 71 Hz and 89 and 102 Hz. In addition, also the frequency domain decomposition (FDD) suggested the presence of eigenfrequencies around 60 and 95 Hz in the preliminary data analysis in Chapter 4. Hence, it is likely that these peaks belong to modes of the bridge deck which are triggered by a large part of the vehicles. This would make passages in which these frequencies are excited interesting for SHM.

Conclusion The answer to the second research question *How is the local dynamic response of the bridge deck of the Haringvlietbrug influenced by operational variabilities?* was found in Chapter 4 and Chapter 8. It became clear that vehicle passages are dominantly present in the high-frequency dynamic response of the bridge deck. The amplitude as well as the dominant frequencies and shape of the Fourier spectrum of the acceleration response of the Haringvlietbrug were different for each passage. Nevertheless, relatively consistent behaviour was also present in the dynamic response to passages as a substantial part of the passing vehicles excited modes around 70, 90 and 130 Hz. The responses of different sensors to the same passage showed a strong correlation for both longitudinally- and transversely-placed sensors (Chapter 4). This means that the exact position of the vehicle relative to the sensor is not a source of variability.

The third research question was *What are the causes of the differences in the dynamic response of the Haringvlietbrug to different vehicle passages?*. This question was answered by the parametric studies in Chapter 7 and the simulation of load cases in Chapter 8. The variable model parameters were sorted from most to least influential on the acceleration response of the beam based on the results of the model. Most influential is the time delay between multiple axles: the time delay modulates the signals of the loads of the wheels subjected to the bridge deck. As a result, some frequencies of the load are amplified while others are damped. The effect is dominant for closely-spaced axles (for example the axles of a trailer). The unevenness, also a highly influential parameter, described the point contact between the wheel and the bridge deck and included road and tyre roughness and irregularities. The frequency response energy varies with the frequencies that are excited by the unevenness and vehicle velocity. Both the amplitudes and the shape of the Fourier spectrum of the response of the beam are influenced by this parameter. The velocity of the vehicle is an important source of the variability in the spectra when it is considered together with time delay or unevenness. Less

influential are the mass and suspension stiffness of the vehicle. According to the model, these parameters only influence the amplitude of the Fourier spectrum of the response of the beam and not the shape of the spectrum. It is difficult to indicate what role these parameters actually play at the Haringvlietbrug. Additional information is needed to say more about that. Furthermore, it is likely that there are factors influencing the dynamic response of the bridge which were not included in the model.

The last research question was *How can the newly obtained insights be used for the sake of vibration-based structural health monitoring?*. Learning more about the sensitivity of the bridge deck response to the parameters of passing vehicles allows to better define a strategy how to deal with such variability. An option would be to filter out the operational variabilities of the Haringvlietbrug recordings to make them useful for damage detection for SHM. However, it was found that, according to the model, the bridge deck is highly sensitive to three parameters: the axle distance, unevenness and velocity. This high sensitivity makes it difficult to mitigate the effects of these parameters. Moreover, learning more about these parameters would require a more extensive measurement campaign.

Altogether, this research was yet another confirmation of the complexity of using local vibrations for vibration-based SHM. The literature study indicated this already as Alamdari (2015) wrote about the complexity of exciting higher-order modes consequently and Rainieri & Magalhaes (2017) concluded that the influence of EOVs and small-scale damage on the eigenfrequencies of the structure were of the same magnitude. Amongst others, De Bruijn (2019) and Greijmans (2020) also experienced difficulties separating the modal behaviour of the structure from EOVs. According to the model, this is because the sensitivity of the bridge deck to the characteristics of the passing vehicles is high. An improved technique is required which is able to extract consistent modal behaviour of the structure before being able to use higher-order modes for SHM. But, given the high sensitivity of the dynamic response of the bridge deck of the Haringvlietbrug to the passing vehicles, this will be a challenge.

9.4. Recommendations

Multiple recommendations for further research were made based on the above discussion and conclusions, which are divided into recommendations on SF, modal analysis and the semi-analytical model.

Similarity filtering It was concluded that SF is not an effective method to remove operational variabilities from the signal for this system. One of the reasons for this was the large variability in the dynamic response of each vehicle passage. However, a relatively large part of the passages contained high-energy frequency bands around 70, 90 and 130 Hz. This suggests that these concentrations of energy belong to modes which were frequently excited. Only selecting these passages might increase the performance of SF as it can better converge to consistent modal behaviour.

Modal analysis The spatial density of the accelerometers was too low to reliably perform modal analysis and ERA was not a perfectly suitable method for the current application. Improvements of the modal analysis would help to better understand the dynamic response of the Haringvlietbrug and the consistency of excited modes. Should someone want to further explore these research objectives, it is recommended to equip a section of the bridge with a high spatial density of accelerometers in a new measurement campaign and to use a more suitable modal analysis technique.

Semi-analytical model The first step for further research would be the verification of the results of this research, particularly the influence of the model parameters, by comparing the results with test vehicles measurements. The effect of the vehicle mass and suspension stiffness can be tested by comparing the bridge response to a truck with a loaded versus an empty trailer and an adapted suspension.

Next, the influence of time delay between multiple wheels on the Haringvlietbrug should be investigated. Two questions need to be answered: is the sensitivity of the dynamic response of the bridge to the time delay as large as in the model and what are the minimum and maximum time delay values for which the effect is significant? To answer these questions properly, multiple test vehicles with different axle configurations are needed.

The unevenness is more difficult to validate because it comprises both pavement and wheel characteristics and irregularities. The test vehicles could be equipped with a distance measurement instrument, an accelerometer and a laser making it possible to map the actual pavement roughness of the Haringvlietbrug

(Islam *et al.*, 2014). A PSD can be applied after processing the data to find dominant unevenness frequencies (Wambold, 1979) which can help explain the acceleration spectra of the response of the bridge. Camara *et al.* (2017) is an example of research in which the roughness of a bridge was measured to use as input for the unevenness of the model. This test equipment would also enable research into the extent of the influence of the exact transverse location of the vehicle on the bridge on the response of the bridge deck as the roughness of the pavement might be slightly different. The effect of irregularities can be investigated by for example equipping a test vehicle with an irregular tyre and comparing the results to the case I passages with a clear Doppler effect (Chapter 8).

By running the above experiments with different vehicle velocities, also the influence of the velocity on the dynamic response of the Haringvlietbrug can be validated. This research was not able to fully explain the effect of the velocity on the amplitude of the response of the beam during the parametric studies of the model. Additional research is required to learn more about how the velocity influences the response and what causes the critical velocities to exist.

Assuming that the importance of the time delay between the vehicle axles is verified, data processing towards damage detection requires information on axle configuration and velocity in order to predict how the signal is modulated. Estimations based on peaks in the acceleration response are not accurate enough so additional sensors providing information about the vehicles are necessary. An option is to add pneumatic tube traffic counters to the sensor set-up in the next measurement campaign. The traffic counters are able to gather information about the passing vehicles (velocity, amount of axles, distance between axles) with good accuracy. If the calculated amplified frequencies match the measured spectrum, the shape of the spectrum is explained. It would be interesting to analyse and compare the response of the Haringvlietbrug to passages labelled by the traffic counter as similar. If the response of the bridge deck is similar for these cases, the performance of damage detection algorithms might be improved when only considering these passages as the behaviour of the bridge is more consistent.

The test vehicles can also be used to partly calibrate the current semi-analytical model which would increase the reliability of the results. Full calibration is not possible because the model is a simplified model developed to capture some specific aspects of the far more complex behaviour of the actual Haringvlietbrug. The measured responses of different test vehicles and the bridge can be used to calibrate the model by adjusting the settings of the model to approach for example the peak acceleration and signal-to-noise ratio of the measurements. It is advised to use multiple different vehicles (from passenger cars to semi-trailer trucks) whose characteristics and velocities are known. During the test runs, the presence of other vehicles on the bridge should be prevented as much as possible.

The current semi-analytical model capabilities are limited and could be extended. The current semi-analytical model could be extended to include more parameters, like vehicle acceleration, or the measured pavement roughness could be used to better define the unevenness. Additionally, the model of the vehicle could be improved by introducing the more realistic, computationally-expensive, half-vehicle model with wheels modelled as disks instead of point contacts. These extensions might make both the effects of time delay and unevenness more realistic. The second option is to build a 3D finite element (FE) model. With such a model, it would be possible to investigate the influence of interference of multiple vehicles on the results. It can be investigated to what extent a vehicle in the other driving direction or at the parallel road of the Haringvlietbrug influences the acceleration recordings. With the current model, only longitudinal wave propagation was investigated while transverse wave propagation most likely will be of influence as well. It should be noted that the FE model is only of added value if it is properly calibrated and validated, which is difficult and would require a lot of bridge data.

It is uncertain if improving the models would enable follow-up research to successfully apply vibration-based SHM on local modes of a bridge deck as the current research concluded that the bridge deck of the Haringvlietbrug is highly sensitive to the characteristics of passing vehicles. Further improving the understanding of the nature of the variability in the dynamic response of the bridge deck would help process the measurement data from the accelerometers but it is unlikely that all variability can fully be explained and normalised with high reliability. The knowledge of the sources might be insufficient to normalise the acceleration data with respect to the operational variabilities.

A data-driven approach that does not need a full physical explanation might be a solution. Optimally, an algorithm is developed which is able to extract only the dynamic properties of the bridge deck from the measurements (and is hardly influenced by EOVs). Many attempts were already made to do this but algorithms

like active neural networks or the robust principal component analysis are promising. A large advantage of these algorithms is that they are easily applicable to different bridges. The still insufficient performance of such algorithms might be caused by the high sensitivity of bridge decks to operational variabilities as seen in this research. A solution for upcoming research might be to focus only on similar passages to decrease the large variability between the samples. Some passages excite completely different modes than others which means that not all samples contain the same information on the dynamic behaviour of the structure.

Bibliography

Al-Rumaithi, A. 2022. *Eigensystem Realization Algorithm (ERA)*.

Alamdari, M.M. 2015. *Vibration-Based Structural Health Monitoring*. Ph.D. thesis, University of Technology, Sydney.

Alampalli, S. 1998. *Influence of in-service environment on modal parameters*. Tech. rept. Transportation Research and Development Bureau.

Bao, Yuequan, & Li, Hui. 2021. Machine learning paradigm for structural health monitoring. *Structural Health Monitoring*, **20**(4), 1353–1372.

Brady, Sean P., & O'Brien, Eugene J. 2006. Effect of Vehicle Velocity on the Dynamic Amplification of Two Vehicles Crossing a Simply Supported Bridge. *Journal of Bridge Engineering*, **11**(2), 250–256.

Brady, Sean P, O'Brien, Eugene J, & Žnidarič, Aleš. 2006. Effect of Vehicle Velocity on the Dynamic Amplification of a Vehicle Crossing a Simply Supported Bridge.

Brewick, P. T., & Smyth, A. W. 2013. An investigation of the effects of traffic induced local dynamics on global damping estimates using operational modal analysis. *Mechanical Systems and Signal Processing*, **41**(1-2), 433–453.

Brewick, P. T., & Smyth, A. W. 2014. On the application of blind source separation for damping estimation of bridges under traffic loading. *Journal of Sound and Vibration*, **333**(26), 7333–7351.

Brincker, R., & Ventura, C. 2015. *Introduction to Operational Modal Analysis*. John Wiley & Sons, Ltd.

Brunton, S. 2018. *Data-Driven Control: Eigensystem Realization Algorithm*.

Caicedo, J. M. 2011. Practical guidelines for the natural excitation technique (NExT) and the eigensystem realization algorithm (ERA) for modal identification using ambient vibration. *Experimental Techniques*, **35**(4), 52–58.

Camara, Alfredo, Vázquez, V. F., Ruiz-Teran, A. M., & Paje, S. E. 2017. Influence of the pavement surface on the vibrations induced by heavy traffic in road bridges. *Canadian Journal of Civil Engineering*, **44**(12), 1099–1111.

Cantieni, Reto. 1992. *Dynamic Behavior of Highway Bridges Under the Passage of Heavy Vehicles*. Tech. rept.

Cross, E. J., Koo, K. Y., Brownjohn, J. M.W., & Worden, K. 2013. Long-term monitoring and data analysis of the Tamar Bridge. *Mechanical Systems and Signal Processing*, **35**(1-2), 16–34.

De Bruijn, Janno. 2019. *Vibration-based Monitoring of the Zwartewaterbrug: a Machine Learning Approach*.

Deraemaeker, A., Reynders, E., De Roeck, G., & Kullaa, J. 2008. Vibration-based structural health monitoring using output-only measurements under changing environment. *Mechanical Systems and Signal Processing*, **22**(1), 34–56.

Farrar, Charles R., Duffey, Thomas A., Cornwell, Phillip J., & Doebling, Scott W. 1999. *Excitation methods for bridge structures*.

Figueiredo, Eloi, Moldovan, Ionut, Santos, Adam, Campos, Pedro, & Costa, João C. W. A. 2019. Finite Element–Based Machine-Learning Approach to Detect Damage in Bridges under Operational and Environmental Variations. *Journal of Bridge Engineering*, **24**(7), 04019061.

Fuchs, Florian, & Bokelmann, Götz. 2018. Equidistant spectral lines in train vibrations. *Seismological Research Letters*, **89**(1), 56–66.

Furtmüller, Thomas, Adam, Christoph, & Veit-Egerer, Robert. 2020. Variable mass loading effect on the long-term ambient response of a freeway bridge. *Structure and Infrastructure Engineering*.

Gao, Qing fei, Wang, Zong lin, Liu, Chen guang, Li, Jun, Jia, Hong yu, & Zhong, Jun fei. 2015. Dynamic responses of a three-span continuous girder bridge with variable cross-section based on vehicle–bridge coupled vibration analysis. *IES Journal Part A: Civil and Structural Engineering*, **8**(2), 121–130.

Gardner, Sérgio Paul, & Barthorpe, Robert J. 2019. On current trends in forward model-driven SHM. *Pages 2152–2160 of: Structural Health Monitoring 2019: Enabling Intelligent Life-Cycle Health Management for Industry Internet of Things (IIOT) - Proceedings of the 12th International Workshop on Structural Health Monitoring*, vol. 2. DEStech Publications Inc.

Gasparis, Georgios. 2019. *A Benchmark Study on Operational Modal Analysis System Identification Algorithms for Operating Offshore Wind Turbines*. Tech. rept. TU Delft.

Gonzalez, Arturo, & Schmidt, Franziska. 2018. *Effects on bridges of the various vehicle configurations*. Tech. rept.

Greijmans, Marie-Louise. 2020. *Vibration-based damage detection of the Haringvlietbrug: A data-driven approach*.

Hou, Rongrong, & Xia, Yong. 2021. Review on the new development of vibration-based damage identification for civil engineering structures: 2010–2019. *Journal of Sound and Vibration*, **491**(1), 115741.

Huang, D. 2012. Vehicle-Induced Vibration of Steel Deck Arch Bridges and Analytical Methodology. *Journal of Bridge Engineering*, 241–248.

Islam, Shahidul, Buttlar, William G., Aldunate, Roberto G., & Vavrik, William R. 2014. *Measurement of pavement roughness using android-based smartphone application*.

Juang, Jer Nan, & Pappa, Richard S. 1985. An eigensystem realization algorithm for modal parameter identification and model reduction. *Journal of Guidance, Control, and Dynamics*, **8**(5), 620–627.

Karakus, Murat, Cavus, Aydin, & Colakoglu, Mehmet. 2017. Vibration analysis of a tire in ground contact under varied conditions. *Journal of Theoretical and Applied Mechanics (Bulgaria)*, **47**(1), 3–17.

Kim, Chubyoung, Jung, Dae-Sung, Kim, Nam-Sik, & Yoon, Jah-Geol. 1999. *Effect of Vehicle Mass on the Measured Dynamic Characteristics of Bridges from Traffic-Induced Vibration Test*. Tech. rept.

Kortendijk, C N. 2020. *Influence of temperature on natural vibrations of steel bridges*.

Kostić, Branislav, & Gül, Mustafa. 2017. Vibration-Based Damage Detection of Bridges under Varying Temperature Effects Using Time-Series Analysis and Artificial Neural Networks. *Journal of Bridge Engineering*, **22**(10), 04017065.

Ljung, Lennart. 1999. *System identification : theory for the user*. 2nd edn. Upper Saddle River, NJ: Prentice Hall PTR.

Malekloo, Arman, Ozer, Ekin, AlHamaydeh, Mohammad, & Girolami, Mark. 2021. Machine learning and structural health monitoring overview with emerging technology and high-dimensional data source highlights. *Structural Health Monitoring*.

Mathworks. *Time-Frequency Analysis and Continuous Wavelet Transform*.

Meyer, M. 2022. *The Characterization of the Dynamic Interaction between Highway Bridges and Long, Multi-Trailer Heavy Vehicles*. Ph.D. thesis, University of Stellenbosch.

Michaltsos, G T, & Konstantakopoulos, T G. 2000. Dynamic Response of a Bridge With Surface Deck Irregularities. *Journal of Vibrations and Control*, **6**, 667–689.

Milne, D. R.M., Le Pen, L. M., Thompson, D. J., & Powrie, W. 2017. Properties of train load frequencies and their applications. *Journal of Sound and Vibration*, **397**(6), 123–140.

Milosevic, Marko. 2018. *Structural Health Monitoring of the Zwartewaterbrug Bridge*.

Ni, Y. Q., Hua, X. G., Fan, K. Q., & Ko, J. M. 2005. Correlating modal properties with temperature using long-term monitoring data and support vector machine technique. *Engineering Structures*, **27**(12), 1762–1773.

Noel, Adam B., Abdaoui, Abderrazak, Elfouly, Tarek, Ahmed, Mohamed Hossam, Badawy, Ahmed, & Shehata, Mohamed S. 2017. Structural Health Monitoring Using Wireless Sensor Networks: A Comprehensive Survey. *IEEE Communications Surveys and Tutorials*, **19**(3), 1403–1423.

Ostachowicz, Wieslaw, Soman, Rohan, & Malinowski, Pawel. 2019 (5). *Optimization of sensor placement for structural health monitoring: a review*.

Pappa, R., Elliott, K., & Schenk, A. 1992. A consistent-mode indicator for the eigensystem realization algorithm. *Journal of Guidance, Control, and Dynamics*, **16**(5).

Pastor, Miroslav, Binda, Michal, & Harčarik, Tomáš. 2012. Modal Assurance Criterion. *Procedia Engineering*, **48**(1), 543–548.

Peeters, Bart, & De Roeck, Guido. 2000. *One year monitoring of the z24-bridge: environmental influences versus damage events*. Tech. rept. KU Leuven.

Peeters, Bart, Maeck, Johan, & De Roeck, Guido. 2001. Vibration-based damage detection in civil engineering: Excitation sources and temperature effects. *Smart Materials and Structures*, **10**(3), 518–527.

Pisal, Alka Y., & Jangid, R. S. 2016. Vibration control of bridge subjected to multi-axle vehicle using multiple tuned mass friction dampers. *International Journal of Advanced Structural Engineering*, **8**(2), 213–227.

Rainieri, Carlo, & Magalhaes, Filipe. 2017. Challenging aspects in removing the influence of environmental factors on modal parameter estimates. *Pages 2244–2249 of: Procedia Engineering*, vol. 199. Elsevier Ltd.

Rattigan, Paraic H., Gonzalez, Arturo, & OBrien, Eugene J. 2009. Influence of pre-existing vibrations on the dynamic response of medium span bridges. *Canadian Journal of Civil Engineering*, **36**(1), 73–84.

Rishin, V. V., Lyashenko, B. A., Akinin, K. G., & Nadezhdin, G. N. 1973. Temperature dependence of adhesion strength and elasticity of some heat-resistant coatings. *Strength of Materials*, **5**(1), 123–126.

Rytter, Anders. 1993. *Vibrational Based Inspection of Civil Engineering Structures*.

Santos, Adam, Figueiredo, Eloi, Silva, M. F.M., Sales, C. S., & Costa, J. C.W.A. 2016. Machine learning algorithms for damage detection: Kernel-based approaches. *Journal of Sound and Vibration*, **363**(2), 584–599.

Sawant, V. A., Patil, V. A., & Deb, Kousik. 2011. Effect of vehicle-pavement interaction on dynamic response of rigid pavements. *Geomechanics and Geoengineering*, **6**(1), 31–39.

Shafiei, Babak. 2021. Investigating the impact of the velocity of a vehicle with a nonlinear suspension system on the dynamic behavior of a Bernoulli–Euler bridge. *SN Applied Sciences*, **3**(3).

Sheibani, M., & Ghorbani-Tanha, A. K. 2021. Obtaining mass normalized mode shapes of motorway bridges based on the effect of traffic movement. *Structures*, **33**(10), 2253–2263.

Smith, Emma, & Garcia, Hector. 2013. *Wheel Induced Vibrations on Heavy Vehicles*. Tech. rept.

Sohn, Hoon. 2006. Effects of environmental and operational variability on structural health monitoring. *Philosophical Transactions of the Royal Society A: Mathematical, Physical and Engineering Sciences*, **365**(1851), 539–560.

Song, Lizhong, Li, Xiaozhen, Hao, Hong, & Zhang, Xun. 2018. Medium- and High-Frequency Vibration Characteristics of a Box-Girder by the Waveguide Finite Element Method. *International Journal of Structural Stability and Dynamics*, **18**(11).

Subbian, J., Balasubramanian, A., Padmanaban, S., & Amarnath, SKP. 2019. *Investigation of High Frequency Interior Noise due to Tyre-Road Interaction using Experimental and*. Tech. rept. Inter.Noise, Madrid.

Wahab, Magd Abdel, & De Roeck, Guido. 1997. Effect of Temperature on Dynamic System Parameters of a Highway Bridge. *Structural Engineering International: Journal of the International Association for Bridge and Structural Engineering (IABSE)*, **7**(4), 266–270.

Wambold, James C. 1979. The measurement and data analysis used to evaluate highway roughness. *Wear*, **57**(1), 117–125.

Wang, J. F., Lin, C. C., & Chen, B. L. 2003. Vibration suppression for high-speed railway bridges using tuned mass dampers. *International Journal of Solids and Structures*, **40**(2), 465–491.

Xia, Yong, Hao, Hong, Zanardo, Giovanna, & Deeks, Andrew. 2006. Long term vibration monitoring of an RC slab: Temperature and humidity effect. *Engineering Structures*, **28**(3), 441–452.

Yu, Helu, Wang, Bin, Li, Yongle, Zhang, Yankun, & Zhang, Wei. 2018. Road vehicle-bridge interaction considering varied vehicle speed based on convenient combination of simulink and ANSYS. *Shock and Vibration*, **2018**.

Zhang, Xun, Li, Xiaozhen, Wen, Zhipeng, & Zhao, Yu. 2018. Numerical and experimental investigation into the mid- and high-frequency vibration behavior of a concrete box girder bridge induced by high-speed trains. *JVC/Journal of Vibration and Control*, **24**(23), 5597–5609.

Zhou, Guang Dong, & Yi, Ting Hua. 2014. A summary review of correlations between temperatures and vibration properties of long-span bridges. *Mathematical Problems in Engineering*, **2014**.

Zhu, J, Zhang, W, & Wu, M X. 2018. Coupled Dynamic Analysis of the Vehicle-Bridge-Wind-Wave System.

A

Appendices

A.1. Sensor Layout

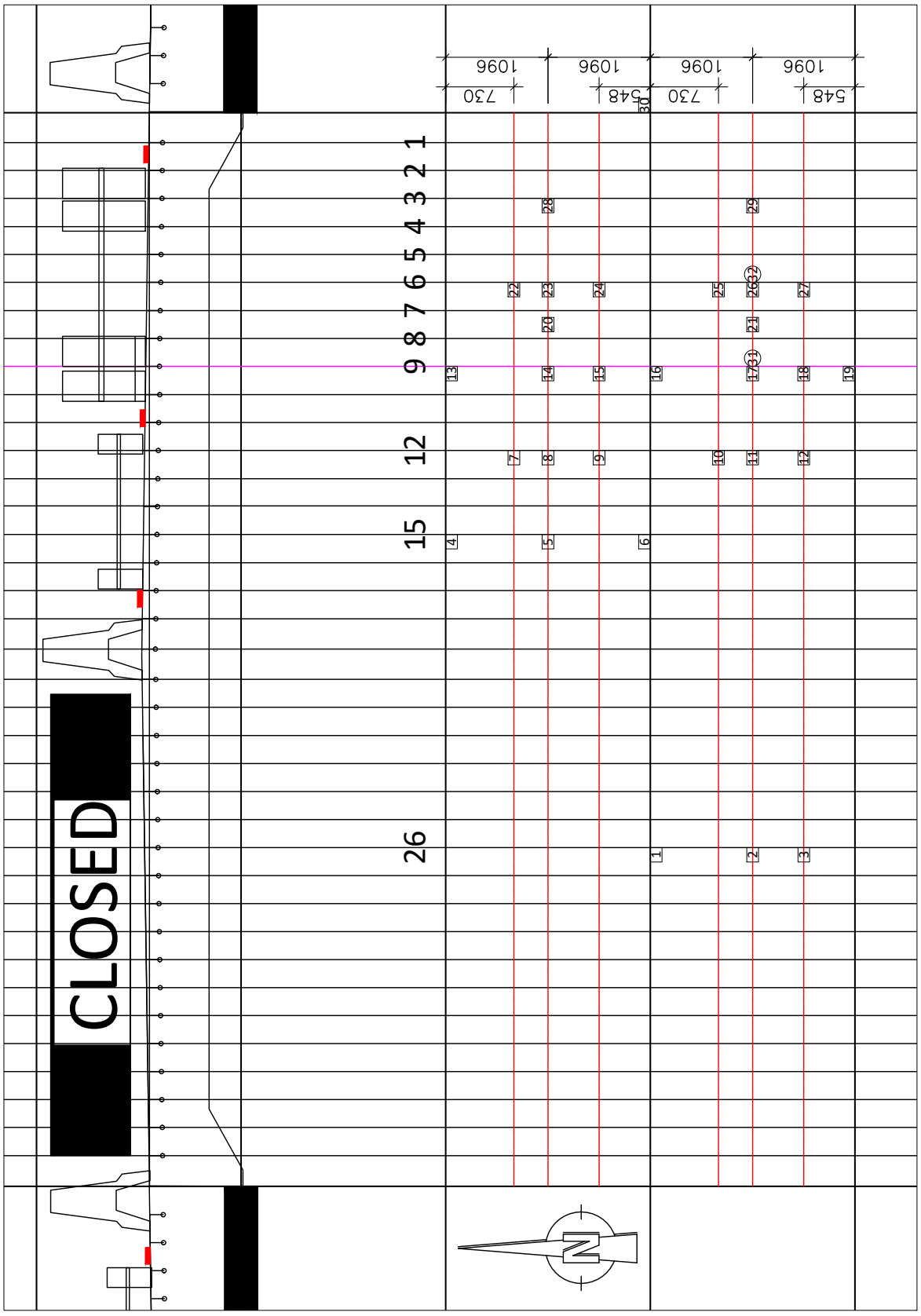

Figure A.1: Top view of the zoomed out accelerometer layout. All squared numbers are sensors in the z-direction and the circular numbers in the y-direction. The vertical lines and the other numbers are the bulbs, the horizontal black lines are the transverse beams and the red lines are guide lines. The pink line is the alignment of the left wheels of heavy trucks.

A.2. Data Analysis

A.2.1. Raw Acceleration Data

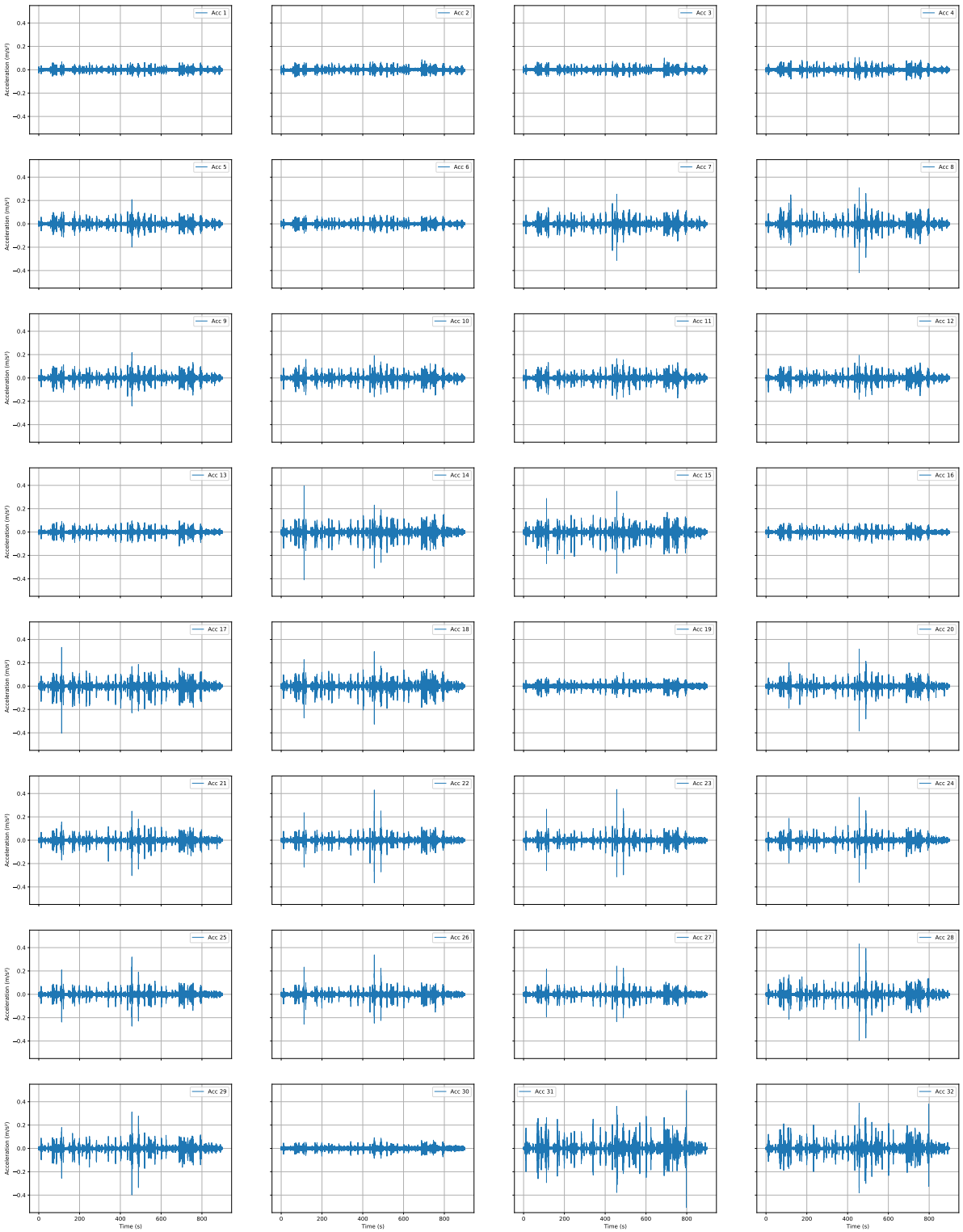

Figure A.2: Raw acceleration data of all sensors recorded on the 11th of October 5:14 AM.

A.2.2. Frequency Spectrum

Figure A.3: Fourier transform of all sensors recorded on the 11th of October 5:14 AM with a high-pass filter of 20 Hz.

A.3. Analytical Model With One Resonator

Before the model with two local resonators was made (Chapter 7), a model consisting of one resonator was set up to perform an eigenfrequency analysis. Figure A.4 shows a drawing of this model. The model consists of two Euler-Bernoulli beams separated by the local resonator. Below the figure, the derivation and results of the eigenfrequency analysis are presented.

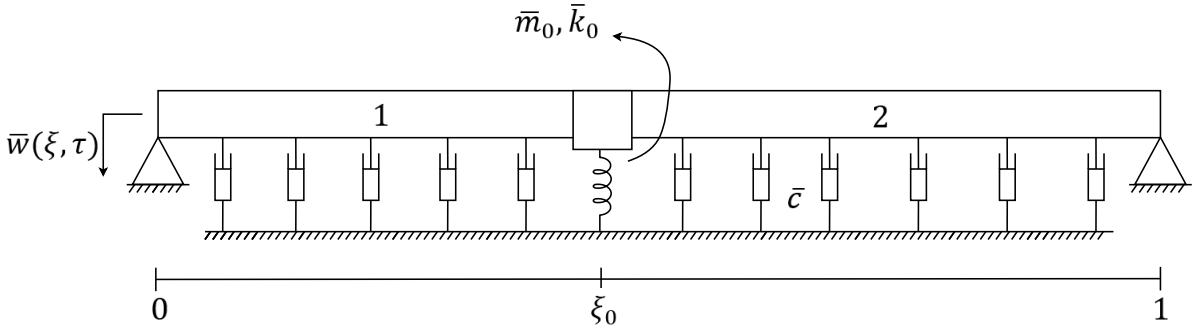

Figure A.4: A drawing of the analytical model with one resonator intended for the eigenfrequency analysis of the beam.

A.3.1. Derivation

The dimensionless equation of motion of a Euler-Bernoulli beam on a viscose foundation is

$$\frac{\partial^4 \bar{w}_i}{\partial \xi^4} + \frac{\partial^2 \bar{w}_i}{\partial \tau^2} + \bar{c}\frac{\partial \bar{w}_i}{\partial \tau} = 0 \tag{A.1}$$

A description of all parameters can be found in Table 7.2. For the sake of clarity, the spatial derivative is denoted with an accent in the remaining of this section, so $dW/d\xi = W'$. Substituting $\bar{w}_i(\xi,\tau) = W_i(\xi)e^{i\phi\tau}$ into Equation A.1 gives:

$$W_i'''' - \beta^4 W_i = 0 \tag{A.2}$$

Where:

$$\beta^4 = \phi^2 - i\phi\bar{c} \tag{A.3}$$

The general solution of Equation A.2 is:

$$W_i(\xi) = A_i\cosh(\beta\xi) + B_i\sinh(\beta\xi) + C_i\cos(\beta\xi) + D_i\sin(\beta\xi) \tag{A.4}$$

Since the model consists of two beams, there is a total of eight unknown dynamic amplitudes. This system can be solved with four boundary conditions and four interface conditions. The system has the following boundary and interface conditions:

$$\begin{aligned}
&W_1(0) = 0\\
&W_1''(0) = 0\\
&W_1(\xi_1) = W_2(\xi_1)\\
&W_1'(\xi_1) = W_2'(\xi_1)\\
&W_1''(\xi_1) = W_2''(\xi_1)\\
&W_2'''(\xi_1) - W_1'''(\xi_1) = \left(\varphi^2\bar{m}_0 - \bar{k}_0\right)W_1(\xi_1)\\
&W_2(1) = 0\\
&W_2''(1) = 0
\end{aligned} \tag{A.5}$$

Substitution of Equation 7.22 into the boundary and interface conditions provides a system of 8 equations containing 9 unknowns (the 8 unknown amplitudes of the general solution and the frequency ϕ). Then, a coefficient matrix $\mathbf{M} \in \mathbb{C}^{8\times 8}$ can be composed containing the coefficients of the amplitudes. One obtains the eigenfrequencies of the system by solving the eigenvalue problem of this matrix:

$$\det|\mathbf{M}| = 0 \tag{A.6}$$

Before the frequency equation was solved, the exploding terms were killed. This was done as follows: the hyperbolic functions were rewritten into exponential functions. Then, the positive exponentials ($\exp(\beta)$) were killed by dividing the equation by it. This made the frequency equation computationally less expensive to solve.

After obtaining the complex eigenfrequencies of the system, the mode shapes were plotted. This required the evaluation of the unknown amplitudes of Equation A.4. Again, the general solution was substituted into the boundary and interface conditions of Equation A.5. A coefficient matrix $\mathbf{A} \in \mathbb{C}^{7\times7}$ and vector $\mathbf{b} \in \mathbb{C}^{7\times1}$ were composed from the first seven equations. The amplitudes were obtained by solving the matrix equation to $\mathbf{x}$:

$$\mathbf{Ax} = \mathbf{b} \tag{A.7}$$

where $\mathbf{x} \in \mathbb{C}^{7\times1}$ is a vector containing the first seven unknown amplitudes. The solutions depend on the 8th unknown amplitude $D2$. Substituting the found eigenfrequencies into the amplitudes and dividing the solution by $D2$ provides the relative mode shapes.

A.3.2. Results

The aim of the model was to find the effect of changing parameters on local mode shapes of the beam. The local mode shapes are induced by the local resonator. Table A.1 shows the chosen input parameters. The selection procedure for the values of these parameters was explained in Chapter 7.

Table A.1: The input parameters of the analytical model for obtaining the eigenfrequencies of the beam with one resonator.

Parameters	Value
ξ_0	0.4
$\bar{k}_0$	6.0×10^6
$\bar{m}_0$	7.6×10^{-2}
$\bar{c}$	6.4×10^3

If the local resonator is simplified to a mass-spring system, the eigenfrequency then follows from:

$$\phi_R = \sqrt{\frac{\bar{k}_0}{\bar{m}_0}} = 8.9 \times 10^3 \quad \text{rad} \tag{A.8}$$

It was expected to find the local mode of the beam induced by the resonator at a frequency relatively close to the eigenfrequency of the resonator. The local mode was found by plotting the mode shapes of the found eigenfrequencies. Two examples are shown in Figure A.5. The mode shape of Figure A.5b with an absolute frequency of 8273 rad was identified as the mode shape induced by the local resonator since the amplitude at the resonator is large compared to the amplitude at the rest of the beam.

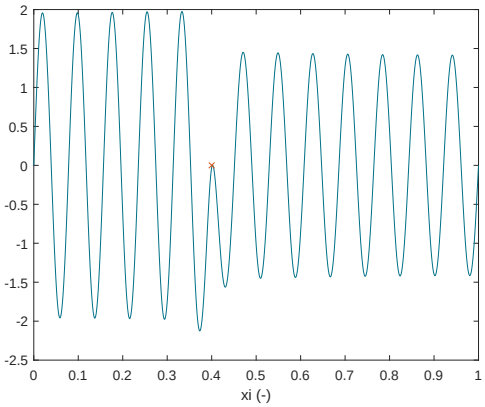

(a) $\phi = 6338$ rad

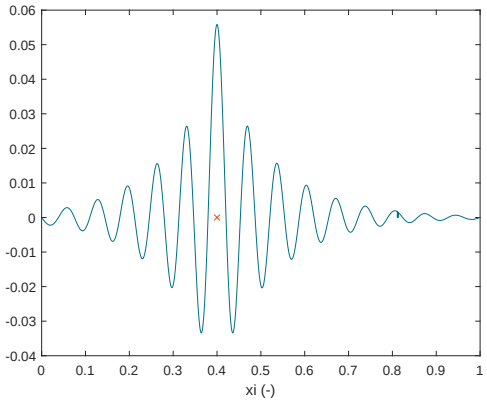

(b) $\phi = 8273$ rad

Figure A.5: Two mode shapes. The mode in b was identified as local mode induced by the resonator.

Despite the fact that it was possible to identify a mode induced by the local resonator, a model with two resonators was proposed. Inducing the local mode shape required an unrealistic amount of damping in the

model with one resonator possibly affecting the reliability and applicability of the results of the time-history analysis. Adding an extra resonator to the model allows the choice of multiple damping coefficients: the part of the beam outside the resonators can still have an unrealistic damping coefficient needed to induce the local mode shape because only the part of the beam in between the resonators has physical meaning. This part can be either undamped or have a realistic damping coefficient.

A relation between the dimensionless damping coefficient $\bar{c}$ and the damping ratio ζ can be obtained by the following steps. First, $\bar{w} = \sin(\pi\xi)q(t)$ is substituted into the equation of motion in Equation A.1 leading to the following equation:

$$\ddot{q} + \bar{c}\dot{q} + \pi^4 q = 0 \tag{A.9}$$

where $\dot{q}$ denotes the first time derivative of $q(t)$, so $\dot{q} = \mathrm{d}q/\mathrm{d}t$. The well known equation of motion of a damped mass-spring system is:

$$\ddot{x} + 2\zeta\omega_n\dot{x} + \omega_n^2 x = 0 \tag{A.10}$$

For the first mode, Equation A.9 can be turned into Equation A.10 by substituting $\omega_n = \pi$, leading to the following relation between ζ and $\bar{c}$:

$$\zeta = \frac{\bar{c}}{2\pi^2} \tag{A.11}$$

A dimensionless damping coefficient $\bar{c}$ of 6.4×10^3 gives a damping ratio ζ of 322 which is an unrealistic value as damping ratios of 1 or higher already indicate that the structure is overdamped. Steel bridges usually have a damping ratio between 0.01 and 0.05.

A.4. Quarter-Vehicle Model

In the semi-analytical model presented in Chapter 7, vehicles were simulated by a single degree-of-freedom (SDOF) mass-spring system. However, another vehicle models were also tried: in case of one moving mass crossing the beam a quarter-vehicle model was introduced. Considering the SDOF vehicle model, the effect of the vehicle characteristics on the dynamic response of the beam was limited: changing the stiffness influenced the amplitude of the Fourier spectrum of the amplitude response significantly but the influence of a changing mass was negligible. The shape of the spectrum did not change (only when increasing the eigenfrequency of the mass-spring system significantly).

A vehicle has more eigenfrequencies than the 1 Hz of the cabin which was modeled. The eigenfrequency of the suspension of a passenger car is about 20 Hz. By introducing a 2DOF mass-spring system (Figure A.6a), it was investigated whether the influence of the vehicle characteristics on the results increased because the second eigenfrequency of the mass-spring system would be closer to the eigenfrequencies of interest of the beam.

The result of the time-history analysis of a beam with default settings but a 2DOF vehicle is shown in Figure A.6b. Two aspects changes compared to the the default model with an SDOF vehicle. Firstly, the amplitude of the response in both the time and frequency domain increased because the spring stiffness of the suspension is much stiffer. Secondly, a peak at the second eigenfrequency of the vehicle is now visible in the frequency domain of the acceleration response of the beam (at about 1400 rad). However, the shape of the higher-frequency components of the spectrum has not changed while the adding an extra degree of freedom to the vehicle approximately doubles the computational expenses. It was therefore chosen to continue with the SDOF vehicle model.

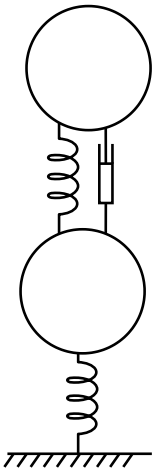

(a) Drawing of the vehicle model

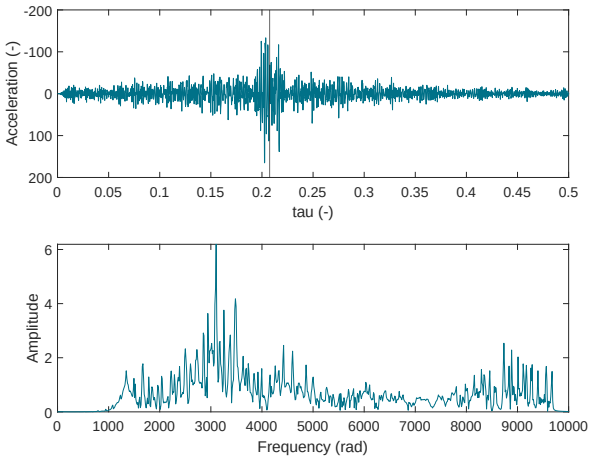

(b) The spectrum of the FT of the acceleration response of the beam at ξ_m

Figure A.6: The response of the beam (b) subjected to a 2DOF vehicle model (a).

A.5. Robustness Analysis

A robustness analysis was performed to investigate whether the sensitivity of the semi-analytical model on the variable parameters was dependent on the fixed parameters. This was done by changing the distance between the local resonators and compare the results with the results of the model with default settings.

First, the effect of the time delay between multiple moving masses with changing fixed parameters was looked into. The results of two different local resonator spacings (Figure A.7) can be compared to the result with default spacing (Figure 7.17b). The following aspects stand out:

- The high-energy frequency bands shifted because the eigenfrequencies of the beam changed.
- The effect of the time delay is exactly the same; the same frequencies are amplified or damped out. This makes sense as the modulation of the signal is only influenced by the axle distance and vehicle velocity.
- In the time domain, the differences between both models are significant. The vibrations induced by the vehicle are longer in duration for the model with large resonator spacing which is caused by the facts that the vehicle is a longer time on the middle beam and that the damping is lower as the middle beam is undamped.

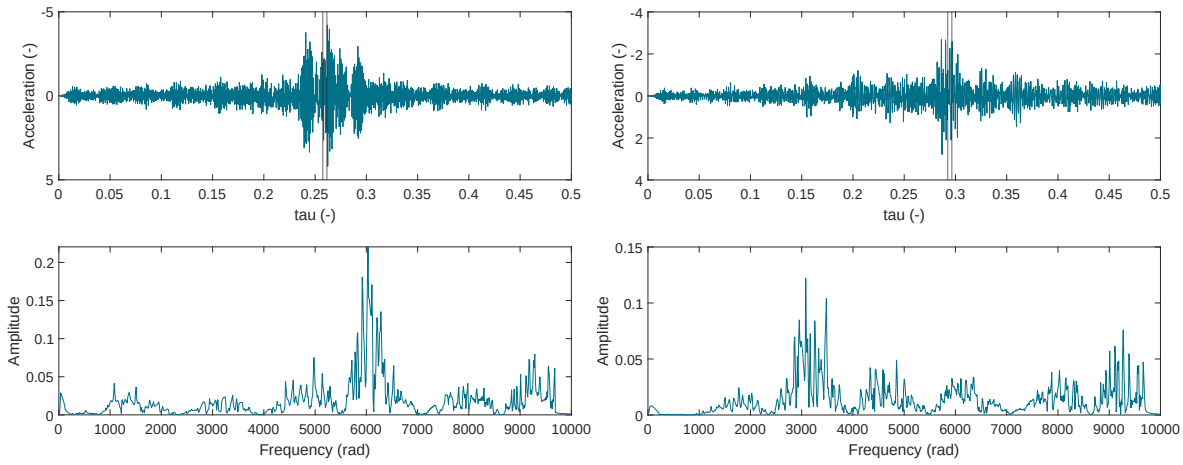

(a) $\xi_1 = 0.35$ and $\xi_2 = 0.48$ (b) $\xi_1 = 0.55$ and $\xi_2 = 0.62$

Figure A.7: The acceleration response of the beam at ξ_m and its Fourier spectrum and the effect of changes in the location of the local resonators on the time delay effect ($\theta_2 = 0.008$). The vertical lines in the time domain are when the moving masses passes ξ_m.

Secondly, the effect of a different resonator spacing on the presence of the dominant unevenness frequency component is shown in Figure A.8. Also the qualitative extent of the influence of this parameters was not changed by choosing a different resonator spacing. The response of the beam did change but this was caused by the changing dynamic properties of the beam.

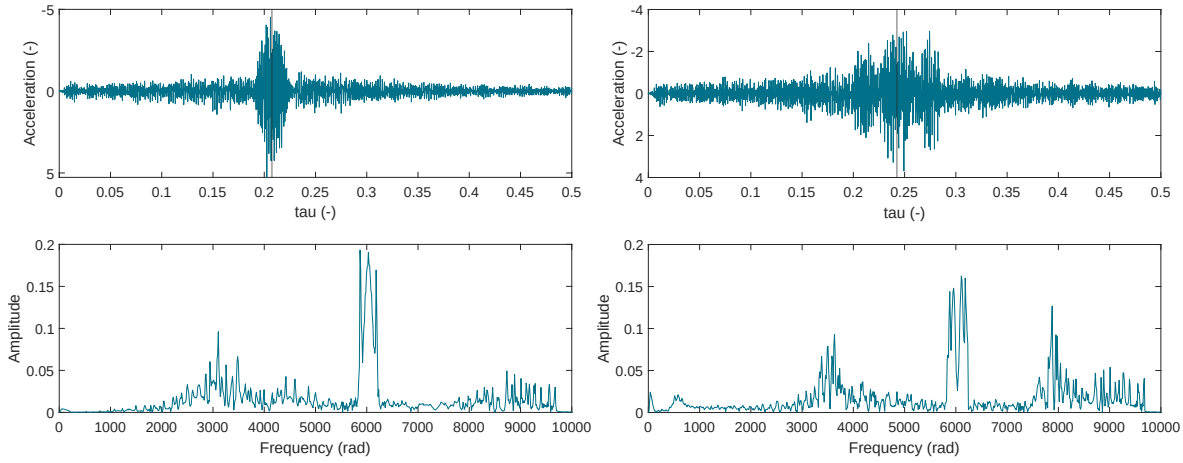

(a) Default settings

(b) $\xi_1 = 0.35$ and $\xi_2 = 0.52$

Figure A.8: The acceleration response of the beam at ξ_m and its Fourier spectrum and the effect of changes in the location of the local resonators on the effect of a dominant unevenness frequency component. The vertical line in the time domain is when the moving mass passes ξ_m.